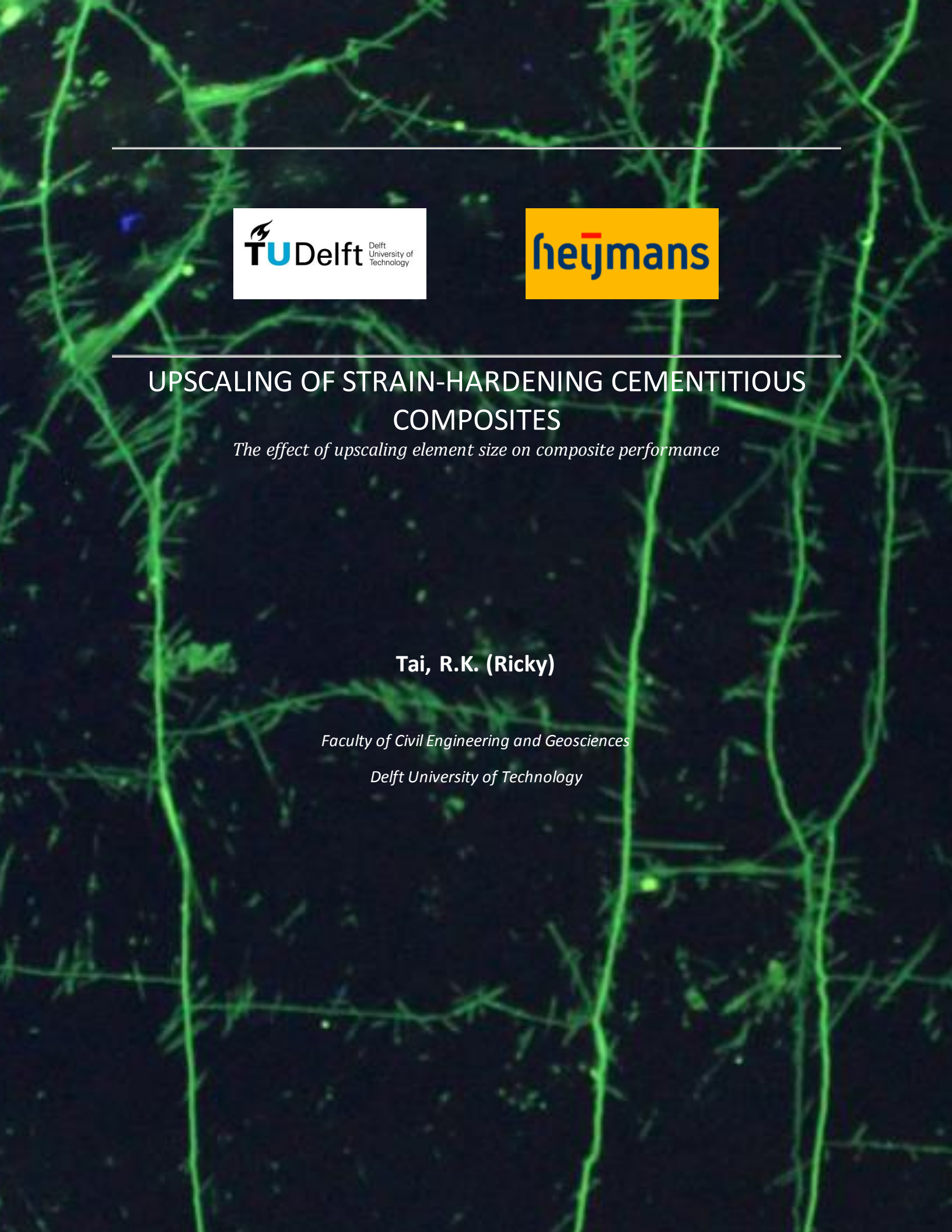

UPSCALING OF STRAIN-HARDENING CEMENTITIOUS COMPOSITES

The effect of upscaling element size on composite performance

Tai, R.K. (Ricky)

Faculty of Civil Engineering and Geosciences

Delft University of Technology

UPSCALING OF STRAIN-HARDENING CEMENTITIOUS COMPOSITES

The effect of upscaling element size on the composite performance

by

Tai, R.K. (Ricky)

In partial fulfillment of the requirements for the degree of
Master of Science
In Civil Engineering

Faculty of Civil Engineering and Geoscience
Delft University of Technology
the Netherlands
July, the 9th 2015

Thesis Committee

Prof.dr.ir. E. Schlangen (Chair)	Delft University of Technology
Prof.dr.ir d. Hordijk	Delft University of Technology
Dr.ir. O. Çopuroğlu	Delft University of Technology
Dr.ir. M. Ottelé	Delft University of Technology / Heijmans
Ir. R. Pepers	Heijmans

TU Delft Delft University of Technology

heijmans

ACKNOWLEDGEMENTS

This thesis is the result of the collaboration of the Microlab and Concrete structures group at the faculty of Civil Engineering and Geoscience of Delft University of Technology, and Heijmans NV.
I would like to express my sincere gratitude to the people I had the opportunity to work with. First I would like to thank the chair of my thesis Prof.dr.ir. E. Schlangen for giving me an opportunity to work on this thesis. I learned a lot from his guidance during the thesis and will cherish the discussions we had. Furthermore I am very thankful for his flexibility, where it seemed that help was always ready when I needed it. I am also very grateful to the other members of my committee. Prof.dr.ir. D. Hordijk for his always keen perspective on my work and the successful arrangement of my experiments in the Stevin 2 lab, which seemed impossible to arrange at the time. Dr.ir. O. Çopuroğlu for his expertise and patient guidance on image analysis, which was a new area of expertise for me. Dr.ir. M. Ottelé and Ir. R. Pepers for their guidance at the start of my thesis, which contributed to a solid basis for my thesis and played a huge role on directing it to the final product. Furthermore I would like to thank them for allowing me to do my thesis in collaboration with their company Heijmans NV.
Aside from my committee I would like to thank the staff at the Microlab and Stevin 2 for their input, cooperation and knowledge during the conduction and preparation of the experiments. Gerrit Nagtegaal who, aside of helping me conduct the experiments, always participated actively in designing the test setup and interpreting the test results. His flexible way of working and outstanding arrangement of the experiment was also much appreciated. Maiko van Leeuwen for his help during the physical labor of mixing and placing SHCC, as well as for his expertise on batching. Albert Bosman and Richard Quist for their guidance and expertise in the experiments in the Stevin 2 lab, which had many new complexities introduced due to the scale of the experiments. Last but not least, the help of other PHD candidates, post-doctoral researchers and fellow graduates which have helped, inspired and motivated me a lot.
I would also like to thank my parents for their unconditional love and support, and forming me to the person that I am today. For instilling their hard working mentality by leading by example. My family and friends for their support and motivation.

SUMMARY

> *"[Strain-hardening cementitious composites (SHCC)] are a new class of [fiber reinforced cementitious] composites characterized by a strain-hardening behavior in tension after first cracking accompanied by multiple cracking up to relatively high strain levels."* [1]

In order to contribute to the transition of relatively thin SHCC elements, used in most lab experiments, into applications of large SHCC elements in practice, knowledge and understanding of the mechanical performance of upscaling the element size is needed. For ordinary concrete a decrease in the nominal strength of a material may be observed when the element size is upscaled. This phenomena is called the size-effect. Many sources of size-effect in concrete have been identified and investigated. These include the Wall effect, diffusion processes, hydration heat, statistical inhomogeneities, linear elastic fracture mechanics, and fractal nature of the crack surface. Even though SHCC shares many similarities with ordinary concrete it also has key differences which could lead to other behavior during upscaling of the element size. Examples of these are the exclusion of coarse aggregates, strong dependency on fiber properties, dispersion and orientation, and a ductile nature of failure.

In this thesis it was first investigated whether there is a general size-effect for SHCC. The adjective 'general' is used because it included multiple sources of size-effect. Aside of size-effect the strain capacity was also considered, since this is one of the main advantages of using SHCC. Two specimen sizes of 120*30*10 mm^3 and 360*90*30 mm^3 were compared in a 4-point bending test (4-PBT). The nominal strength and fictitious strain capacity dropped from respectively 13.3±1.5 MPa to 8.4±0.4 MPa and 8.9±1.6 ‰, to 4.9±2.1 ‰ due to the upscaling. The fictitious strain is a strain calculated based on the deflection of the specimen and linear elasticity.
There are many sources of size-effect and it has been decided to investigate the effect of fiber effectivity and fracture mechanics based size-effect. Since fibers play an important role of the behavior of SHCC and fracture based size-effect is a main contributor of size-effect in ordinary concrete.
Aside from the findings above, there are strong suggestions that increase of the loading (displacement) rate will decrease the nominal strength and strain capacity significantly. Furthermore a protocol has been developed to characterize the crack width distribution of the cracked SHCC specimen for future research.

Two parameters, concerning the fiber dispersion and orientation, were used to quantify the fiber effectivity. It is suspected that the relatively thin SHCC elements, commonly used in lab experiments, might alter the fiber orientation favorably, and overestimates the nominal strength and strain capacity compared to thicker elements. To investigate this a SHCC cube of 150*150*150 mm^3 was produced, where after three differently orientated specimens of 120*30*10 mm^3 were sawn out. The nominal strength and strain capacity of these specimens were obtained with a 4-PBT and compared to the values of thin casted specimens of 120*30*10 mm^3. To verify whether the specimens from the cube had significant alteration of the fiber effectivity and to investigate the effect of fiber effectivity, specially prepared sections with a thickness of approximately 40 microns were analyzed under an optical microscope with a XPL filter. It has been verified that fiber orientation has been altered for the specimens sawn from the cube, and the decrease of the nominal strength and strain capacity of the

[1] Naaman, A. E. (2007). High performance fiber reinforced cement composites: classification and applications. In CBM-CI international workshop, Karachi, Pakistan (pp. 389-401).

specimens could be explained by lower limit of the fiber effectivity parameters. The lower this limit is, the bigger the decrease in the nominal strength and strain capacity was found.
Within the three differently orientated specimens, one type showed quasi-brittle failure instead of strain-hardening. This type of specimen was vertically orientated in the cube and had surprisingly comparable fiber orientation and dispersion compared with the other specimens. The quasi-brittle failure might be introduced by the placement method of the SHCC in the cube, which led to interfaces with weak cement properties in combination with reduced amount of effective fibers. Due to the specimen orientation, this interface covers at least the whole cross section of the vertical orientated specimen.
It is recommended to use steel bars as primarily reinforcement for safety and the fibers for the multiple fine cracks, and to develop a placement method that reduces the margin of error of the fiber effectivity parameters.

Fracture mechanics based size-effect is explained by the science of fracture mechanics. For quasi-brittle materials like concrete, increasing the specimen size will shift the material in the linear elastic fracture mechanics zone in the generalized size-effect law. In this zone the nominal strength drops significantly. One study revealed that there is no size-effect in SHCC if there is adequate strain-hardening. This is pleasant, but size-effect concerns only the nominal strength and in SHCC the strain capacity is an more important parameter. Therefor in this experimental series also the effect of upscaling of the element size on strain capacity was investigated along with the size-effect. This was done by investigating differently sized specimens with fixed thickness and a fixed specimen height and span ratio. Specimens with spans of 175, 350, 700, and 2100 mm were investigated.
It has been found that only the specimens with a span of 2100 mm had a significant drop in nominal strength. This could be explained by an inadequate strain-hardening ability of the used mix design. Furthermore the strain capacity did gradually decrease for each size. This raises major concern since strain capacity is a main advantage of SHCC. A theoretical model has been developed to explain these findings. This model is based on the strength of the material along the crack. Where the strength in the crack tip decreases when it approaches the crack opening where the strain is higher. It was assumed that the crack width increases with element size. With digital image correlation (DIC) technique the crack width has been determined along the height of the localized macro cracks for one specimen per span length. The results were corresponding to the assumption with the exception of the specimen with span 700 mm. This might be due to the acquisition of the data, where only one cracked surface was investigated by the digital image correlation technique. There is indication that at this specimen of 700 mm a relatively stronger variance in the distribution of the crack width along the specimen thickness was present.
Finally three methods to compute a strain were compared: the fictitious strain based on deflection of the specimen and linear elasticity, the engineering strain calculated from the elongation measured with a LVDT, and the DIC strain obtained by the DIC technique. The fictitious strain is not reflecting the material behavior. The engineering strain is the most commonly used method to acquire strain, but measures with a eccentricity and is not practical to measure the strain over a bigger area. The DIC strain measures directly without eccentricity, covers a big area relatively easy, and can easily identify separate cracks. Based on the DIC strains found in the experiments the measured strain at values close to zero is illogical and absolute values presumably incorrect. However this might be corrected with proper calibration of measuring technique.

CONTENTS

LIST OF SYMBOLS

Roman lower case letters

a	Distance between the outer support in 4-PBT	[mm]
b	Initial specimen width	[mm]
$d1$	Major axis of spread in mini slump test	[mm]
$d2$	Axis orthogonal to $d1$	[mm]
d_f	Fiber diameter	[mm]
f_c'	Cylinder compressive strength	[MPa]
f_{ctm}	Mean axial tensile strength	[MPa]
$f_{ctm,fl}$	Mean flexural tensile strength	[MPa]
g	Snubbing factor, coefficient to raise the bridging stress of fibers which are inclined to the matrix crack plane	[-]
h	Initial specimen height	[mm]
l	Span	[mm]
l_{ch}	Characteristic length	[mm]
l_e	Original embedding length of the fiber in the fiber pullout test	[mm]
l_{p0}	Pullout segment of the fiber in the fiber pullout test	[mm]
n	Number of grids per section	[-]
p	Probability	[-]
q	Uniform distributed load	[N/mm]
s_{3ML}	Initial displacement rate of the 3ML specimen	[mm/s]
s_{3ML}'	Adjusted displacement rate of the 3ML specimen	[mm/s]
t	Time	[s]
t_{LOP}	Time at LOP	[s]
z	Coordinate along the height of the specimen	[mm]

Roman upper case letters

C	Complementary energy	[J/m2]
CV	Coefficient of variation	[-]
D	Characteristic dimension	[mm]
E	Young's modulus	[MPa]
E_m	Young's modulus of matrix	[MPa]
F	Force in piston	[N]
$F_{steel\ block}$	Force from the steel block	[N]
G_d	Chemical bond between fiber and matrix	[J/m2]
G_f	Fracture energy	[J/m2]
J_c	Matrix toughness	[J/m2]
J_{tip}	Crack tip toughness	[J/m2]
K_m	Fracture toughness	[J/m2]
L_f	Fiber length	[mm]
L_o	Initial length	[mm]
P	Applied load of single fiber pullout test	[N]
PSH_{energy}	Energy criteria for strain-hardening	[-]
$PSH_{strength}$	Strength criteria for strain-hardening	[-]
RH	Relative humidity	[%]
V_f^{crit}	Critical fiber volume fraction	[m3]

$X_{average}$	Average number of fibers in one section	[-]
X_i	Average number of fibers per grid in one section	[-]

Greek lower case letters

α_1	Factor describing the lower limit of nominal strength ML specimen	[-]
α_2	Factor describing the lower limit of nominal strength 3ML specimen	[-]
$\alpha_{dispersion}$	Coefficient of dispersion	[-]
α_{fiber}	Fiber distribution coefficient	[-]
β	Slip hardening coefficient	[-]
δ	Average crack opening	[mm]
δ_0	Crack opening corresponding to maximum bridging stress	[mm]
δ_p	Deflection of piston	[mm]
δ_{ss}	Constant crack opening of steady-state cracks	[mm]
ε	Strain	[‰]
$\varepsilon_{c,LOP}$	Compressive strain at MOR	[‰]
$\varepsilon_{t,MOR}$	Tensile strain at MOR with uniaxial tensile test (UTT)	[‰]
$\varepsilon_{t.LOP}$	Tensile strain at LOP with uniaxial tensile test (UTT)	[‰]
ϑ	Angle of the fiber with respect to the loading axis	[°]
σ	Stress	[MPa]
σ_{crack}	Average bridging stress along the crack	[MPa]
$\sigma_{3ML,\ average}$	Average nominal strength of 3ML specimen	[MPa]
$\sigma_{f,MOR}$	Compressive stress at MOR	[MPa]
$\sigma_{ML,\ average}$	Average nominal strength of ML specimen	[MPa]
σ_o	peak stress of the average bridging stress	[MPa]
σ_{ss}	Constant ambient tensile stress	[MPa]
$\sigma_{t,LOP}$	Tensile stress at LOP with uniaxial tensile test (UTT)	[MPa]
$\sigma_{t,MOR}$	Tensile stress at MOR with uniaxial tensile test (UTT)	[MPa]
τ	Frictional bond property	[MPa]

Greek upper case letters

Δl	Elongation	[mm]

LIST OF ABBREVIATIONS

2D	Two dimensional
3D	Three dimensional
3-PBT	3- Point bending test
4-PBT	4-Point bending test
A_{Aa}	Area fraction of constituent A
BFS	Blast furnace slag
CV	Coefficient of variation
DIC	Digital image correlation
ECC	Engineered cementitious composites
FA	Fly ash
FRC	Fiber reinforced concrete
HPFRCC	High performance fiber reinforced cementitious composites
HTPP	High tenacity polypropylene
HTPP-SHCC	Strain-hardening cementitious composites with high tenacity polypropylene fibers
ITZ	Interfacial transition zone
LEFM	Linear elastic fracture mechanics
LOP	Limit of proportionality
LP	Limestone powder
LVDT	Linear variable differential transformer
MOR	Modulus of rupture
OPC	Ordinary Portland cement
PDF	Probability density function
PE	Polyethylene
PL	Parallel placement of material to the longitudinal direction of the beam
PVA	Polyvinyl alcohol
PVA-SHCC	Strain-hardening cementitious composites with polyvinyl alcohol fibers
R/SHCC	Reinforced Strain-hardening cementitious composites
RGB	Red, Green, and Blue
SHCC	Strain-hardening cementitious composites
SP	Superplasticizer
TL	Transversal placement of material to the longitudinal direction of the beam
UTT	Uniaxial tensile test
UV	Ultraviolet
VMA	Viscosity modifying agent
V_{Va}	Volume fraction of constituent A
w/b	Water to binder ratio
w/p	Water to powder ratio
XPL	Cross polarized light

LIST OF FIGURES

LIST OF TABLES

PART I: INTRODUCTION

1 GENERAL INTRODUCTION

1.1 BACKGROUND

Strain-hardening cementitious composites (SHCC) is a relatively new class of fiber reinforced cementitious composite. Different names have been given to this class of material, e.g. High Performance Fiber Reinforced Cement Composites (HPFRCC) and Engineered Cementitious Composites (ECC). However, in this thesis the term SHCC will be adopted, because it contains a description that distinguishes SHCC from other composites. The following definition of SHCC is given by Naaman [1]:

> *"[SHCC] are a new class of [fiber reinforced cementitious] composites characterized by a strain-hardening behavior in tension after first cracking accompanied by multiple cracking up to relatively high strain levels."*

The tensile strain-hardening behavior is depicted in Figure 1.1. Whereas the curves A,B, and C schematically show the typically tensile stress-strain relation of respectively plain concrete mixture, conventional fiber reinforced concrete (FRC), and SHCC. The corresponding failure modes are respectively brittle, quasi-brittle, and strain hardening. This strain hardening behavior under tensile loading is inherent with the formation of multiple fine cracks and can lead to high levels of tensile strain capacity. It is possible to produce SHCC with a tensile strain capacity of several hundred times higher than of plain concrete mixture [2]. In addition, the strain-hardening behavior of SHCC relates to an enhanced modulus of rupture and fracture energy of SHCC compared to plain concrete mixture and FRC [6]. These properties can be exploited favorably when designing civil structures and are summarized in Table 1.1 [3]. For example in [4] a design for SHCC integrated reinforced concrete beams, where the reinforcement is surrounded by SHCC, was researched. With this design crack width could be limited to values unachievable with conventional reinforced concrete, which contributes to enhanced durability of the beam. It should be noted that this table is not exhaustive, as more applications for SHCC are being investigated, see e.g. the Structural design and practical applications of SHCC sessions in the International RILEM Conferences on Strain Hardening Cementitious Composites [5].

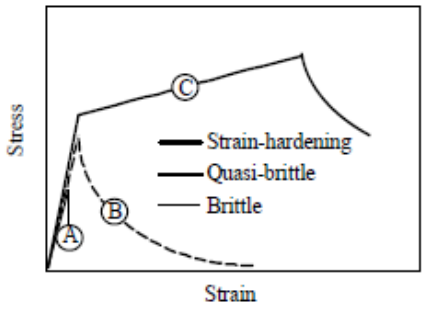

Figure 1.1 Three types of tensile failure mode observed in cementitious materials [6].

Table 1.1 Favorable SHCC behavior and potential applications [3].

Favorable SHCC behavior	Potential applications
Possible reduction or elimination of shear reinforcement	Reinforced SHCC beams, hinges of beam column connection
Sustaining large imposed deformation without damaged localization	Possible to replace conventional joints at bridge deck, seismic retrofitting
Compatible deformation between SHCC and reinforcement	Can avoid spalling, bond splitting and other common failure modes due to incompatible deformation and high shear lag
High damage resistance and reduction	Structure insensitive to notches, dents etc. Application at places with high stress concentration factor
Tight crack control width	Enhance durability of structure and liquid tightness

1.2 RESEARCH JUSTIFICATION

1.2.1 RESEARCH SIGNIFICANCE

Despite the favorable material properties of SHCC compared to conventional concrete and other FRC, use of SHCC in the Netherlands has been scarce. This could be due to many reasons, such as high costs, the absence of designing guidelines or codes, lack of application areas etc. Furthermore, there might be a scaling problem between elements tested in the lab and applications of SHCC in the practice. Where in the lab SHCC was mostly produced in small quantities and tested as relatively small elements where the element thickness was close to fiber length. While in practice larger quantities of SHCC and relatively thicker elements, with higher element thickness to fiber length ratio, are needed in many cases. Additionally, upscaling of the production quantities and the size of elements may lead to respectively reduced material properties and scaling problems in terms of nominal strength. For the latter it is known that ordinary concrete has reduced nominal strength when the element size is increased up to certain dimensions. This is described by the size-effect law for concrete and other quasi-brittle material [7]. However relatively little is known about the size-effect in SHCC, which unlike concrete is not a quasi-brittle material.

1.2.2 AREA OF RESEARCH INTEREST

The area of interest is the reduced composite performance of SHCC when element geometry is upscaled with respect to the common lab-tested elements. In this thesis the composite performance will be evaluated by the nominal strength and the strain capacity.

The focus lies on two possible sources for reduced composite performance. These are the fiber effectivity and fracture mechanics based size-effect. The fiber effectivity is a based on the fiber arrangement. Most SHCC elements tested in the lab are generally of small thickness [e.g. 2, 8]. Where it could be argued that fiber arrangement is mostly two-dimensional, while applications in practice may lead to a three-dimensional fiber arrangement (Figure 1.2 [9]). While the fracture mechanics size-effect is an extensively investigated size-effect in concrete and can be explained by fracture mechanics.

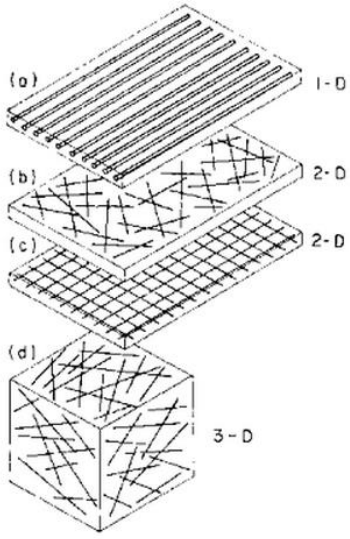

Figure 1.2 Classification of fiber arrangements in one (a), two (b and c) or three (d) dimensions [9].

1.2.3 RESEARCH AIM, OBJECTIVE, AND SUB-QUESTIONS

The overall aim of this thesis is to contribute to the transition of common lab-tested SHCC elements into applications of large SHCC elements. This can be achieved through the following objective:

> *The objective of this thesis is to identify and evaluate sources which are accountable for reduced performance of SHCC when the element size is upscaled, and provide critical factors to parties, e.g. concrete plants and contractors, who produce large SHCC structures.*

The objective is subdivided into the following sub-questions:

1. What is the effect of increasing the element size of typical lab-sized elements on the nominal strength and strain capacity?
2. How does fiber effectivity alter due to upscaling of the SHCC element size, and what effect has it on the nominal strength and strain capacity?
3. What is the contribution of fracture mechanics based size-effect to the size-effect of SHCC?

1.3 RESEARCH STRATEGY

SHCC is a delicate material and sensitive to many factors which can influence the successful performance of the composite. Therefor a literature survey is first performed in order to gain insight on subjects such as the mechanical behavior and the mechanism responsible for its strain-hardening characteristics. Then the mix design of cement-based materials will be investigated, because the performance for a particular SHCC depends heavily on the mix design. Later on other relevant subjects such as the specimen preparation and size-effect in concrete will be investigated.
Since not much is known about the effects of upscaling the element size of a SHCC specimen, a typical lab-sized element will be compared to an element which is enlarged in three dimensions. In case of significant size-effect two possible sources of size-effect will be researched. These are the effectivity of the fibers and the fracture mechanics based size-effect. Since fibers are a significant constituent of SHCC and plays an important role in the composite performance. Fiber effectivity will be evaluated by two

parameters: fiber dispersion and fiber orientation. These can be significantly altered when the geometry is upscaled. While the fracture mechanics based size-effect is a main contributor in the size-effect of conventional concrete. Therefor understanding of these two sources might be crucial when upscaling the element size.
Finally a summary of the conclusions and recommendations will be presented at the end of this thesis. Figure 1.3 depicts the flow chart of this thesis.

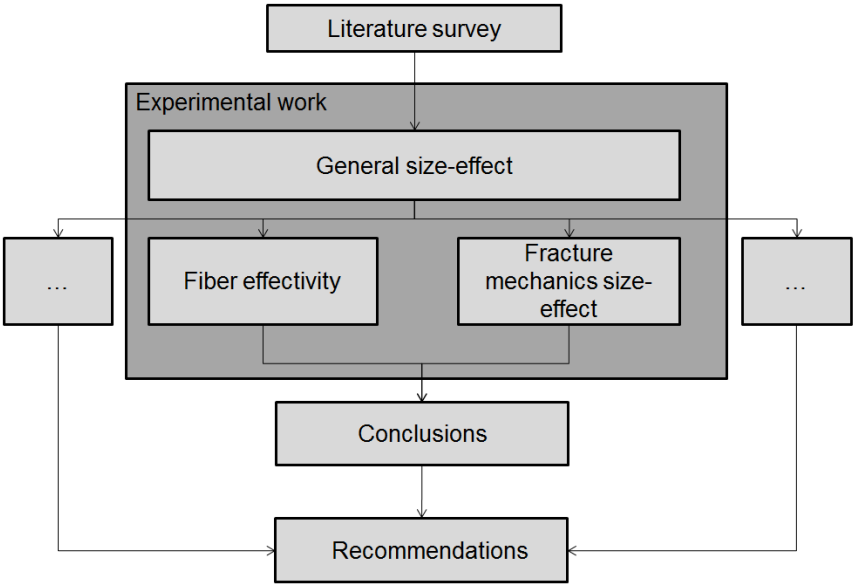

Figure 1.3 Flowchart of the thesis.

REFERENCE LIST PART I

[1] Naaman, A. E. (2007). High performance fiber reinforced cement composites: classification and applications. In CBM-CI international workshop, Karachi, Pakistan (pp. 389-401).
[2] Li, V. C., Wu, C., Wang, S., Ogawa, A., & Saito, T. (2002). Interface tailoring for strain-hardening polyvinyl alcohol-engineered cementitious composite (PVA-ECC). ACI Materials Journal, 99(5).
[3] Li, V. C. (2003). On engineered cementitious composites (ECC). Journal of advanced concrete technology, 1(3), 215-230.
[4] Maalej, M., & Li, V. C. (1995). Introduction of strain-hardening engineered cementitious composites in design of reinforced concrete flexural members for improved durability. ACI Structural Journal, 92(2).
[5] Toledo Filho, R.D. & Silva, F.A. & Koenders, E.A.B. & Fairbairn, E.M.R. (2011) 2nd International RILEM Conference on Strain Hardening Cementitious Composites (SHCC2-Rio). RILEM Publications SARL
[6] Li, V. C. (1998). Engineered Cementitious Composites-Tailored Composites Through Micromechanical Modeling.
[7] BazÏant, Z. P.; Planas, J.: Fracture and Size-effect in Concrete and Other Quasibrittle Materials. Boca Raton: CRC Press 1998
[8] Sahmaran, M., Lachemi, M., Hossain, K. M., Ranade, R., & Li, V. C. (2009). Influence of aggregate type and size on ductility and mechanical properties of engineered cementitious composites. ACI Materials Journal, 106(3).
[9] Arnon, B., & Sidey, M. (2007). Fiber reinforced cementitious composites. I)(second edition). London: Taylor & Francis Group.

PART II: LITERATURE SURVEY

2 LITERATURE SURVEY

2.1 MATERIAL CHARACTERISTICS

SHCC is a relatively new class of fiber reinforced cementitious composite. A definition is given in chapter 1.1. The strain-hardening behavior under tensile stress, also known as tensile strain-hardening behavior, is depicted in Figure 2.1. Whereas the curves A, B and C show the schematized tensile stress-strain relation of respectively plain concrete mixture, conventional FRC, and SHCC. The corresponding failure modes are respectively brittle, quasi-brittle and strain-hardening. The tail softening of FRC and strain-hardening of SHCC can be attributed to the bridging action of the aggregates, cement ligaments, and/or fibers. What distinguishes SHCC from other FRC or cementitious composites is strain-hardening under tension along with the forming of multiple fine cracks. The mechanism behind this characteristic behavior will be explained in more in detail in chapter 2.2.

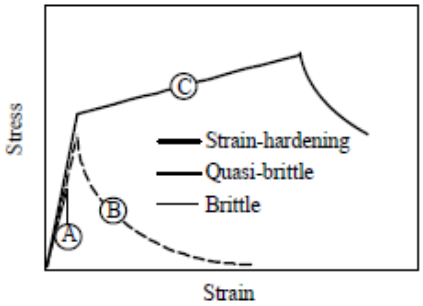

Figure 2.1 Three types of tensile failure mode observed in cementitious materials [1].

As of present many mix proportions of SHCC have been developed, e.g. self-consolidating, high early strength, lightweight and green SHCC. Designs with local materials (Japan, Europe, South Africa and USA) have also been successful. The strain capacity for common SHCC ranges from 1 to 8 percent. [2].

Early SHCC mix designs typically contain a binder (e.g. cement and fly ash (FA)), sand (Microsilica sand average and maximum grain size of respectively 110 and 200 µm), superplasticizer (SP) and fibers (e.g. polyvinyl alcohol (PVA) and polyethylene fibers (PE), <2% fiber volume fraction) [2, 3]. Table 2.1 shows the mix design proportions by weight for ECC-M45, a self-compacting SHCC developed in the USA [2].

Table 2.1 Mix design proportions by weight of ECC-M45 [2].

Cement	Fly Ash	Sand	Water	SP	Fiber (Vol%)
1.0	1.2	0.8	0.56	0.012	0.02

2.1.1 MECHANICAL BEHAVIOR: SHCC VS FRC WITH STEEL FIBERS

Below a review of mechanical properties of SHCC in comparison with FRC with 1% volume fraction of steel fibers is given. Both types of materials are tested under the same conditions. Results of this

comparison are summarized in Table 2.2 [1]. Where the moment of first crack and peak stress in the stress-strain diagram is called respectively the limit of proportion (LOP) and modulus of rupture (MOR).

The tensile behavior between SHCC and FRC with steel fibers (1%) were compared with the uniaxial tensile test (UTT). In SHCC multiple crack development with many sub-parallel cracks during the strain-hardening phase were observed. After reaching the MOR in the stress-strain diagram, crack extension accompanied by fiber bridging was observed. With the FRC a quasi-brittle behavior was observed. Where the softening tail is the result of the opening of one localized macro crack.
The compressive strength measured with the cylindrical compression test showed slightly better performance for SHCC compared to FRC. An increase of 50-100% compared to conventional concrete was observed.
The flexural strength of SHCC and FRC was compared with a 4-point bending test (4-PBT). SHCC showed a slightly higher flexural strength and reached the peak flexural stress slower than FRC. During the increase of flexural stresses, development of multiple fine cracks were observed in the SHCC specimens. To determine the fracture energy a fracture test similar to ASTM E399-78 was performed. Significant higher fracture energy was measured in SHCC specimens than in FRC with steel fibers (1%) specimens.

Table 2.2 Mechanical properties of SHCC and FRC with 1% volume fraction steel fibers tested under the same conditions [1].

	Tensile				**Compressive**		**Stiffness**	**Flexural**	**Fracture**
	$\sigma_{t,LOP}$ [MPa]	**$\varepsilon_{t,LOP}$ [‰]**	**$\sigma_{t,MOR}$ [MPa]**	**$\varepsilon_{t,MOR}$ [‰]**	**f_c' [MPa]**	**ε_{cu} [‰]**	**E [MPa]**	**$\sigma_{f,MOR}$ [MPa]**	**G_f [J/m^2]**
SHCC	2.5	0.21	4.6	56	68.5	6.7	22000	25	27000
FRC	4.3	0.35	4.3	0.35	55	14.8	32500	10.9	4900

Where:

- $\sigma_{t,LOP}$ *Tensile stress at LOP with uniaxial tensile test (UTT)*
- $\varepsilon_{t,LOP}$ *Tensile strain at LOP with UTT*
- $\sigma_{t,MOR}$ *Tensile stress at MOR with UTT*
- $\varepsilon_{t,MOR}$ *Tensile strain at MOR with UTT*
- f_c' *Cylinder compressive strength*
- $\varepsilon_{c,LOP}$ *Compressive strain at MOR*
- E *Young's modulus*
- $\sigma_{f,MOR}$ *Tensile stress at MOR with a flexural test*
- G_f *Fracture energy*

2.2 MECHANISM AND CRITERIA

2.2.1 MECHANISM

The tensile stress-strain diagram is depicted in Figure 2.2. This behavior is the result of the development of multiple fine cracks accompanied by multiple small drops of stress in the diagram, and therefor sometimes termed pseudo strain-hardening. Increased loading of the specimen leads to the growth of the first micro crack, corresponding to the first drop in the stress-strain diagram. Shortly after a drop of the stress in the diagram the fibers are bridging the crack, slip-hardens, and transferring the load through the crack. The process of slip-hardening will be discussed later in chapter 2.2.4.3. The crack bridged by the slip-hardened fibers is now strengthened and can carry the stress through the crack. An increase of the load level will lead to the formation of the next micro-crack. This crack will grow in the matrix with the biggest flaw size. Subsequently a small drop in the stress will occur. The fibers will bridge this new crack, slip-harden and transfer the stress through the crack. The repeated development of multiple fine cracks will continue until the specimen is saturated with multiple fine cracks. Increasing the load even more will lead to a short fiber pull-out phase where all cracks will widen. This leads to a

decrease of the fiber bridging strength. Which leads to the localization of a single macro-crack, depicted as the thickest dark stripe in the most right-hand sided specimen in Figure 2.2. At this point fibers are either completely pulled out or broken. As one can see, it is the ability to develop multiple fine cracks that leads to the enhanced strain capacity of SHCC [2, 4].

2.2.2 STRENGTH AND ENERGY CRITERIA FOR STRAIN-HARDENING

For strain-hardening to occur there are two criteria, often named the strength and energy criteria. A summary of [5,6,7] describing these criteria is given below.

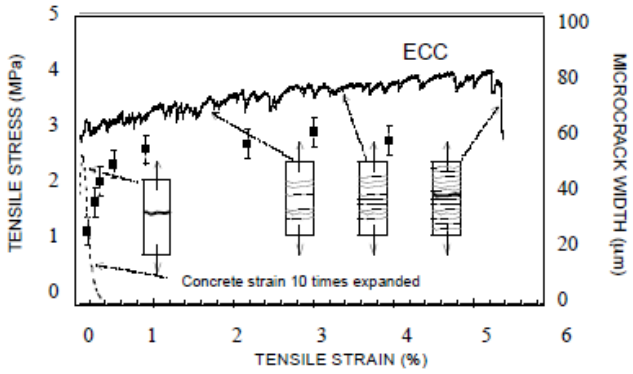

Figure 2.2 Tensile stress-strain curve of SHCC and the crack width development as a function of the imposed strain. [2].

The strength criteria is relatively easy to understand. In order to achieve the strain-hardening behavior of SHCC multiple fine cracks must be given the opportunity to develop. This means that the fiber may not rupture at the cracking strength of the matrix as this will lead to a immediately failure of the bridging fibers. This will prevent the development of fine cracks and hence the strain-hardening behavior. Therefor the strength criterion is that the fiber maximum bridging stress is bigger than the matrix cracking stress.

As explained before, the strain-hardening behavior of SHCC is the result of the formation of multiple fine cracks under tension. Multiple fine cracks can only develop when the cracks in the SHCC matrix are the steady-state type of cracks.
Figure 2.3 schematically shows a Griffith type and steady-state flat crack [5]. The Griffith type of crack is characterized by the Griffith residual strength concept, which relates a decreasing tensile stress to an increasing crack opening. This decrease of tensile stress can be related to the middle fibers of the crack, which are depicted as broken or less stiff springs in the figure. For the steady state crack this is not the case. Steady-state cracks are flat shaped cracks where the crack opening is smaller than a critical crack opening. These cracks are characterized by the constant crack opening δ_{ss} under a constant ambient tensile stress σ_{ss}. Resulting into a flat shaped crack.

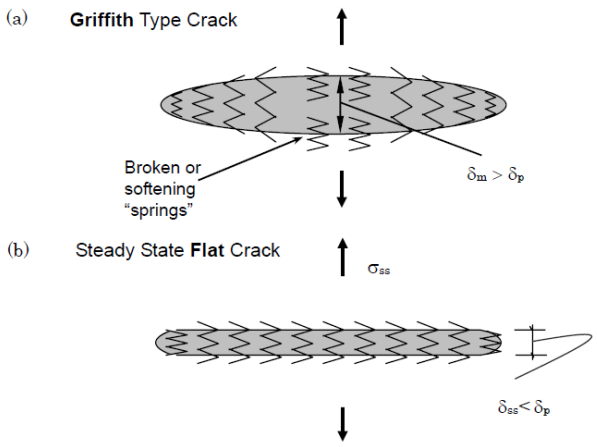

Figure 2.3 Schematized view of the Griffith type crack (a) and the steady state flat crack (b) [5].

In turn the steady-state cracks only develop under a certain condition, formulated by Marshall and Cox [8]. They have shown that steady state crack propagation prevails when [9]:

$$J_{tip} \leq \sigma_{ss}\delta_{ss} - \int_0^{\delta_{ss}} \sigma(\delta)d\delta = C \qquad \textit{(eq. 2.1)}$$

Where J_{tip} is the crack tip toughness and C the complementary energy. Figure 2.4 describes the relation between the average bridging stress transferred across a crack and the opening of this crack.

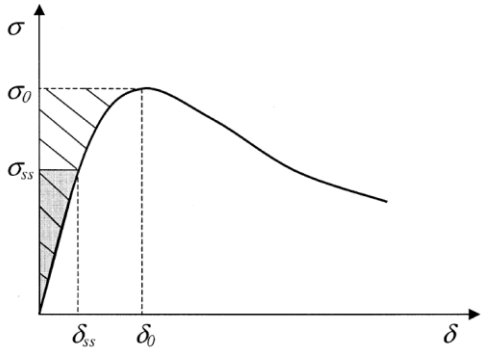

Figure 2.4 The average bridging stress across the crack versus the opening of the crack. Where the shaded area is the complementary energy [7].

The parameters in the middle part are depicted in Figure 2.4. At low fiber contents, which is the case for most SHCC mix proportions, the J_{tip} the matrix toughness J_c. The J_c is calculated as K_m^2/E_m, with K_m and E_m respectively the fracture toughness and Young's modulus of the matrix. It can be seen that the condition in (eq. 2.1) can be influenced by factors such as the water content in the mix proportion, and aggregate size and content.
Figure 2.4 and (eq. 2.1) can be interpreted as follows. The middle part of (eq. 2.1) is equal to the external applied energy minus the energy that dissipated by the deformation of the inelastic springs. It is in fact a potential energy that is stored at the crack tip. The energy criterion is that the complementary

energy, the stored energy, must be bigger than the crack tip toughness, energy needed to propagate the crack. This makes it possible for the crack to grow in length instead of width.

2.2.3 TAILORING SHCC BY MICROMECHANICS

High ductility of SHCC is achieved by maximizing the C. As can be seen in Figure 2.4, the C is the arced area and is limited by the peak stress in the $\sigma(\delta)$ diagram, σ_0. The amount of complimentary energy can be influenced through numerous matrix-fiber mechanism and is summarized in Table 2.3.

Table 2.3 Relation of σ(δ) curve and fiber-matrix interaction mechanism.

Part of $\sigma(\delta)$ curve	**Influenced by**
Slope of rising branch	Fiber volume, length and diameter and Young's modulus
Origin of rising branch	Presence of chemical bond shifts the origin upwards
Peak value of $\sigma(\delta)$ curve	Volume, length and diameter of the fiber, and fiber-matrix frictional bond stress

In [10] Li showed how the bridging law could be derived. Based on the strength and energy criteria, Li has derived (eq. 2.2) for the critical fiber volume fraction.

$$V_f^{crit} = \frac{12 J_c}{g\tau(L_f/d_f)\delta_0} \qquad \textit{(eq. 2.2)}$$

Where:

- V_f^{crit} *Critical fiber volume fraction*
- J_c *Matric toughness*
- g *Snubbing factor, coefficient to raise the bridging stress of fibers which are inclined to the matrix crack plane*
- τ *Frictional bond property*
- L_f *Fiber length*
- d_f *Fiber diameter*
- δ_0 *Crack opening corresponding to maximum bridging stress*

This equation provides a guideline to tailor the micro-parameters such that the critical fiber volume fraction can be minimized by:

- reducing J_c. This can be achieved by adjusting the water cement ratio, and the aggregate volume, size and type.
- increasing τ. This can be done by modification of fiber surface, fiber deformation and transition zone. When improving the frictional bond property, one must be aware to avoid brittle failure by fiber rupture. By tailoring fiber length one also influences the d_f and δ_0. Longer fibers are preferred for the critical fiber volume fraction, but also decreases the workability of the plastic mix.

To quantitatively measure the margin of saturated cracking two performance indices are defined in [11], see (eq. 2.3) and (eq. 2.4). Where the former is based on the energy criteria and the latter on the strength criteria. PSH_{energy} can be improved by decreasing the J_{tip} through the reduction of matrix fracture toughness or by introducing a large flaw size. However these modifications can lead to respectively low compressive strength and low first crack strength under tension. $PSH_{strength}$ can be improved by increasing the fiber bridging strength or controlling the fiber-matrix interfacial bond

properties. In [12] Kanda proposed threshold values for the indices for PVA and PP fibers: $PSH_{strength}$ = 1.45 (PVA), and 2 (PP). and PSH_{energy} = 3 (both fibers) to achieve robust strain-hardening accounting for inhomogeneity in the composite.

$$PSH_{energy} = \frac{J'_b}{J_{tip}} \qquad \textit{(eq. 2.3)}$$

Where:

- J'_b *Complementary energy*
- J_{tip} *Crack tip toughness*

$$PSH_{strength} = \frac{\sigma_0}{\sigma_c} \qquad \textit{(eq. 2.4)}$$

Where:

- σ_0 *Fiber bridging capacity*
- σ_c *Matrix cracking strength*

2.2.4 COMPOSITE-CONSTITUENTS RELATION

SHCC is a cementitious composite reinforced with fibers. To study its behavior three main constituents should be considered [13]:

- The bulk cementitious matrix
- The fibers
- The fiber-matrix interface

Properties of each constituent will influence the properties of the composite. Table 2.4 gives an overview of some relevant constituent properties [1].

Table 2.4 Cement based fiber composite material constituents and their relevant properties [1].

Constituents	Properties
Matrix	Fracture toughness, Young's modulus, initial flaw size
Fiber	Young's modulus, tensile strength, length, diameter, volume fraction
Fiber-Matrix Interface	Bond properties, snubbing coefficient

2.2.4.1 MATRIX

The matrix of fiber reinforced cementitious composites is similar to that of normal cementitious composites. To tailor the properties given in Table 2.4, many parameters are of importance, one can alter the water to binder ratio w/b, cement type, properties of the filler materials (the type, size, content and particle size distribution) etc. Below a summary of useful information concerning the matrix strength is given [1, 7, 14,15]:

- The matrix cracking strength may not exceed the fiber maximum bridging stress to avoid rupture of the fibers during steady-state crack formation.
- For low fiber volume fractions: $J_{tip} \approx K_m^2/E_m$. Where small J_{tip} is enhancing the strain capacity. K_m can be calculated by LEFM techniques. E_m can be estimated with Hirsch formula.
- Incorporation of aggregates increases the fracture toughness due to crack deflection.

- To achieve saturated strain-hardening cracking, the index PSH_{energy} (eq. 2.3) should be larger than 3 to account for the material constituent variations along the length of the specimen. When J_{tip} is assumed to be 5 J/m^2.
- Flaw size is sensitive to mixing, placement and curing methods.

2.2.4.2 FIBERS

Application of fibers in FRC has been diverse. There is a great variety in [13]:

- material, e.g. steel, carbon, and glass
- surface treatment, e.g. profiled, and coatings
- fiber geometry, e.g. hooked at ends, bundled filaments, and fibrillated films
- fiber layout, e.g. continuous in mats and woven fabrics, and discontinuous in short discrete fibers.

Concerning the geometry of the fibers in FRC, two levels must be considered; the shape of the individual fibers and their dispersion in the cementitious matrices (Figure 1.2). During the development of SHCC, two desirable properties according to Li [1] were:

> *"Flexible processing – can be used in pre-cast or cast-in-place applications and no requirement of very special processing machinery. Short fibers of moderate volume fraction – to maintain flexible processing, reduce cost and weight."*

Although not necessarily a requirement according the definition of SHCC, the author of this thesis is in agreement with the reasoning of Li. Therefor this thesis solely focuses on the short discrete fibers.

There are many commercially available synthetic fibers. Their properties may vary considerably from manufacturer to manufacturer. Table 2.5 gives an overview of two commonly used synthetic fibers used in SHCC. In the beginning ultra-high molecular Polyethylene (PE) fibers were used, but due to the high material costs, Polyvinyl Alcohol (PVA) fibers has partially replaced PE fibers in the SHCC mix designs. One of the early problems of PVA fibers was its too high bond stress. This was caused by the strong chemical bond between the PVA fiber and matrix. Which led to delamination of the fiber during pullout. To decrease the chance of delamination oil coated PVA fibers have been successfully implemented. A more detailed description of this interaction will be discussed in chapter 2.2.4.3.

Table 2.5 Typical properties of commercially available synthetic fibers [13].

Fiber type	Diameter [µm]	Density [kg/m^3]	Tensile strength [MPa]	Elastic modulus [GPa]	Ultimate elongation [%]
Polyethylene	25-1000	920-960	80-600	5	3-100
PVA	14-650	1300	800-1500	29-36	5.7

Literature survey has led to the following list of useful information concerning fibers [9]:

- Fiber length and diameter are directly related to the surface area and the critical fiber volume. See (eq. 2.2).
- Increasing the fiber's Young's modulus will improve to the fiber-bridging stress.

2.2.4.3 FIBER-MATRIX INTERFACE

In conventional concrete there is an interfacial transition zone (ITZ). Which is located in the region of the cement paste around the aggregate particles, where higher porosity and predominance of smaller cement particles develops. A common view is that the ITZ is the weakest link in concrete, since micro-cracks due to loading predominantly develops in the ITZ [16]. In fiber reinforced cementitious composites, such as SHCC, there is an additional interface that should be considered. This interface is the fiber-matrix interface. Control of the fiber-matrix interface is essential to enable strain-hardening abilities of FRC.

The mechanism of the tensile strain-hardening is described in chapter 2.2. The bridging effect of the fibers is determined by the properties of the fiber-matrix interface. First debonding occurs, then some of the fiber pull out partly and slip-hardening occurs. When the specimen is saturated with multiple fine cracks the fibers will pull out completely or rupture, resulting in failure of the specimen. According to the authors of [13], three types of fiber-matrix interactions are of importance:

- Chemical
- Friction
- Mechanical anchorage induced by deformations on the fiber surface or by overall complex geometry

Where the latter is most important for steel fibers, the former two are important for the soft synthetic fibers. For the soft synthetic fibers the interfacial shear resistance is generally classified in two categories, i.e. friction-dominant type and chemical bond-dominant type. Figure 2.5 show different assumed shear stress distribution models [17]. The presence of the chemical bond diminishes the *C* as described in Table 2.3.

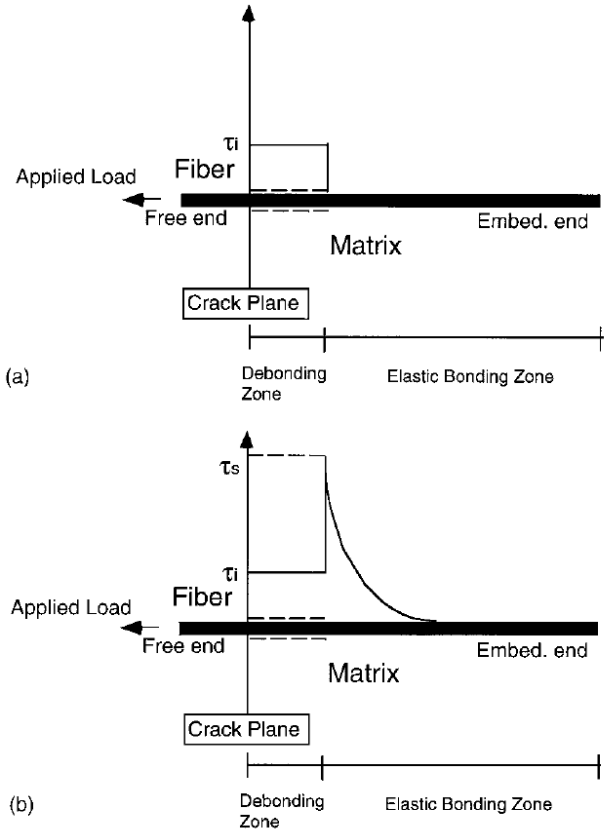

Figure 2.5 Assumption of shear stress distribution: friction only interface model (a); chemical bond and frictional interface model (b) [17].

In one research [7] it was mentioned that the PVA fiber exhibits the behavior in Figure 2.5 (b). This is caused by the hydroxyl group in the molecular chain of the PVA fiber. Due to the presence of this hydroxyl group, PVA fibers tend to develop a strong chemical bond with the cement. It is shown that this bond will decrease the complementary energy, thus decreasing the tensile capacity. The research found that untreated PVA fibers have shown barely multiple cracking behavior and a tensile strain capacity lower than 1 percent. In order to counter the effect of the chemical bond, the fibers were treated with multiple oil coating volumes. The effect of oiling on interfacial properties and micromechanical predictions of complementary energy are shown in Table 2.6. The model and method (single fiber pullout test) for the extraction of these interfacial properties are described in detail in [18]. According to [7] the optimum oil coating was 1.2% by the weight of the oil to the weight of the fibers. After this volume of oil coating, the authors found no further reduction of crack spacing. While increasing the oil content would further decrease properties as first crack strength and first tensile strength of the composite.

Table 2.6 Effect of oiling on interfacial properties and micromechanical predictions of complementary energy C [7].

Weight ratio oil to fiber	τ [MPa]	G_d [J/m^2]	β [-]	C [J/m^2]	C/J_{tip} [-]
0.0	2.44±0.49	4.71±0.58	2.21±0.71	3.64-6.63	0.73-1.33
0.3	2.15±0.19	3.16±0.66	2.31±0.19	5.17-13.8	1.03-2.76
0.5	2.14±0.15	2.96±0.75	1.82±0.23	7.68-13.6	1.54-2.72
0.8	1.98±0.13	2.18±0.39	1.18±0.34	12.5-20.7	2.50-4.14
1.2	1.11±0.13	1.61±0.60	1.15±0.17	24.2-38.1	4.84-7.62

Where:
- τ *Frictional bond*
- G_d *Chemical bond*
- β *Slip hardening coefficient*
- J'_b *Complementary energy*
- J_{tip} *Crack tip toughness (assumed to be 5 J/m^2)*

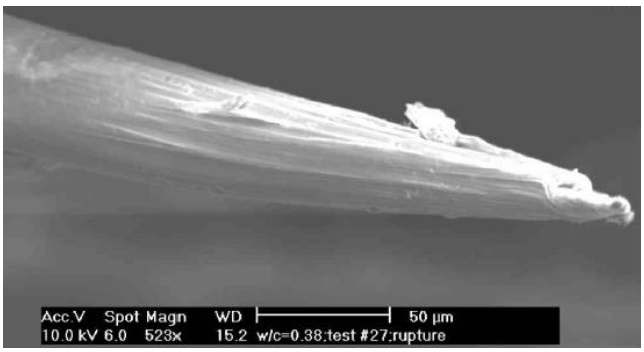

Figure 2.6 Ruptured end of non-oiled PVA fiber [7].

The hypothesis of the negative influence by the higher chemical energy were confirmed by the analysis of the PVA fiber behavior during pullout. Figure 2.6 depicts the fiber end of a non-oil treated PVA fiber [7]. It shows a pencil-sharpened shape at the fiber end, which can be explained by the matrix shaving the soft fiber. Since the tip travels the biggest distance during pullout it leads to this pencil-sharpened shape. The shaving process is depicted in Figure 2.7a. When the PVA fiber is non-oil coated the cross section was decreased by the shaving process to the amount that it cannot bridge the crack and premature fiber rupture occurs. Oil coated fibers however showed less delamination of the fiber and therefor lead to a lower crack spacing and bigger average crack width. Figure 2.7b shows the *P-u* curve, where the *P* is the applied load on the fiber and *u* the pull-out of the fiber. A sudden drop in load is exhibited after stage 3 where the fiber loses contact with the matrix. Due to delamination a smaller pullout segment l_{po} compared to the original embedment length l_e is found.

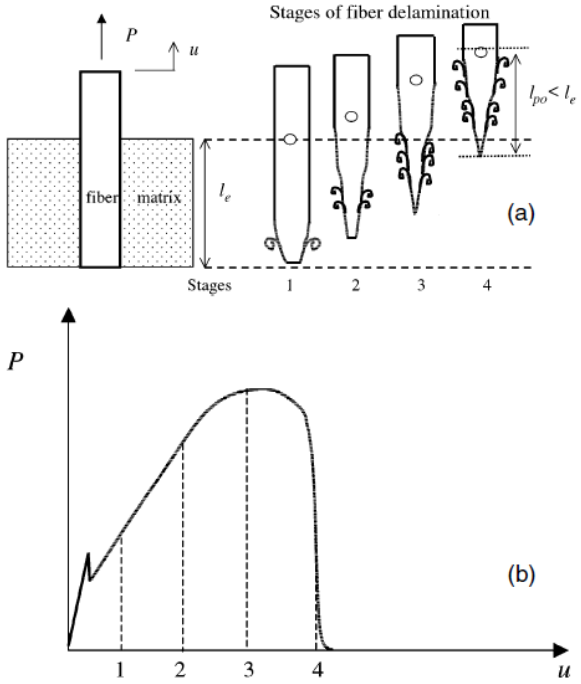

Figure 2.7 Fiber delamination during slip hardening (a) at various stages of pullout process illustrated on a P-u curve (b) [7].

Literature survey has led to the following list of useful information concerning the fiber-matrix interface [1, 7, 13,17]:

- Interface properties are very sensitive to fiber type, particle size distribution and processing.
- C and J_{tip} are tailorable through the parameters in shown in Table 2.3. Note: by minimizing J_{tip} certain mechanical behavior drop, e.g. compressive strength.
- Interface properties as τ, G_d *and* β, C can be determined with the single fiber pullout test (appendix A).
- Based on J_{tip} = 5 J/m^2, the optimal ranges of interfacial properties are G_d < 2.2 J/m^2, τ = 1.0 - 2.1 MPa and β < 1.5.
- Hydrophilic fibers may extract water from the matrix and swell.
- Examining the failure of the fiber may lead to interface properties optimization.

2.3 MIX DESIGN

2.3.1 GENERAL

In SHCC the strain-hardening ability of a composite is very sensitive to small alterations in the mix design. Due to this sensitivity SHCC mix designs proven in the USA or Japan may not show the same strain-hardening behavior when made in the Netherlands with local materials, because materials like cement, blast furnace slag (BFS), limestone powder (LP) etc. have a different chemical composition worldwide. For more information it is referred to Appendix B. Therefor a proven SHCC mix design of A past TU Delft research [19] will be described below.

In research [19] the goal was to replace ordinary Portland cement (OPC) with LP and BFS to lower the material costs and CO_2 emission. Moreover LP and BFS improves the fresh and hardened properties of

concrete, such as workability and durability. In order to simplify the mixing procedure, a mix design with BFS cement is developed to minimize the number of matrix materials (Table 2.7). The M1 mix design is based on the standard SHCC mix M45. Where M2-M4 investigates the optimum LP content. For the chemical composition of the used cement, LP, and BFS see the original research [19]. The water to powder ratio, w/p, is increased due to the higher water demand of BFS compared to FA. Then in M5 and M6 the BFS content increases. Finally a mix design with BFS cement was given. Fibers used in this study was the PVA fiber with a length of 8 mm and a diameter of 40 µm. The tensile strength of the PVA fiber is 1600 MPa and the density is 1300 kg/m^3. The surface of the fiber is oil-coated with 1.2% (by weight).

Table 2.7 Several SHCC mixtures with [19].

Mix	Type I cement	CEM III/ B 42.5 N	Silica sand	Fly ash	LP	BFS	W/p	SP	PVA fiber (by volume)
M45	1	-	0.8	1.2	-	-	0.2	0.013	2%
M1	1	-	-		0.8	1.2	0.27	0.025	2%
M2	1	-	-		1.5	1.2	0.27	0.023	2%
M3	1	-	-		2	1.2	0.26	0.018	2%
M4	1	-	-		3	1.2	0.26	0.018	2%
M5	1	-	-		2	1	0.26	0.018	2%
M6	0.6	-	-		2	1.4	0.26	0.020	2%
M-CEM III*	-	1	-	-	1	-	0.26	0.020	2%

**Author of [19] did not give a mix number to this mix, in future reference this mix is named M-CEM III*

Specimens were prepared and tested in UTT, 4-PBT and compressive test. Additionally loaded crack width measurements were performed. For the test setups it is referred to [19]. Table 2.8 shows the flexural deflection capacity and tensile strain capacity of SHCC at 28 days. Mix M6 show the best highest flexural deflection and tensile strain capacity. The M-CEM III is designed for easier mixing and is based on M6 (almost the same OPC, BFS, and LP content).

Table 2.8 Flexural deflection capacity and tensile strain capacity of SHCC at 28 days.

	M1	M2	M3	M4	M5	M6	M-CEM III
Flexural deflection capacity [mm]	2.0±0.1	3.2±0.8	3.8±1.0	3.3±0.7	3.8±0.4	3.9±0.3	*
Tensile strain capacity [%]	1.7±0.3	2.4±0.5	3.1±0.6	2.6±0.5	3.1±0.3	3.3±0.2	3.1±*

** Not provided by author.*

2.3.2 ADDITIVES

Additives such as superplasticizer (SP) and viscosity modifying agent (VMA) are used to control the rheological properties of the fresh mix, which in turns can predict mechanical behavior [14]. The influences of these additives on the mechanical strength and rheological properties of the fresh mix will be described.

SP, also known as high range water reduce, is a admixture that can be added to the mix to either [20]:

- increase workability without changing the mix composition in order to enhance workability characteristics of concrete
- reduce the mixing water and the water-cement ratio in order to improve strength and improve durability at a given workability
- educe both water and cement at a given workability in order to save cement and reduce creep, shrinkage and thermal strains caused by heat of cement hydration.

Another admixture is the VMA. Addition of a VMA to the mix causes the plastic viscosity to increase [21].

In [14] the relation of the ratio of class C and F FA, the w/b, SP, and VMA versus the plastic viscosity, relative yield stress, ultimate tensile strength and tensile strain capacity were investigated. The SP used is a polycarboxylate-based SP with solids content of 30%, and the VMA based on hydroxypropylmethylcellulose. The findings of this research are summarized in Table 2.9.

Table 2.9 Effect of variables on different responses of SHCC [14].

Response	**Performance characteristics**	**C/F (↑)**	**w/b (↑)**	**SP/B (↑)**	**VMA/B (↑)**
Plastic viscosity	Bigger is better	(+1)	-4	-3	+2
Relative yield stress	Smaller is better	-3	+1	+4	?2
Ultimate yield strength	Bigger is better	+3	-4	-2	(-1)
Tensile strain capacity	Bigger is better	+4	-3	?1	+2

Where:

- *C/F* — *ratio of class C and class F FA*
- *w/b* — *water to binder ratio by mass*
- *SP/B* — *superplasticizer-binder ratio by mass*
- *VMA/B* — *VMA – binder ratio by mass*

Note: + is positive impact on performance requirement; - is negative impact on performance requirement; ? is uncertain trend of impact; 4 is the highest impact; 1 is lowest impact; and () is insignificant/unpooled factor

From Table 2.9 it can be seen SP and VMA can be added to adjust respectively the plastic viscosity and relative yield stress.

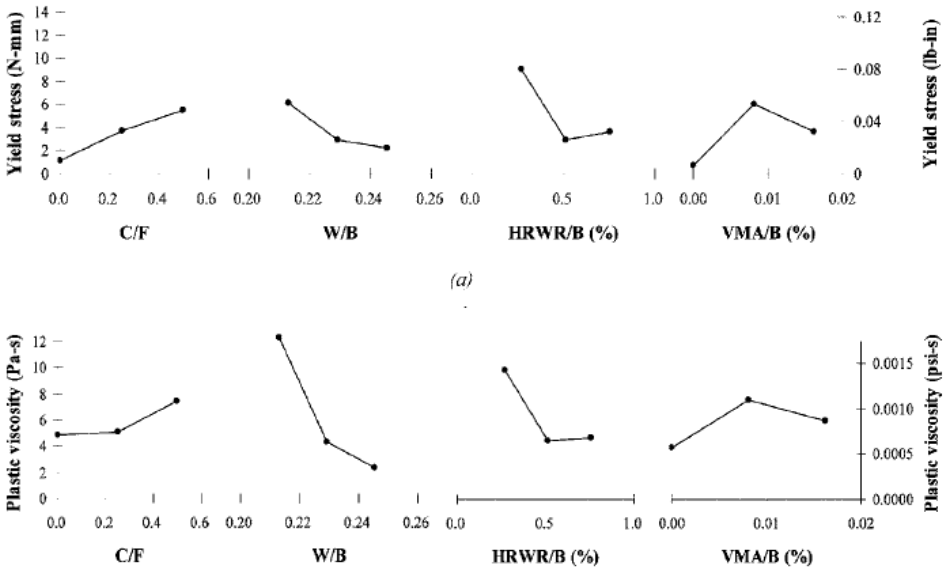

Figure 2.8 The effect of each variable on: relative yield stress (top), and plastic viscosity of SHCC mortar (bottom) [14].

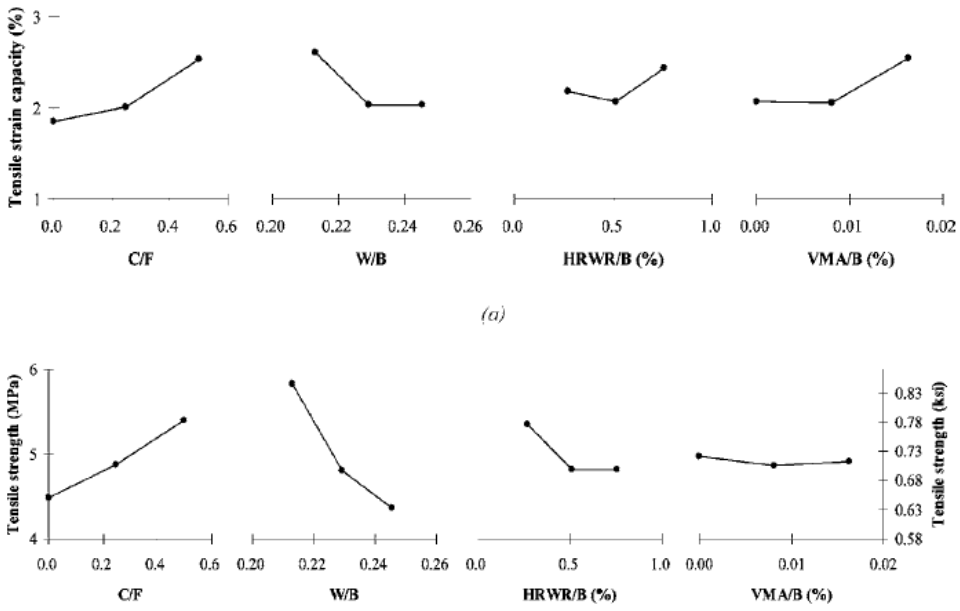

Figure 2.9 The effect of each variable on: tensile strain capacity (top), and ultimate tensile strength of SHCC (bottom) [14].

Figure 2.8 shows the effect of each variable on the relative yield stress and plastic viscosity of the SHCC mortar. It should be noted that the SP and VMA show a reverse of trend at respectively 0.51% by mass and more than 0.008% by mass. Figure 2.9 shows the effect of each variable on the strain capacity and ultimate tensile strength of SHCC. This suggest “saturation points” of the chemical admixtures, where the SP dosage beyond this point does not decrease the flow time of the fresh mortar [22].

Based on the findings, the researchers in [14] recommended that a w/b in the range of 0.25 ± 0.05 is adopted in the SHCC mixture. While a high plastic viscosity (high Marsh cone flow time) and low yield stress (high mini-slump flow diameter) can be achieved through adjustment of the amount of SP.

2.4 MIXING, PLACEMENT, AND CURING PROCEDURE

While proper mix design is essential for strain-hardening behavior, one must not forget the importance of mixing, placement, and curing procedure. These three procedures have significant impact on the composite behavior. Many researches have been dedicated to these procedures. In [23] a mix procedure is given for large scale processing on site. While in [11] the effect of the mixing procedure and curing conditions on the mechanical performance of a polypropylene fiber based SHCC is shown. Lastly, in [24] the research showed evidence that the casting direction influences the fiber orientation.

2.4.1 MIXING PROCEDURE

In [23] the mixing procedure is designed for large scale processing on site. The goal was to achieve comparable mechanical properties of the ECC-M45 produced in the lab (compressive strength, tensile strength and tensile strain capacity are respectively 60 MPa, 4.35 MPa and 2.0%) while using traditional on site mixing equipment in a reasonable amount of time.
Compared to the high shear energy mixers in the lab, the mixers on site or on transit trucks are mainly gravity-powered low-energy paddle mixers. To ensure adequate workability of the material a successful material design was achieved by tailoring the grain size distribution of the mortar mix. By using the improved Fuller curve by Funk and Dinger it was possible to design a mix that required minimum mixing energy.

For the design of the mixing process three pre-determined requirements were set. The material must remain highly fluid throughout the entire mixing process and through the addition of fibers in the last mixing step. Secondly, the material should be nearly homogeneous after a short mixing time and immediate prior to adding the fibers. Lastly, the mixing time is kept to a minimal to keep pace with the ongoing operations at the concrete batching plants. Several designs were tested for a small scale mixer (200 L) and a large scale mixer (3000 L). The best mixing procedure complying to the aforementioned goal and pre-determined requirements is shown Table 2.10.

Table 2.10 Large scale SHCC batching sequence times [23].

Activity no.	Activity	Elapsed time (minutes)
1	Charge all sand	2
2	Charge approximately 90 to 95% of mixing water, all superplasticizer, all hydration stabilizer	2
3	Charge all fly ash	2
4	Charge all cement	2
5	Charge remaining water to wash drum fins	4
6	Mix at high rpm for 5 minutes or until material is homogeneous	5
7	Charge fibers	2
8	Mix at high rpm for 5 minutes or until material is homogeneous	5
	Total	24

Steps 6 and 8 are to accommodate the absence of large aggregates which normally agitate the materials within the mixing drums. The advised amount of time is 5 to 10 minutes. The hydration stabilizer at step 2 is at a dosage of 300 mL per 100 kg cement to maintain a minimum flowability value for 30 minutes for transport in transit trucks.
With this research it is shown that it is possible to design a material and mix process that at least the mechanical properties of ECC-M45 tested in lab, while also taking into consideration the available traditional mixing equipment and minimizing the mixing time.

In [25] the influence of the sequence of the mixing procedure on the fiber distribution and mechanical properties of SHCC was researched. Table 2.11 shows the standard and adjusted mixing sequence. In the adjusted mixing sequence the aim is to first achieve desired plastic viscosity for good fiber distribution (step 2 of adjusted sequence). Then the fibers are added in step 3, and in step 4 rest powder and liquid materials are added to tailor the workability and hardened properties of the composite. The specimens produced with the adjusted sequence showed improved tensile stress-strain diagrams (Figure 2.10) and better fiber distribution. The fiber distribution is evaluated by calculating the fiber distribution coefficient based on a grid analysis.

Table 2.11 Standard and adjusted sequence of mixing procedure according to [25].

Steps	**1**	**2**	**3**	**4**
Standard sequence	Mix all powder materials	All liquid materials are added and mixed (1 min low speed then 2 min high speed)	Fibers are added and mixed (4 min high speed)	-
Adjusted sequence	Mix proper amount of powder materials	Proper amount of liquid materials is added and mixed (1 min low speed then 2 min high speed)	Fibers are added and mixed (2 min high speed)	The rest powder and liquid materials are added. (2 min high speed)

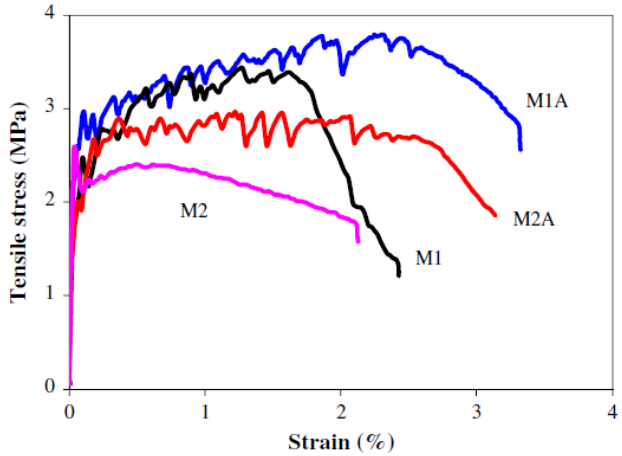

Figure 2.10 Typical uniaxial tensile stress-strain diagram of the for SHCC mixtures. M1 and M2 were mixed following the standard mixing sequence, and M1A and M2A were mixed following the adjusted mixing sequence [25].

The fiber distribution of M1A and M2A (A stands for adjusted sequence of mixing procedure) are respectively 8% and 24% higher than that of M1 and M2. Good correlation between fiber distribution and tensile strain capacity was found.

2.4.2 PLACEMENT PROCEDURE

In [24] it was shown that the placement procedure significantly influences the fiber orientation, hence the mechanical behavior of the composite. In the research the fiber orientation was manipulated by either placing the material parallel or transversal to the longitudinal direction of the beam (Figure 2.11). For the mechanical tests three-point bending tests (3PBT) with specimens of 100*100*400 mm were performed. Hereafter image analysis (see chapter 4.2) is performed to extract probability density function (PDF) of the fiber distribution in the specimen. This was coupled to the mechanical performance. The following observations and conclusions were made:

- The calculated fiber bridging behavior is from good to worse: parallel placing, transversal placing, 2D, and 3D (Figure 2.12).
- The maximum load carried by parallel is around 30 % higher than transversal placed concrete.
- The fiber per unit area, which is closely related to fiber orientation distribution, of parallel was also roughly 50 percent higher than that of transversal placed concrete.
- PDF of the fiber angle with relation to the loading axis show that the PL is left skewed and TL is right skewed (Figure 2.13).

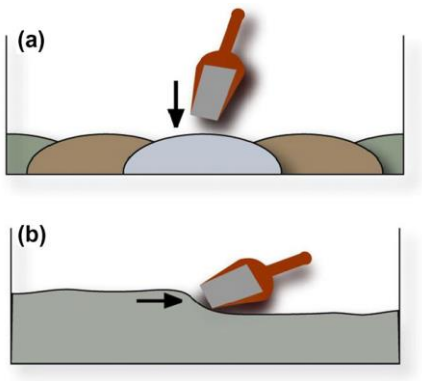

Figure 2.11 Specimen preparation by placing the concrete transversal to the tensile direction of the specimen (a) or parallel to the tensile direction of the beam (b).

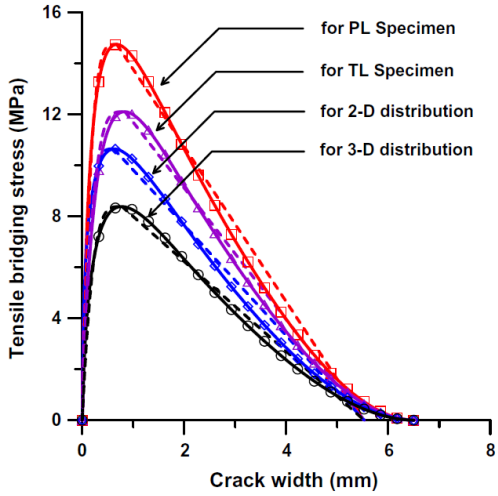

Figure 2.12 Comparison of the simplified diagrams with the fiber bridging behaviors obtained from the fiber orientation distribution [24].

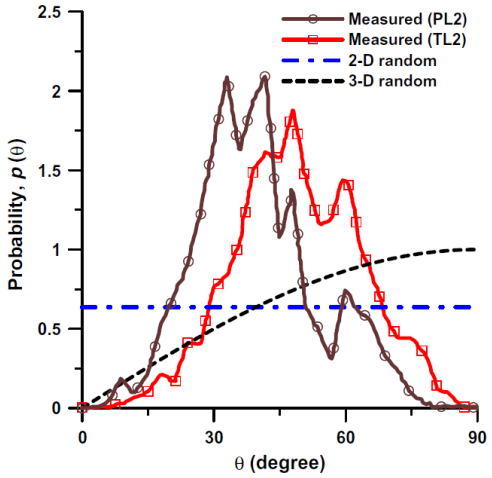

Figure 2.13 Comparison of PDF for different fiber orientation distributions [24]. PL and TL for respectively parallel and transversal placement with regard of the longitudinal direction of the specimen.

2.4.3 CURING PROCEDURE

Research in [11] also investigated the effect of the curing regime on the SHCC specimen. Three different regimes were investigated and shown in Table 2.12.

Table 2.12 Three different curing regimens in [11].

Curing method	**Temperature [°C]**	**Relative humidity [%]**
Laboratory condition for 28 days	23 ± 3	45 ± 5
Water for 7 days and then room temperature until 28 days	23 ± 3	45 ± 5
Water for 28 days	23± 3 °C	-

It was found that the average tensile ductility is significantly higher for water-cured specimen compared to air-cured specimen. However tensile strength remains nearly the same. Crack opening at bridging capacity decreased with water curing. The main reason for this is the increased fiber-matrix frictional bond. Water curing in comparison with air curing decreased the matrix toughness and increase the fiber bridging capacity. Water curing is effective for HTTP-SHCC due to improved fiber-matrix interface frictional bond strength. This is will not be the case for PVA-SHCC where the interface frictional bond strength was decreased deliberately with an oil coating.

2.5 UPSCALING OF ELEMENT SIZE

According the plastic theory (or strength theory) materials have a material strength or yield limit. Failure or yielding of an element will occur when this material strength or yield limit is exceeded. Regardless of the size of the element, as long it is from the same material, the material strength or yield limit is identical. However as Leonardo da Vinci already has observed:

> *"among cords with equal thickness the smallest is the strongest"*, and *"a cord is so much stronger… as it is shorter"* [26].

Any deviation from the notion that differently sized elements consisting of the same material have the same material strength is known as size-effect.

Size-effect in concrete may have many sources, According to [27] these are:

- Wall effect, influence of material dispersion and/or orientation due to the boundary effect imposed by the surface of the mold. For example in concrete adjacent to the mall has relatively less particles and more fine particles in comparison with the interior.
- Diffusion phenomena can change the material properties and produce residual stresses. These diffusion processes are proportional to the square of the sizes of the structure.
- Hydration heat is proportional to the square of the sizes of the structure.
- Statistical size-effect which causes randomness in material strength. Which is described in the well-known Weibull's weakest link statistics. However, unlike in metallic and other structures where from microscopic flaws turns into the initiation of a macroscopic crack which causes the structure to fail, in concrete fail only after a large growth of stable crack zone or fracture. Making statistical randomness outside this zone irrelevant.
- Fracture mechanics size-effect, due to the release of stored energy into the fracture front which increases with element size.
- Fractal nature of crack surface.

One of the earlier explanation of size-effect in concrete is the Weibull's weakest link theory. A chain consisting of multiple rings is as strong as the weakest ring. Where the strength of the ring is dependent on flaws in the material structure, which in its turn is of statistical nature. However in concrete this does not always hold true, as a fracture process zone with stable crack grow might develop before the concrete element fails after the developments of a macroscopic crack. Granted, there are several cases where the Weibull's weakest link theory holds true, e.g. thick plain unreinforced structures [28]. Furthermore many tests show a size-effect much stronger that can be predicted by Weibull's weakest link theory [29].

Another source of size-effect is the fracture mechanics size-effect. This source is based on the theory of Linear Elastic Fracture Mechanics (LEFM), and of deterministic nature as opposed to the statistical

nature of Weibull's weakest link theory. It has been found that quasi-brittle material follow theory of plasticity (or strength theory) on small scale, characterized by the material strength or yield limit. On large scale it follows the theory LEFM, characterized by fracture energy í.
LEFM is a basic theory that describes the behavior of any material with cracks. When a crack is present in an elastic body, the stress redistributes around the crack, and concentrates at the crack tip. However Griffith noted that in a sharp crack infinite stress would be present at the crack tip [30]. He also concluded that for the crack formation a certain energy per unit area of the crack plane was needed, often denoted as G_f. Based on this energy approach and contribution of many others, it has been derived that size-effect exists, following a power law. Which describes that the nominal strength is proportional to the inverse square root. The nominal strength will decrease with $D^{-1/2}$ where D, a characteristic dimension, is increased [27].

The last mentioned source of size-effect is proposed in [31] and proposes to identify parameters as the fracture energy of a material with fractals. Fractals are mathematical sets that repeat a set pattern at each scale. This could explain why higher fracture energy is found in specimens of bigger size.

REFERENCE LIST PART II

[1]Li, V. C. (1998). Engineered Cementitious Composites-Tailored Composites Through Micromechanical Modeling.
[2] Li, V. C. (2008). Engineered Cementitious Composites (ECC) Material, Structural, and Durability Performance.
[3] Sahmaran, M., Lachemi, M., Hossain, K. M., Ranade, R., & Li, V. C. (2009). Influence of aggregate type and size on ductility and mechanical properties of engineered cementitious composites. ACI Materials Journal, 106(3).
[4] Van Zijl, G. P. A. G., & Boshoff, W. P. (2008). Mechanisms of creep in fibre-reinforced strain-hardening cement composites (SHCC).
[5] Li, V. C. (2003). On engineered cementitious composites (ECC). Journal of advanced concrete technology, 1(3), 215-230.
[6] Yang, E. H., Wang, S., Yang, Y., & Li, V. C. (2008). Fiber-bridging constitutive law of engineered cementitious composites. Journal of advanced concrete technology, 6(1), 181-193.
[7]Li, V. C., Wu, C., Wang, S., Ogawa, A., & Saito, T. (2002). Interface tailoring for strain-hardening polyvinyl alcohol-engineered cementitious composite (PVA-ECC). ACI Materials Journal, 99(5).
[8] Marshall, D. B. and Cox, B. N. (1988). A J-integral method for calculating steady-state matrix cracking stresses in composites. Mechanics of Materials, (8), 127-133
[9] Yang, E. H., Wang, S., Yang, Y., & Li, V. C. (2008). Fiber-bridging constitutive law of engineered cementitious composites. Journal of advanced concrete technology, 6(1), 181-193.
[10] Li, V.C., Post-Crack Scaling Relations For Fiber Reinforced Cementitious Composites, ASCE J. of Materials in Civil Engineering, 4(1) 1992, pp. 41-57.
[11] Felekoglu, B., Tosun-Felekoglu, K., Ranade, R., Zhang, Q., & Li, V. C. (2014). Influence of matrix flowability, fiber mixing procedure, and curing conditions on the mechanical performance of HTPP-ECC. Composites Part B: Engineering, 60, 359-370.
[12] Kanda, T. (1998). Design of engineered cementitious composites for ductile seismic resistant elements.
[13] Arnon, B., & Sidney, M. (2007). Fiber reinforced cementitious composites. I)(second edition). London: Taylor & Francis Group.
[14] Yang, E. H., Sahmaran, M., Yang, Y., & Li, V. C. (2009). Rheological control in production of engineered cementitious composites. ACI Materials Journal,106(4).
[15] Kanda, T., & Li, V. C. (1998). Multiple cracking sequence and saturation in fiber reinforced cementitious composites. JCI Concrete Research and Technology,9(2), 19-33.
[16]Scrivener, K. L., Crumbie, A. K., & Laugesen, P. (2004). The interfacial transition zone (ITZ) between cement paste and aggregate in concrete. *Interface Science*, *12*(4), 411-421.
[17] Kanda, T., & Li, V. C. (1999). Effect of fiber strength and fiber-matrix interface on crack bridging in cement composites. Journal of Engineering mechanics, 125(3), 290-299.
[18] Lin, Z., Kanda, T., & Li, V. C. (1999). On interface property characterization and performance of fiber reinforced cementitious composites. Concrete Science and Engineering, 1(3), 173-184.
[19] Zhou, Jian, et al. "Development of engineered cementitious composites with limestone powder and blast furnace slag." Materials and Structures 43.6 (2010): 803-814.
[20] Collepardi, M. (1998). Admixtures used to enhance placing characteristics of concrete. Cement and Concrete Composites, 20(2), 103-112.
[21] Leemann, A., & Winnefeld, F. (2007). The effect of viscosity modifying agents on mortar and concrete. Cement and Concrete Composites, 29(5), 341-349.
[22] Agullo, L., Toralles-Carbonari, B., Gettu, R., & Aguado, A. (1999). Fluidity of cement pastes with mineral admixtures and superplasticizer—a study based on the Marsh cone test. *Materials and Structures*, *32*(7), 479-485.
[23] Lepech, M. D., & Li, V. C. (2008). Large-scale processing of engineered cementitious composites. ACI Materials Journal, 105(4).
[24] Kang, S. T., & Kim, J. K. (2012). Investigation on the flexural behavior of UHPCC considering the effect of fiber orientation distribution. *Construction and Building Materials*, *28*(1), 57-65.

[25] Zhou, J., Qian, S., Ye, G., Copuroglu, O., van Breugel, K., & Li, V. C. (2012). Improved fiber distribution and mechanical properties of engineered cementitious composites by adjusting the mixing sequence. Cement and Concrete Composites, 34(3), 342-348.

[26] Williams, E.: Some observations of Leonardo, Galileo, Mariotte and others relative to size-effect. Annals of Science 13 (1957) 23±29; da Vinci, L. (1500's) ± see The Notebooks of Leonardo da Vinci (1945) Edward McCurdy, London (p. 546); and Les Manuscrits de LeÂonard de Vinci, transl. in French by C. Ravaisson-Mollien, Institut de France (1881±91), Vol. 3

[27] Bazant, Z. P., & Planas, J. (1997). Fracture and size-effect in concrete and other quasibrittle materials (Vol. 16). CRC press.

[28] Bažant, Z. P. (1999). Size-effect on structural strength: a review. Archive of applied Mechanics, 69(9-10), 703-725.

[29] BazŸant, Z. P.; Planas, J.: Fracture and Size-effect in Concrete and Other Quasibrittle Materials. Boca Raton: CRC Press 1998

[30] Griffith, A. A. (1921). The phenomena of rupture and flow in solids. Philosophical transactions of the royal society of london. Series A, containing papers of a mathematical or physical character, 163-198.

[31] Carpinteri, A. (1994). Fractal nature of material microstructure and size-effects on apparent mechanical properties. Mechanics of Materials, 18(2), 89-101.

PART III: EXPERIMENTAL WORK

3 GENERAL SIZE-EFFECT

3.1 INTRODUCTION

Literature survey has not convincingly shown whether there is a significant size-effect in SHCC. The purpose of this experimental series is to determine whether significant size-effect exists in SHCC. In this experimental series no classification of sources of size-effect is made. Therefor this size-effect is called the general size-effect. Multiple sources of size-effect, e.g. the Wall effect, diffusion phenomena, hydration heat, statistical, and fracture mechanics are included. This can be done by comparing two differently sized specimens which are geometrically similar in three dimensions. The nominal strength, strain capacity, and crack pattern after loading will be compared.

3.2 OVERVIEW OF MECHANICAL TESTS

There are numerous tests to find mechanical properties of a material. In this chapter a selected number of tests are discussed, these are the uniaxial tensile test (UTT), 3- or 4-point bending tests (3- or 4-PBT), and cube or cylindrical compressive tests. Table 3.1 shows the mechanical properties with their corresponding test methods.

Table 3.1 Common test methods to assess mechanical properties of SHCC specimen.

Mechanical properties	**Test methods**
Tensile	Uniaxial tensile test (UTT)
Compressive	Cubic compressive test Cylindrical compressive test
Flexural	3-point bending test (3-PBT) 4-point bending test (4-PBT)

3.2.1 TENSILE TEST

The UTT is a direct test to investigate whether the specimen exhibits strain-hardening in tension. In the UTT dumbbell shaped specimen, also known as dog-bone specimen, are clamped and glued between steel or aluminum plates at both ends. The stress between the specimen and plates are now strictly transferred with friction. Figure 3.1 shows an example of such a setup. On both sides of the specimen a LVDT can be placed to measure the displacement. By comparing the two LVDT, one can check whether the specimen is indeed loaded in direct tension. In case of an eccentricity, uneven loading will result in differences in the two LVDT. Which means the specimen was subjected to bending load [1].

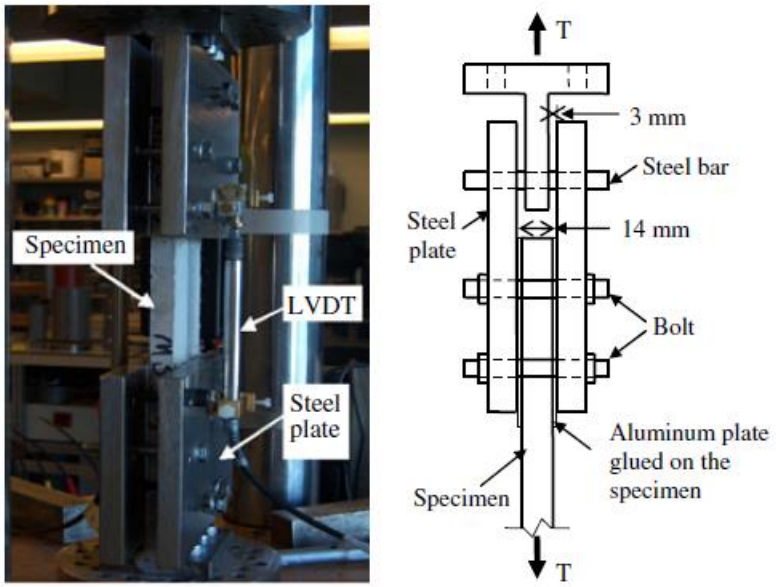

Figure 3.1 Uniaxial tensile test setup as in [19].

It is known that the UTT procedure is difficult to perform and requires experienced personnel. This is due to its high sensitivity to eccentricity which can be introduced many sources, such as the specimen preparation, testing apparatus eccentricities and mounting of specimen. Furthermore additional procedures, such as sandblasting and cleaning of the specimen, may be required to ensure good bond between the glue and the specimen. Due to these difficulties, several researches have attempted to find a more robust and easier to perform experiment [2, 3]. It is found that strain-hardening of the specimen in the flexural tests (3PBT and 4PBT) have strong correlation with strain hardening of the specimen in the UTT. In [3] a method to convert the deflection capacity from a 4-PBT into a strain capacity of the UTT was proposed. For the conversion a master curve describing the relation between deflection capacity and strain capacity has to be constructed first.

3.2.2 COMPRESSIVE TEST

In a compressive test different shaped specimens can be tested, such as the cubical and cylindrical shaped specimen. The test specimen will be put between two steel plates and pressed under a certain load rate. When the specimen has failed the machine will automatically stop and give the failure load. Instead of the steel plates different medium can be put between the specimen and the pressing jacks. Examples of this are steel brushes or a Teflon layer. These will reduce the contact friction between the specimen and the object that is in contact with the specimen. Leading to lower compressive strength compared to steel plates.

3.2.3 FLEXURAL TESTS

Due to the difficult execution of the UTT, flexural test are often used as replacement to indicate strain-hardening behavior. As noted earlier, strong correlation have been found between strain-hardening behavior in UTT, and 3- or 4-PBT. In addition, when a master curve of one SHCC mix describing the correlation between the deflection capacity from a flexural test and the strain capacity form a UTT is constructed, one can convert the deflection capacity into the strain capacity.

In the flexural test a bending moment are introduced in the specimen. A 3-PBT introduces a peak moment in the specimen, while a 4-PBT introduces an area with constant maximum moment (Figure 3.2).

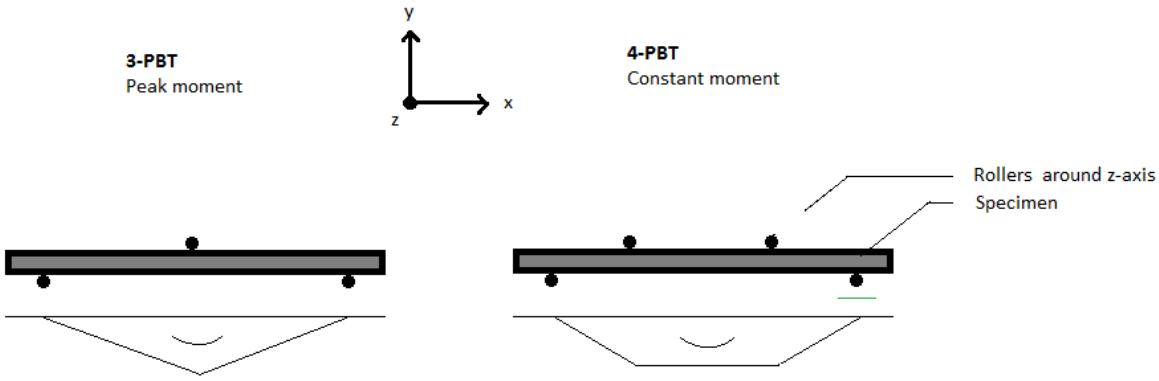

Figure 3.2 3-PBT (left) and 4-PBT (right) moment fields.

Typically 3-PBT are used for homogeneous materials and 4-PBT for inhomogeneous materials. In an inhomogeneous material the weakest cross section of the specimen can be along the whole specimen. So in a 4-PBT there is a larger chance the weakest cross section will fall in between the region with maximum flexural stresses. Thus for SHCC the choice for a 4-PBT is logical when one wants to measure the strain development of the specimen. In a 4-PBT it is expected that the first crack will initiate somewhere along the constant maximum moment field (Figure 3.2), then slip-hardening of the fibers in that crack occurs, and another crack will start to initiate along the constant moment field. For a 3-PBT the maximum moment is concentrated at one point at the middle support (Figure 3.2), it is expected that the first crack will also initiate here. Than the fibers at this crack will slip-harden and strengthen the cross section. However, there is high possibility that the slip-hardening is not adequate enough in order to have crack initiation elsewhere along the specimen, because there a lower moment is present. This will prevent the development of multiple fine cracks.

3.3 RHEOLOGICAL PARAMETERS: PLASTIC VISCOSITY AND YIELD STRESS

The rheology of fresh mortar, generally assumed to be a non-Newtonian fluid, is often described by the Bingham model. According to this model fresh mortar must overcome a yield stress before it can flow. Once it starts to flow shear stress increases linearly with an increase of strain rate. The slope of the strain rate defines the plastic viscosity. Thus the plastic viscosity determines how easily material can flow after the yield stress is overcome [4].

As research in [4] points out, depending on the mixer equipment, mixing procedures, local ingredients, and mixing personnel's experience a large variation in the tensile behavior of SHCC materials can be found. In this particular research an identical mix design, produced in the same mixer, showed tensile strain capacity ranging from 0.6% to 3.4% in different batches (Figure 3.3). However, it was found that control of the rheological parameters, plastic viscosity and yield stress, led to improved fiber dispersion and a more consistent tensile strain capacity in the composite.

A specific range of plastic viscosity was found to be desired. As this makes it possible for adequate mixing energy to be asserted to the mixture for good fiber distribution. However too high plastic viscosity may lead to larger air voids, introduced by high energy mixing for an extended time. In this study the plastic viscosity could be modified by using a VMA. The plastic viscosity was measured indirectly with the Marsh cone flow test. For this specific mix composition, mix procedure and test setup the optimal Marsh cone flow time is between 24 and 33 seconds, and a VMA dosage of 0.02-0.03 % of cement weight.
The yield stress is important for the self-compacting ability of the fresh SHCC. An indirect test with good correlation with the direct measurement of the yield stress is the (mini-)slump test. In research [11] it was noted that increased SP dosage will decrease the yield stress, which is preferred for the casting procedure. However visual observations showed that high dosages of SP will lead to mixtures that are more susceptible to bleeding and clumping of fibers.

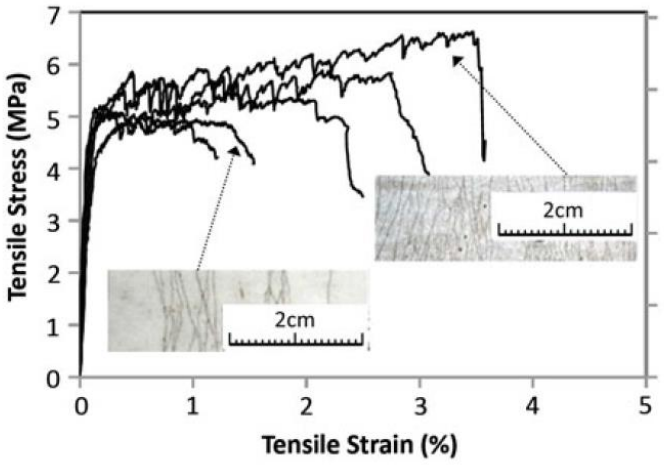

Figure 3.3 An extreme case of variation in tensile stress-strain diagram of SHCC made from the same batch [4].

To control the rheological parameters one can vary in the dosage of the SP and VMA, the amount and type of FA, and the w/b. The effects of these factors on the yield stress and plastic viscosity are described in chapter 2.3.2.

3.4 EXPERIMENTAL SET-UP

3.4.1 MECHANICAL TEST – 4-PBT

The 4-PBT is performed in the setup shown in Figure 3.4. The arrows show the direction of loading from the supports. The supports consists of a steel rods. Due to available lab equipment it is chosen to load the two differently sized specimens in reversed direction. This could influence the results due to the self-weight of both specimens, where in the standard specimens the self-weight is in the opposite direction of the applied force, and in the big specimens in the same direction of the applied force. The machine used is the INSTRON 8872, which has a loading capacity of 10 kN.

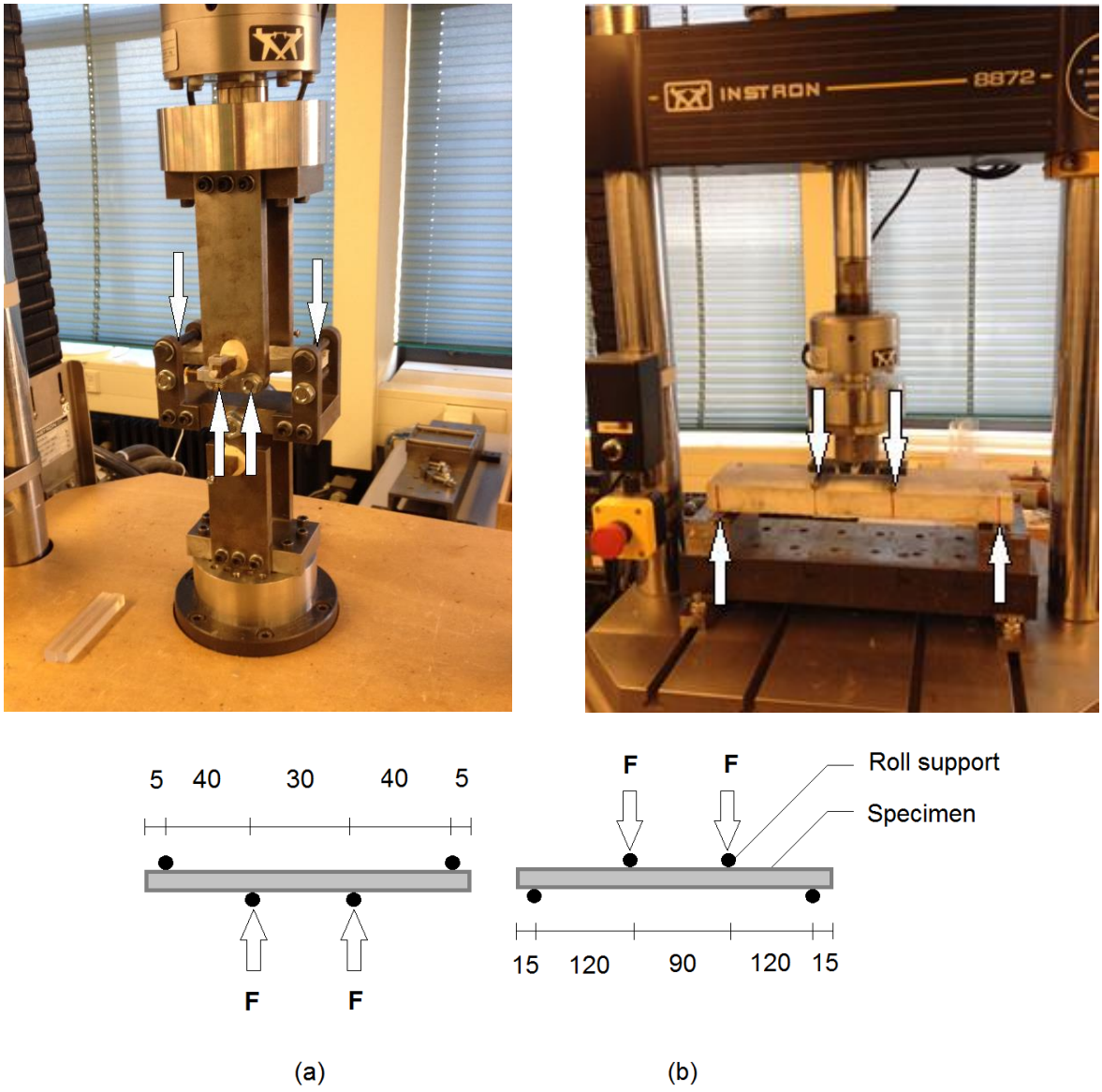

*Figure 3.4 4PBT setup for the 120*30*10 mm^3 specimen (a) and 360*90*30 mm^3 (b). All dimensions are in [mm].*

3.4.2 WORKABILITY TESTS: MARSH CONE AND V-FUNNEL TEST

As mentioned in chapter 3.3 two important rheological parameters can predict the fiber dispersion, hence the mechanical behavior and self-compacting ability of SHCC. These are the yield stress and plastic viscosity. Which can be measured directly with the rotational viscometer. However, the V-funnel flow time and mini-slump diameter tests (Figure 3.5), which are easier to perform, have shown strong correlation with respectively the plastic viscosity and yield stress [5,6,16]. The inner dimensions of these testing equipment used in this experimental series are depicted in Figure 3.5.

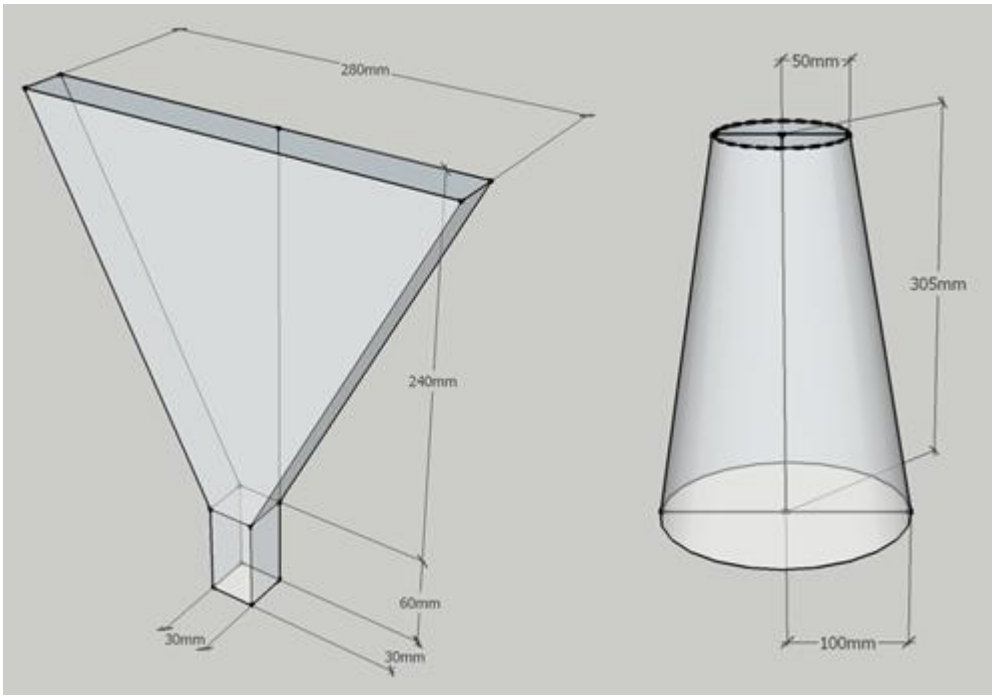

Figure 3.5 Inner dimensions for the workability tests: V-funnel test (left), and Mini-slump test (right).

3.5 EXPERIMENTAL PROCEDURE

3.5.1 INTRODUCTION

Two differently sized geometrical similar specimens will be compared with each other. Due to the available equipment one specimen size is 120*30*10 mm^3. This specimen will be compared with a specimen of 360*90*30 mm^3 (
Figure 3.6). By upscaling all dimensions by a factor 3 it was possible to test the two differently sized specimens in the same experimental setup, which will exclude possible bias introduced by different testing apparatus. Furthermore it was expected that the chosen fiber length to specimen height ratio may lead to a size-effect induced by fiber orientation.

In this experimental series it is chosen to apply flexural tests in favor of the UTT, because this would allow a direct comparison between the results of this experimental series and chapter 4. Where in chapter 4 it was not realistic to use dumbbell shaped specimens due to the sawing techniques applied there. Furthermore strain-hardening behavior in flexural tests has shown strong correlation with those found in UTT. For the reasons stated in chapter 3.2.3, it has been chosen to perform the 4-PBT instead of the 3-PBT.

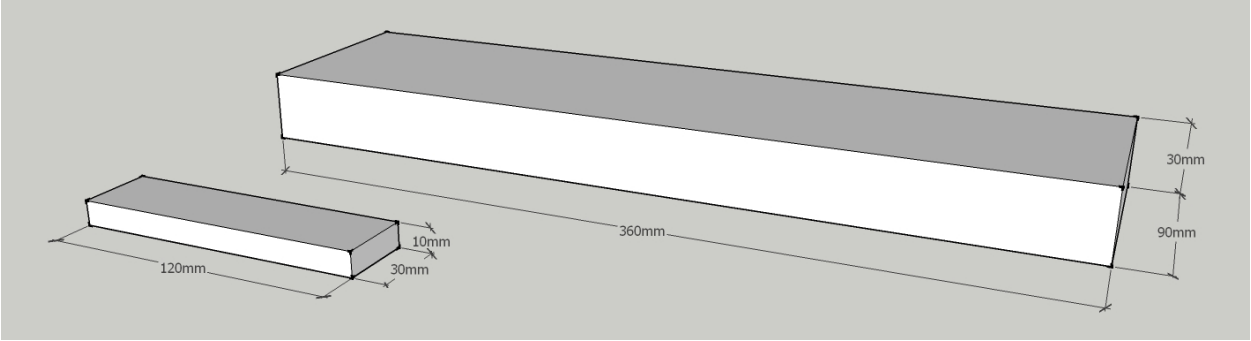

Figure 3.6 Dimensions of the 3-dimensional geometrically similar specimens.

After specimen preparation, which includes a workability test to ensure self-compacting SHCC, all specimens will be tested in a 4-PBT. Subsequently image analysis will be performed to characterize the crack pattern of the specifically loaded specimens. This will be described in chapters 3.5.4 and 3.6.5.

3.5.2 SPECIMEN PREPARATION

The mix design for this experimental series is shown in Table 3.2. The type of SP used is Glenium 51. The PVA fibers have a length of 8 mm, diameter of 40 µm and an oil coating of 1.2 percent per fiber weight (commercial product name: RECS15 from manufacturer KURALON™). Chemical and physical composition, and grain size distribution of the limestone powder and CEMIII/B 42.5N LH HSR were provided by the manufacturer (see appendix C).

Table 3.2 Mix designs for sub-question 2.

CEM III/B 42.5 N LH HSR	LP	BFS	w/p	SP	PVA fiber (by volume)
1	1	-	0.26	0.0027	2%

The mixing procedure is shown in

Table 3.3. Directly after mixing two workability tests are performed to ensure a self-compacting mix. These are the V-funnel test and the mini-slump test, described in respectively chapter 3.5.2.1 and 3.5.2.2. After the workability tests the fresh SHCC is scooped by hand into molds of 240*60*10 mm^3 and 400*200*30 mm^3. Then kept in the mold with a plastic foil cover for one day. After one day the specimens were demolded and put into a curing room for 14 days (constant temperature of 20±2 °C and a relative humidity of 96±2 %). One day prior to testing the specimens were sawn into the desired dimensions. For the specimens cast in the 240*60*10 mm^3 mold four evenly pieces of 120*30*10 mm^3 were sawn. These specimens are coded ML (TU Delft **M**icro**L**ab standardized geometry). The specimens cast in molds of 400*200*30 mm^3 will be sawn into pieces of 360*90*30 mm^3 and coded 3ML (ML with a factor 3 in all dimensions). After sawing the specimens are put back into the curing room until the mechanical tests.

Table 3.3 Mixing procedure for mix.

Procedure	Duration [min]
Mix dry powder ingredients	2 min
Add water and SP	1 min
Medium speed mixing	2 min
Add fiber	2 min
High speed mixing	3 min

3.5.2.1 V-FUNNEL TEST

The V-funnel is wetted with water before testing. The lower opening of the funnel will then be closed and the V-funnel is filled with fresh SHCC until the top of the funnel. From the moment the lower opening of the funnel is opened until the moment light passes through the funnel time is measured. This time is called the V-funnel flow time.

3.5.2.2 MINI-SLUMP TEST

The steel cone and flat square steel plate are wetted with water. Then the cone is placed on the plate and filled with the fresh SHCC mixture. Afterwards the cone is lifted up and the mixture flows. When flowing has stopped the spread of the mortar is recorded by measuring the major axis of the spread *d1* and the axis orthogonal to it *d2*. The average of these two parameters are the slump diameter.

3.5.3 MECHANICAL TESTING – 4-PBT

The procedure of the mechanical testing is depicted in Figure 3.7. In order to make a good comparison between the ML and 3ML specimens, the displacement rate of the 4-PBT should be calibrated such that the ML and 3ML specimens will develop a first crack after similar duration of loading. The reason for this is to have a similar introduction of the energy, which leads to comparable creep, relaxation and redistribution of the stresses.

The displacement rate for the ML specimens is 0.02 mm/s and is based on literature research. It is expected that the 3ML specimens will have a higher deflection capacity. Therefor an initial displacement rate of 0.04 mm/s for the 3ML specimens is chosen. After testing one ML and one 3ML specimens, the displacement rate for the remaining 3ML specimens, s_{3ML}, is adjusted according to (eq. 3.1). Where s_{3ML}' is the adjusted strain rate for the 3ML specimens, and $t_{LOP,ML}$ and $t_{LOP,3ML}$ the time at first crack for respectively the ML and 3ML specimens.

$$s_{3ML}' = \frac{t_{LOP,3ML}}{t_{LOP,ML}} * s_{3ML} \qquad \textit{(eq. 3.1)}$$

After calibration of the displacement rate, several specimens will be tested to construct the flexural stress-fictitious strain diagram. Then the nominal strength and the deviations of the ML and 3ML specimens will be calculated. Lastly, to compare cracking behavior it is chosen to load two specimens until a to be specified load. This load depends on the mean and the deviation of previous results and will be chosen based on the lower limit of both the ML and 3ML specimens. If the lower limit of the ML specimens and 3ML specimens are respectively $\sigma_{ML,Lower\ limit}$ and $\sigma_{3ML,Lower\ limit}$, then the specimens will be loaded until a factor smaller than the minimum of α_1 or α_2 in (eq. 3.2) and (eq. 3.3).

$$\sigma_{ML,lower\,limit} = \alpha_1 * \sigma_{ML,average} \quad \textit{(eq. 3.2)}$$

$$\sigma_{3ML,lower\,limit} = \alpha_2 * \sigma_{3ML,average} \quad \textit{(eq. 3.3)}$$

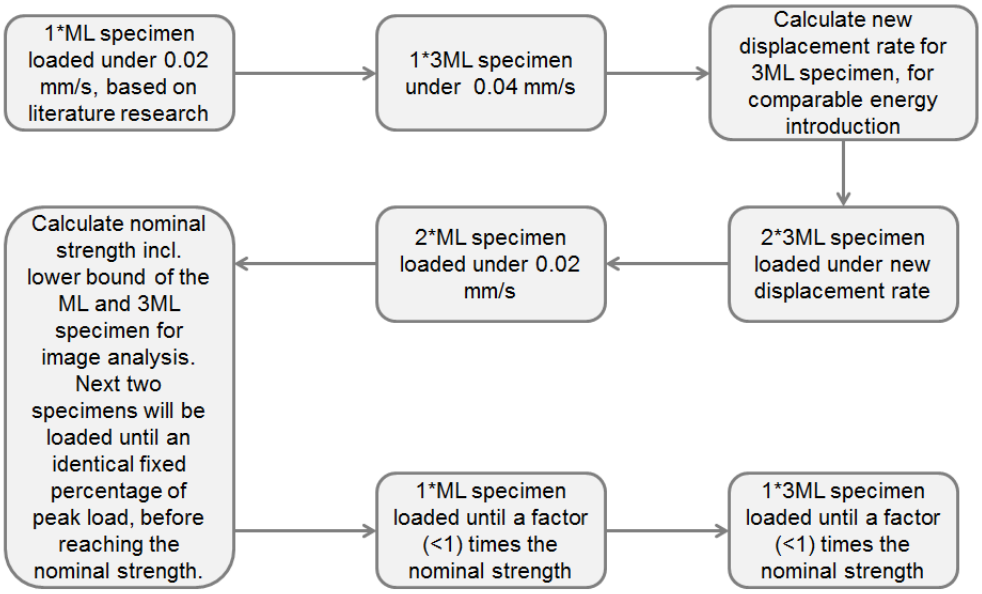

Figure 3.7 Flowchart for the experimental procedure of chapter 3.

3.5.3.1 DETERMINING THE STRESS

In the remainder of the report the tensile stress in the specimen is used to construct the stress-strain diagrams, the calculation of the strain capacity etc. However in the test setups a force *F,* applied by the piston, is being measured.

According linear elastic theory the stress can be calculated as the moment (from *F)* divided by the section modulus, as given in (eq. 3.4). Where *a* is the distance between the outer support and its adjacent inner support*, b* the initial specimen width*,* and *h* the initial specimen height.

However SHCC does not behave linear elastic during the 4-PBT. In reality SHCC is a heterogeneous material that shows multiple cracking. This is of importance since the section modulus changes through the effective height if the specimen is cracked (Figure 3.8). The comparison between the stress levels of differently sized specimens is unjust since the relation of the effective height and section modulus is quadratic. However when assuming that both sized specimens have a crack depth of a the same percentage of their height, which is a reasonable assumption if the specimens are geometrically similar and from the same material, then the comparison of the calculated stresses are fair. It is recommended to check whether the effective heights of the cracked ML and 3ML specimens are indeed the same ratio of the specimen height. This is done in chapter 5.5.3.3.

In the Eurocode the above mentioned situation is coped with formula (3.23) in NEN-EN 1992-1-1. This formula is (eq. 3.5) in this thesis and is a magnification factor for the mean flexural tensile strength $f_{ctm,fl}$

for specimens with a height smaller than 1600 mm is given. Where the $f_{ctm,fl}$ is calculated from the mean axial tensile strength f_{ctm}. The background of this formula can be explained with Figure 3.9. This figure shows the stress diagram in the cross section. From the mean axial tensile strength the black lines can be constructed. In reality, due to cracking of the specimen and the concrete tail softening behavior one gets a line similar to the red line. For the simplification of calculations of engineers, the red line is converted to the green line. Where the moment capacity of the red and green line should be equal. The Eurocode formula is an empirically determined formula, and most probably not suitable for SHCC since SHCC has strain hardening behavior instead of tail softening in concrete.

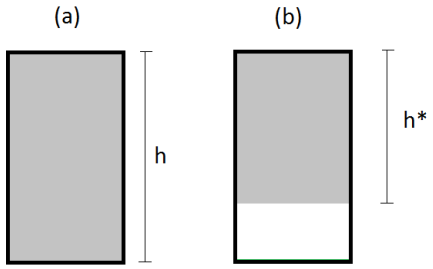

Figure 3.8 Cross section showing effective height h of uncracked (a), and effective height h of cracked (b) specimen.*

$$\sigma = \frac{M}{W} = \frac{0.5F * a}{\frac{1}{6} * b * h^2} \qquad \textit{(eq. 3.4)}$$

$$f_{ctm,fl} = \max\{\left(1.6 - \frac{h}{1000}\right) f_{ctm}; f_{ctm}\} \qquad \textit{(eq. 3.5)}$$

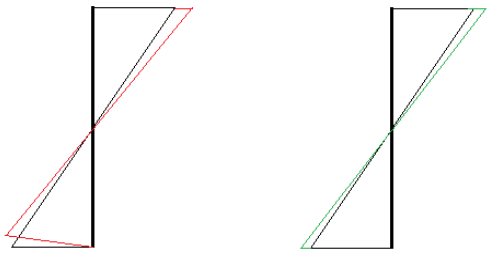

Figure 3.9 Stress diagram of a cross section. Black, red , and green line are respectively: calculated from the mean axial tensile stress, due to crack and tail softening behavior of concrete, and fictitious stress.

Figure 3.9 is for ordinary concrete, where the stress diagram follows an elastic brittle behavior. In Figure 3.10 another model for the stress diagram is depicted. In this model the material shows plastic behavior. The red and blue arrow represent respectively the total compression and tensile forces. These to forces around the neutral axis form a total moment, which is equal to the moment capacity.

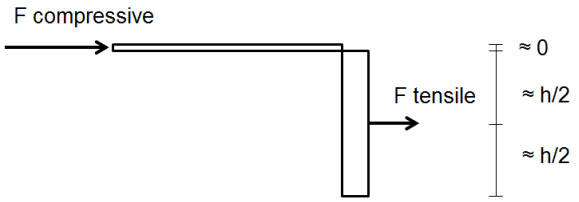

Figure 3.10 Simplified stress diagram of SHCC. Total compression force and tensile force shown as arrows.

In reality SHCC shows a behavior somewhere between that of Figure 3.9 and Figure 3.10. However for the purposes of this thesis it is adequate to follow (eq. 3.4) as long this is done consistently.

The self-weight of the specimens has been mentioned and is included in the stress by (eq. 3.6), where:

- q is a uniform distributed load equal to the density of the SHCC multiplied with the cross section area.
- l is the span equal to the distance between the outer supports.

$$\sigma = \frac{\frac{1}{8} q l^2}{\frac{1}{6} * b * h^2} \qquad \textit{(eq. 3.6)}$$

In the case of the ML specimens, where the piston moves is in opposite direction of the self-weight the self-weight is subtracted from the total stress.
In the tests in chapter 5 a steel block is used between the piston (chapter 5.3.2), which spreads the concentrated piston load into two inner support loads. This weight will be added to the stress as (eq. 3.4). Where $F_{steel\ block}$ is the force from the self-weight of the block.

3.5.3.2 DETERMINING THE STRAIN

The strain capacity between the ML and 3ML specimens are calculated indirectly from the between the vertical displacement and linear elastic theory. Therefor this is a fictitious strain and by no means the engineering strain. The fictitious strain [‰] can be calculated by (eq. 3.7) which gives the strain along the height of the cross section. Where δ_p, l, a, and z are respectively the deflection of the piston, distance between outer supports, distance between the outer support and its adjacent inner support, and the coordinate along the height of the cross section with the origin at the neutral axis. For the derivation of the equation see appendix D.

$$\varepsilon(z) = \frac{6\delta_p z}{(3l^2 - 4a^2)} * 1000 \qquad \textit{(eq. 3.7)}$$

The engineering strain [‰] (eq. 3.8) is defined as the measured elongation of the LVDT (Δl) divided by the original measuring length (L_0).

$$\varepsilon = \frac{\Delta l}{L_0} * 1000 \qquad \textit{(eq. 3.8)}$$

3.5.4 CRACK CHARACTERIZATION

Crack characterization of SHCC is realized with image analysis. Per size one specimen is prepared according to the flowchart in Figure 3.7. The specimens are loaded until a fixed percentage of maximum nominal strength according to the results of previous tests. With image analysis the crack width distribution will be presented.

3.5.4.1 ACQUIRING IMAGES

After loading the specimens to the desired load level, the specimens are impregnated with epoxy with a fluorescent dye. Due to practical reasons it was not possible to epoxy impregnate the whole 3ML sample, therefor the specimen was first sawn to an easy-to-handle size of 90*90*30 cm^3. After epoxy impregnation the top layer of the epoxy is removed by polishing the specimens.
Images were acquired when the specimens were put under UV light with a Canon EOS 20D camera. The empty spaces which are impregnated with epoxy, e.g. the cracks, will fluoresce under the UV light.

3.5.4.2 IMAGE ANALYSIS WITH IMAGEJ

Image analysis of the acquired images are performed with the software imageJ. Contrary to some crack pattern characterization techniques that utilizes lines which intersect the cracks to characterize the crack pattern, in thesis research the crack pattern will be characterized by analyzing the whole image. The advantage of this method is that information of the whole image is used. Where in the former technique only information from the image that intersects the lines are used.

Below a step-by-step guide to acquire the crack width distribution from the base image (Figure 3.11) is given:

1. Selecting the fluorescent parts of the image: *Image>adjust>color threshold. Based on Hue (0-255), saturation (0-255) and brightness (88-255).*
2. Produce a binary image (Figure 3.12): *Process>binary>make binary.*
3. Cleaning the binary image from fibers and some shrinkage (horizontal) cracks by pixel size (Figure 3.13): *Analyze>analyze particles. Pixel size between 1000 and infinity.*
4. Divide the image in grids which show individual cracks as much as possible: *image>stacks>tools>montage to stack. Images per row 10 and images per column 10.*
5. Measure the area per grid (Figure 3.14 left): *analyze>analyze particles. Summarize.*
6. Skeletonize the stacked images (Figure 3.14 right): *process>binary>skeletonize.*
7. Measure the length of the crack. (Skeletonized objects will have one pixel thickness): *analyze>analyze particles. Summarize.*

The area of the skeletonized crack in the grid describes the crack length of the crack within one grid. When the area of the whole crack within the normal grid is divided by this value one can get the average crack width within the grid. The accuracy of the crack width distribution is higher when a smaller grid size is chosen. The average crack width in all grids can be plotted in a weighed distribution which considers the crack length corresponding with the average crack widths. To compare between differently sized objects, one can normalize the area of the analyzed image by presenting the crack width distribution per amount of area. In this example it is chosen for an area of 10 cm^2.

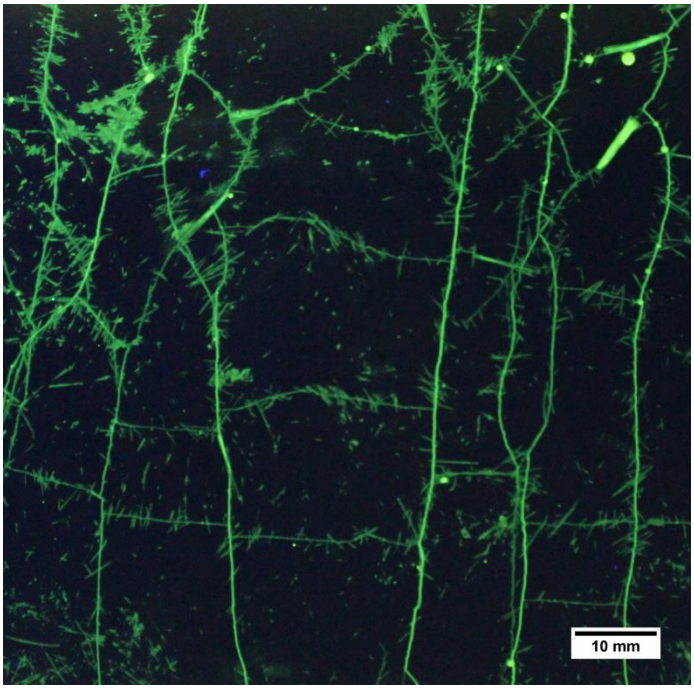

Figure 3.11 Base image for image analysis.

Figure 3.12 Binary image of base image.

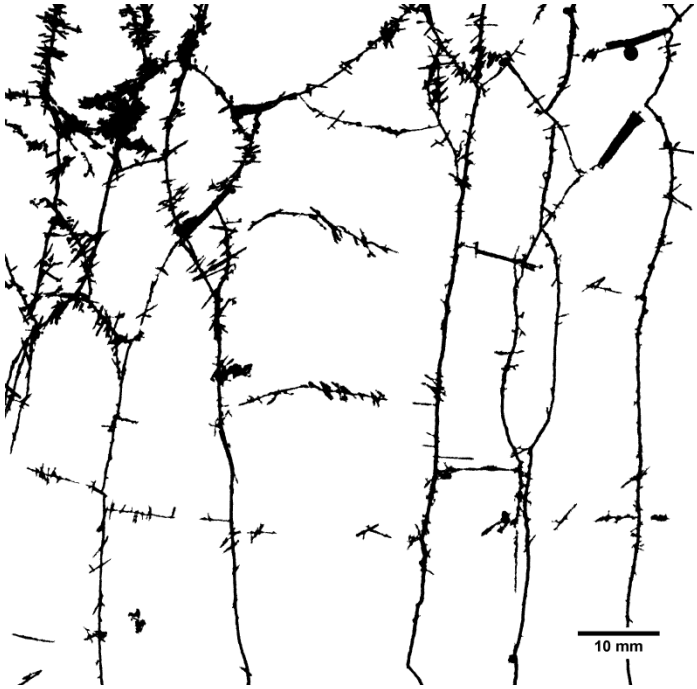

Figure 3.13 Cleaned binary image without fibers and some shrinkage (horizontal) cracks.

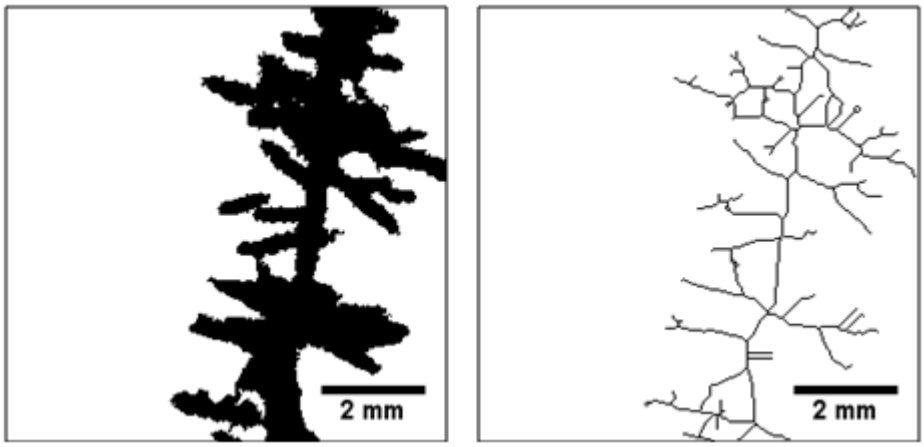

Figure 3.14 Example of image in stack (left) and skeletonized of stack (right).

3.6 RESULTS AND DISCUSSION

3.6.1 WORKABILITY

The slump diameter and flow time of the fresh SHCC are given in Table 3.4. According to NEN-EN206-9 the results of the slump diameter of batch 1 classifies as class SF1 and batch 2 as SF 2. While the V-funnel flow time of batch 1 classifies as VF2 and batch 2 as VF1.

Table 3.4 Slump diameter and flow time of the fresh SHCC.

Batch	Slump diameter [cm]	Flow time [s]
Batch 1	51	9.0
Batch 2	67	7.1

The European Guidelines for Self-Compacting concrete gives an explanation for the consistence classes [7]:

…SF1 (550-650 mm) is appropriate for:
- *Unreinforced or slightly reinforced concrete structures that are cast from the top with free displacement from the delivery standpoint….*

…SF2 (660-750 mm) is suitable for many normal applications (e.g. walls, columns)….

…VF1 has good filling ability even with congested reinforcement. It is capable of self-levelling and generally has the best surface finish. However, it is more likely to suffer from bleeding and segregation….

…VF2 has no upper class limit but with increasing flow time it is more likely to exhibit thixotropic effects, which may be helpful in limiting the formwork pressure … ore improving segregation resistance. Negative effects may be experienced regarding surface finish (blow holes) and sensitivity to stoppages or delays between successive lifts…

Since the specimens are all unreinforced these values for both batches have been accepted.

3.6.2 GENERAL SIZE-EFFECT

This chapter discusses the size-effect found in the ML and 3ML specimens. The nominal strength and the strain capacity will be compared. Figure 3.15 and Figure 3.16 show the stress-fictitious strain diagrams of respectively the ML (120*30*10 mm^3) and 3ML (360*90*30 mm^3) specimens. Due to incorrect calibration the experimental series has been replicated with the same conditions (age, curing time, mixing method etc.) for the ML specimens. While for the 3ML specimens only three specimens from both attempts could be used due to their time at first crack after loading. For more details about the displacement rate and time until first crack after loading of the specimens see chapter 3.6.3.

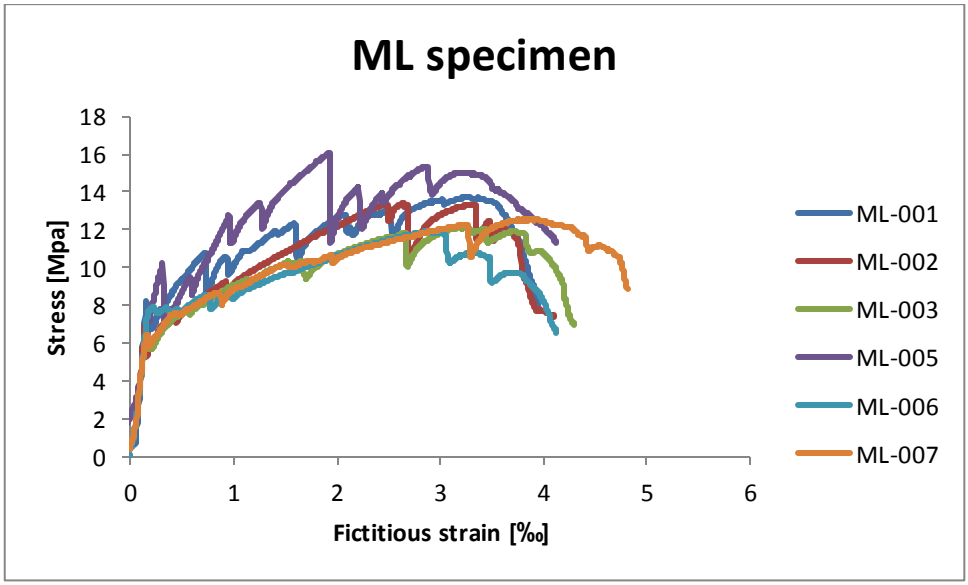

Figure 3.15 Stress-fictitious strain diagram of ML specimen.

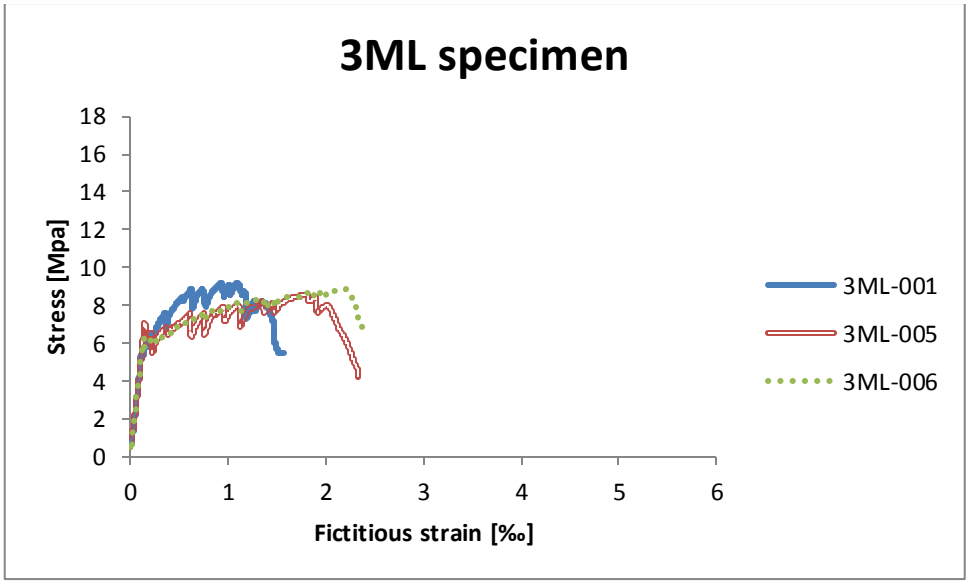

Figure 3.16 Stress-fictitious strain diagram of ML specimen.

As can be seen from Figure 3.15and Figure 3.16 both types of specimens did show strain-hardening behavior. Small drops in strength in the curves indicate the initiation of a new crack. Where after the bridging fibers take over the load and strengthens the crack plane, leading to increase of load capacity. Increased load will initiate another crack elsewhere in the specimens. This process repeats until the specimens are saturated with cracks. After testing photos of the cracked surface of the specimens were taken. All specimens showed multiple fine cracks, which corresponds with the stress-fictitious strain curves. Figure 3.17 shows an example of the multiple fine cracks of the ML (upper) and 3ML (lower) specimens.

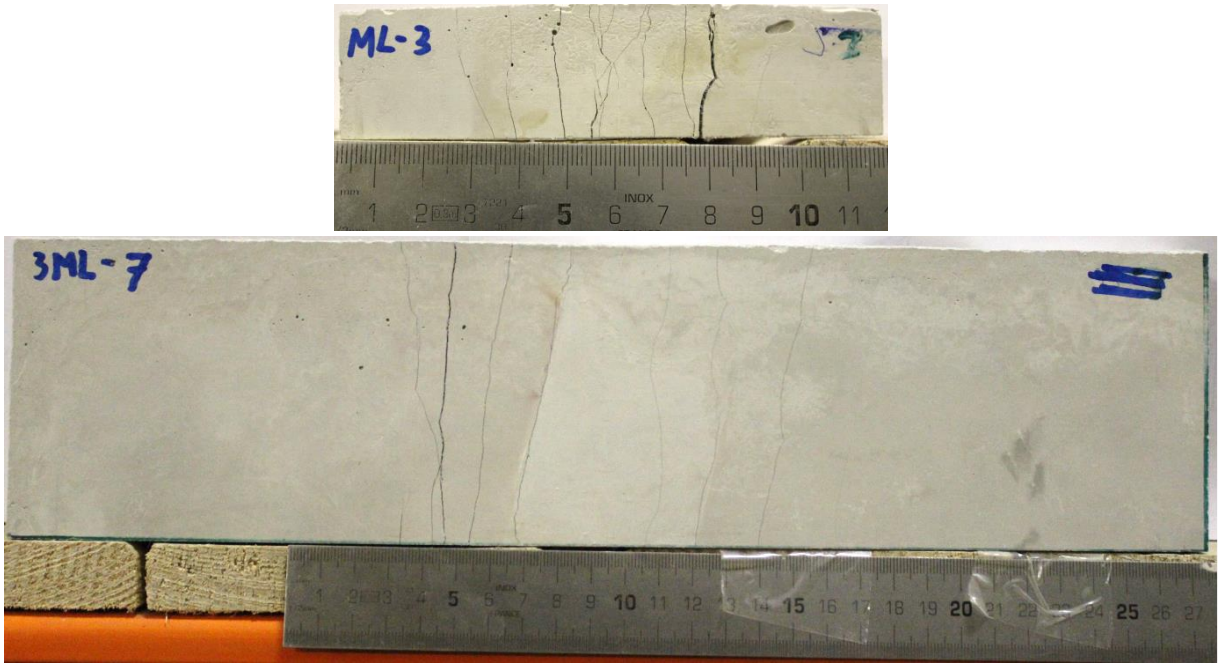

Figure 3.17 Specimens show multiple fine cracking after 4-PBT. ML (upper) and 3ML (lower).

The nominal strength for the ML and 3ML specimens, both at the age of 15 days, are shown in Figure 3.18. With a two tailed hypothesis and a confidence interval of 95 percent, the nominal strength for the ML specimens is 13.3±1.5 MPa and for the 3ML specimens is 8.4±0.4 MPa. On average the nominal strength dropped with 36.8% with the increase of the investigated specimen size. Furthermore the ML and 3ML nominal strength do not overlap each other as can be seen in Figure 3.18. Based on aforementioned confidence interval it can be concluded there is size-effect in the tested specimen sizes.

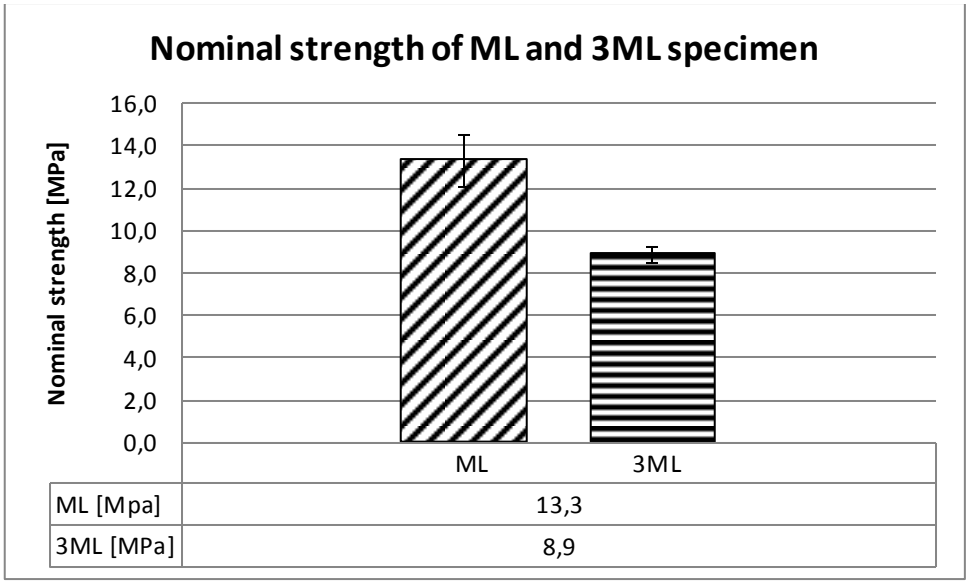

Figure 3.18 Nominal strength of the ML and 3ML specimens with margin of error.

In Figure 3.19 the fictitious strain capacity with a margin of error is given based on a two tailed hypothesis and a confidence interval of 95 percent. The fictitious strain capacity of the ML specimens is 8.9±1.6 ‰, and for the 3ML specimens is 4.9±2.1 ‰. On average the specimen fictitious strain capacity drops 45 percent from the ML to 3ML specimens. However taking into consideration of the margin of errors, this drop could be much less. For more clarification, increased number of samples should be investigated. Similar to the nominal strength one could see that upscaling the specimen sizes has led to a decrease of strain capacity.

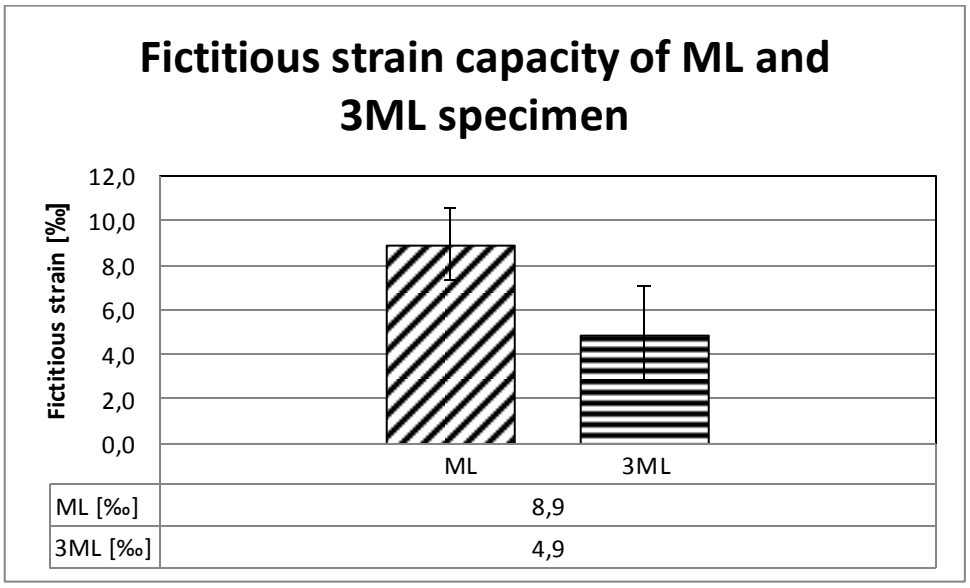

Figure 3.19 Fictitious strain capacity of the ML and 3ML specimens with margin of error.

It should be noted that these fictitious strains are significant lower than the strain capacities found in literature. This is because for the calculation of the fictitious strain linear elastic material was assumed. In such model no cracks development is present. However, in SHCC it is this development of multiple fine cracks and the widening of the cracks that are responsible for the strain capacity. Therefor a comparison between strain capacities only make sense when either the fictitious or true strain capacities are compared consistently with its own type. In chapter 5 the true strain and fictitious strain were both calculated and it was verified that the fictitious strain is a great underestimation of the true strain. In hindsight it would have been better to measure the true strain to compare strain capacity of other literature studies

3.6.3 DISPLACEMENT RATE

As explained in chapter 3.5.3 the rate of loading a specimen has a significant influence on the material properties. Therefor in this experimental series the displacement rates of the 3ML specimens were adjusted in order to let the time of first crack coincide with that of the ML specimens. This leads to a comparable introduction of the energy. Minimizing the influence of creep, relaxation, and redistribution of stresses in the specimens. However a mistake was made during the calibration of the displacement rate. Resulting into a slower loading of the 3ML specimens. The experimental series has been repeated later on with a correct calibration of the load rate of the 3ML specimens. However useful information of the displacement rate on the mechanical behavior of the specimen has been found. These are presented in this chapter.

Table 3.5 shows the displacement rates of two batches made on different dates. Each batch consisted of four ML and four 3ML specimens. Specimens of both batches are tested at the same age. The displacement rate of the ML specimens have all been kept at 0.02 mm/s. While the displacement rate of the 3ML specimens has been varied in the specimen of the first batch.

Table 3.5 Displacement rate of the 4-PBT.

Specimen		**Displacement rate [mm/s]**
Batch 1 mixed on 01-12-2014, tested on 16-12-2014. 3ML displacement rate wrongly calibrated.	ML-001	0.02
	ML-002	0.02
	ML-003	0.02
	ML-004	0.02
	3ML-001	0.04
	3ML-002	0.003, at end 0.15
	3ML-003	0.025
	3ML-004	0.025
Batch 2 mixed on 12-01-2015, tested on 27-01-2015. 3ML displacement rate correctly calibrated	ML-005	0.02
	ML-006	0.02
	ML-007*	0.02
	ML-008	0.02
	3ML-005	0.04
	3ML-006	0.04
	3ML-007	0.04
	3ML-008	0.04

**Apparatus malfunction leading to unloading of specimen halfway. 4-PBT resumed after reset of apparatus.*

In the stress-strain diagram of a strain-hardening material a small drop in the stress corresponds to the formation of a crack in the specimen. The point where the first crack, in the graph the first drop in stress or change in Young's modulus, is known as the limit of proportion (LOP). Table 3.6 shows the time at LOP of the specimen tested in the first batch. As can be seen the time at LOP of the 3ML-002 and 3ML-003 specimens differs from the ML specimens.

Table 3.6 Time at LOP for the specimens of batch 1.

Specimen	**Time at LOP [s]**
ML-001	12
ML-002	12
ML-003	10
3ML-001	13
3ML-002	122
3ML-003	18

Figure 3.20 shows the stress-fictitious strain diagram of the 3ML specimens of batch 1. This figure indicate the effect of the displacement rate on the mechanical behavior of the specimens. However these are merely indications, as the number of specimens per displacement rate is just one.

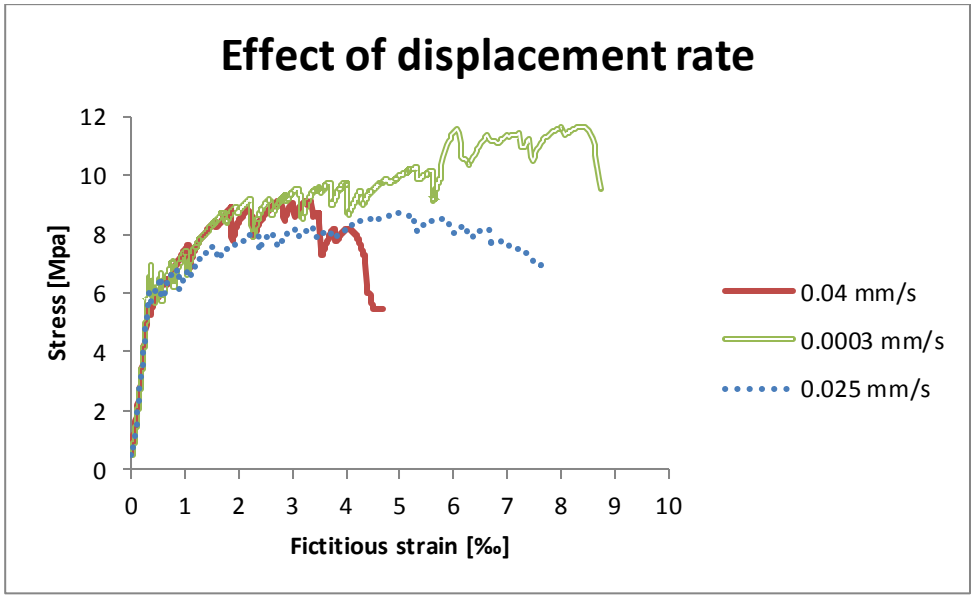

Figure 3.20 Effect of displacement rate on the stress-fictitious strain diagram.

Figure 3.21 and Figure 3.22 show respectively the nominal strength and fictitious strain capacity versus the displacement rate. The labels on the data points show respectively the displacement rate [mm/s], and the nominal strength [MPa] or strain capacity [‰]. It seems that both values tend to drop with increasing loading rate. By comparing these three displacement rates, the biggest drop in the nominal strength relative to the displacement rate of 0.03 mm/s is 22 percent, while for the fictitious strain capacity 67 percent. In the fictitious strain capacity one can see a continuing trend when varying the displacement rate, while this is not the case for the nominal strength.

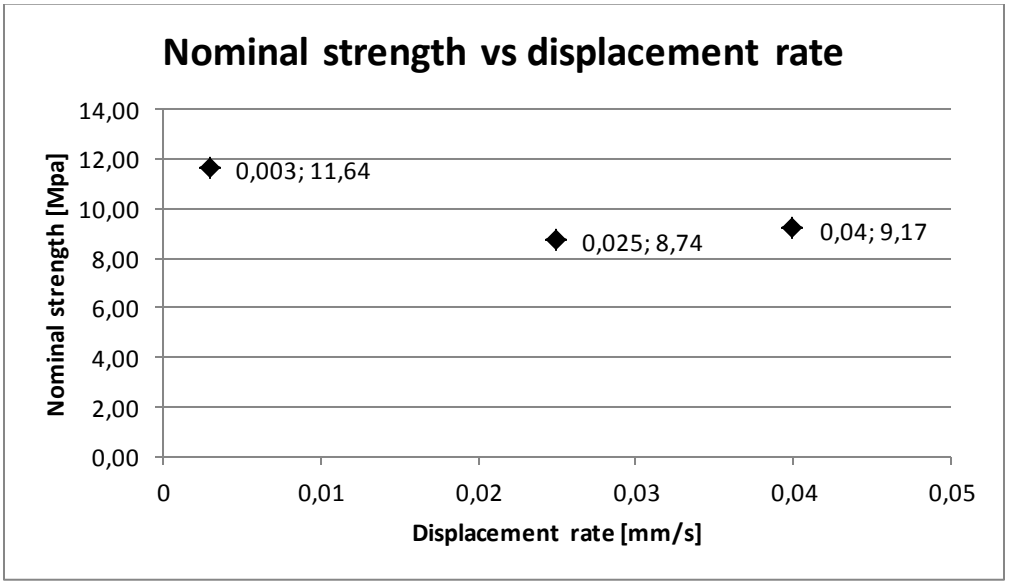

Figure 3.21 Nominal strength vs displacement rate. Label shows respectively the displacement rate [mm/s] and nominal strength [MPa].

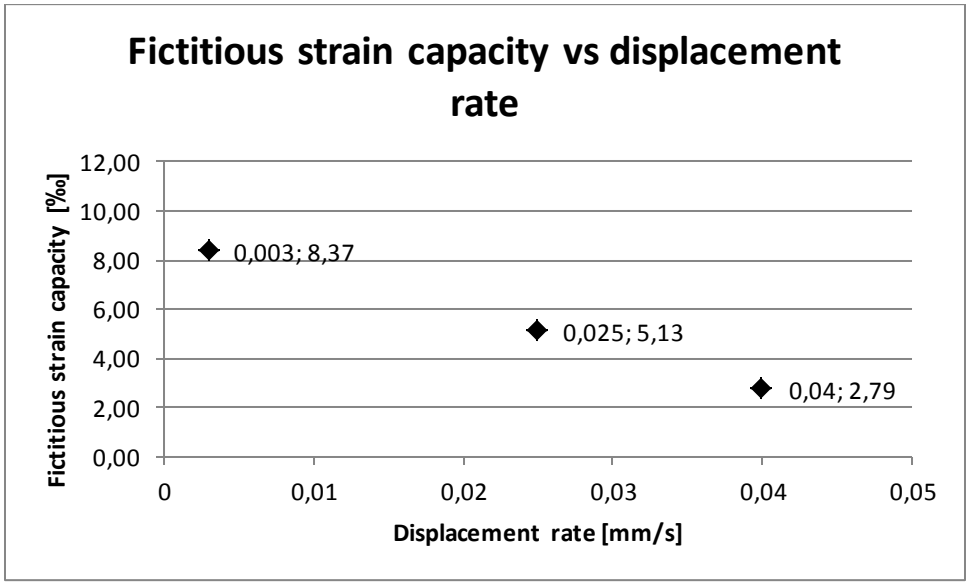

Figure 3.22 Fictitious strain capacity vs displacement rate. Label shows respectively the displacement rate [mm/s] and strain capacity [‰].

The findings can be explained by the different introduction of the energy from the mechanical loading into the specimens. When the displacement rate is reduced, processes such as the redistribution of stresses, relaxation and creep of the material are more pronounced. Redistribution of the stresses allows the peak stresses which are present in the crack tip reduce and is thus beneficial to the nominal strength and (true) strain capacity. Relaxation of the material is also beneficial to the nominal strength and (true) strain capacity. However the creep is unfavorable for the nominal strength as cracks widen and the crack tip will be disturbed. On the contrary this crack widening is favorable for the (true) strain capacity. As the strain capacity is related to the total crack width, this could also explain the stronger drop of the (true) strain capacity in comparison of the nominal strength. While the increased redistribution of stresses and relaxation at lower loading rates both work in favor of the nominal strength and (true) strain capacity, the increased creep is unfavorable for the nominal strength and in favor for the (true) strain capacity. This may be the reason for the discontinuous trend in the nominal strength versus displacement rate.

3.6.4 BATCH EFFECT

Figure 3.23 and Figure 3.24 show the batch effect on respectively the nominal strength and the fictitious strain capacity. The nominal strength of batch one ranges from 12.3 MPa to 13.9 MP, and for batch 2 from 12.1 MPa to 16.2 MPa. Due to this margin of error it can be concluded that the specimens that were prepared for the crack characterization will not reflect the effect of upscaling of specimen size on the crack patterns, and is partly influenced undesirably by the different loading levels. A better way to investigate the crack pattern due to upscaling of specimen size is to load the ML and 3ML specimens to a same chosen amount of strain.

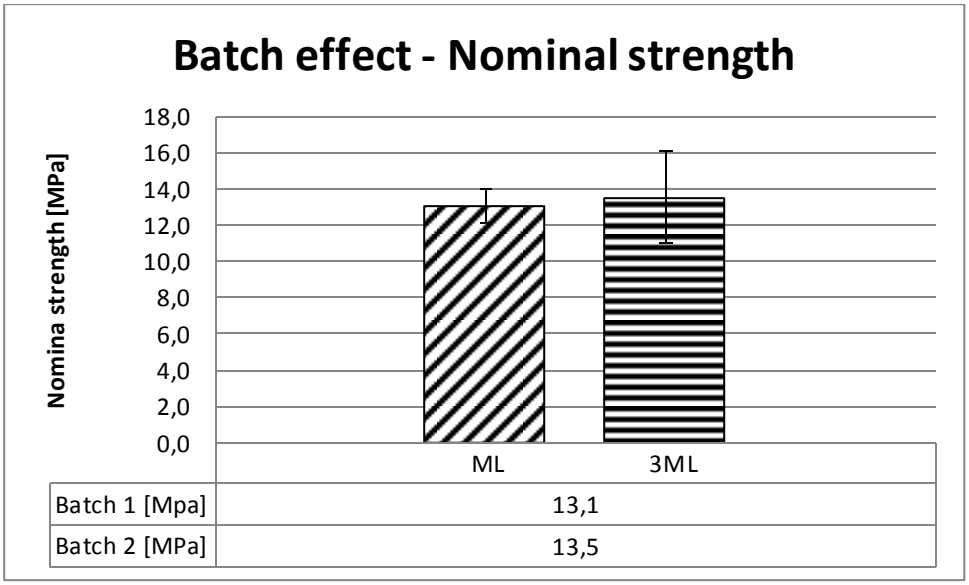

Figure 3.23 Nominal strength of the two batches with margin of error.

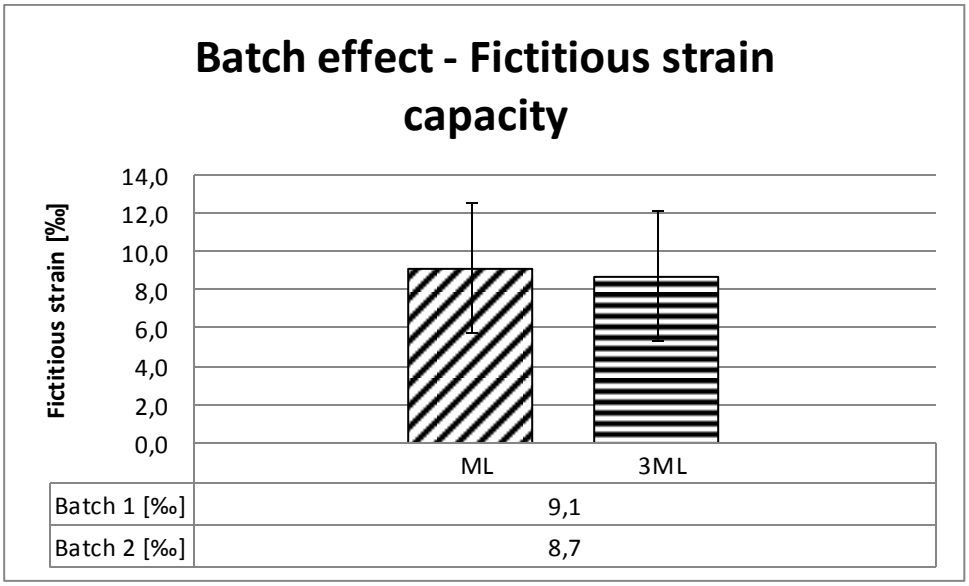

Figure 3.24 Fictitious strain capacity of the two batches with margin of error.

3.6.5 CRACK CHARACTERIZATION

The crack pattern of the ML and 3ML specimens are compared in this chapter. Both specimens were loaded until a fixed percentage of the nominal strength based on limited results. In chapter 3.6.4 it has been found that due to the margin of errors in the nominal strengths of the ML and 3ML specimens this may not be a good comparison. Nonetheless the crack characterization has been performed without correcting the specimen preparation of crack pattern characterization. The point of this chapter is to merely show a possible crack characterization method, rather than giving a conclusive answers to the effect of specimen size upscaling on the crack pattern.

Figure 3.25 shows the crack width distribution of the cracked 3ML specimens per 10 cm^2. It must be noted that the base image consisted of vertical and horizontal cracks. The vertical cracks originate from the mechanical loading as they are perpendicular to the tensile stress. The horizontal cracks are most probably shrinkage cracks. Due to the mechanical cracks the specimen is split into long rectangles with a vertical major axis, simplified in Figure 3.26 left. At the left and right boundary horizontal deformation is allowed along the whole length, but in the middle the vertical deformation is restricted (Figure 3.26 right). This causes vertical stresses which lead to horizontal cracks.
To compare between differently sized objects one can normalize the area of the object to a chosen amount. In this example 10 cm^2 is chosen. As always, it is important to choose an adequate amount of samples. Furthermore the analyzed size of the image should be representative of your sample. For example It is not useful to analyze images of 1 mm^2 if crack spacing in the sample is 20 mm. For a good size of the analyzed images at least multiple cracks should be present in one image.

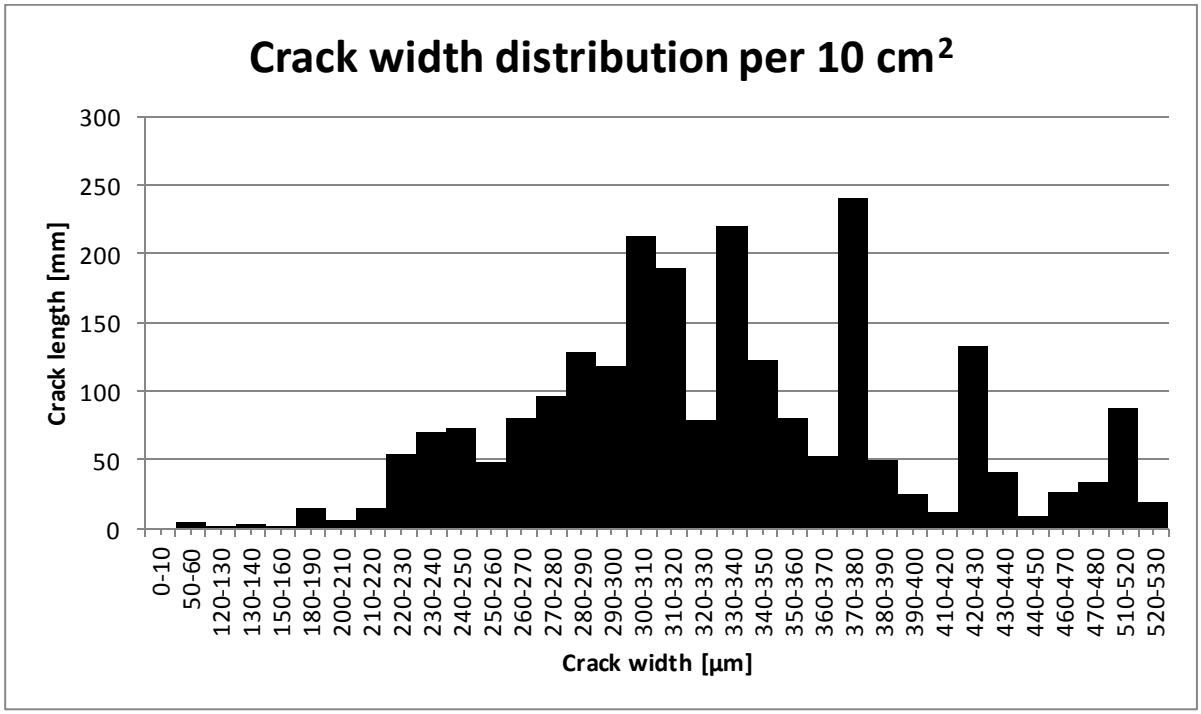

Figure 3.25 Crack width distribution of the cracked 3ML specimen per 10 cm^2.

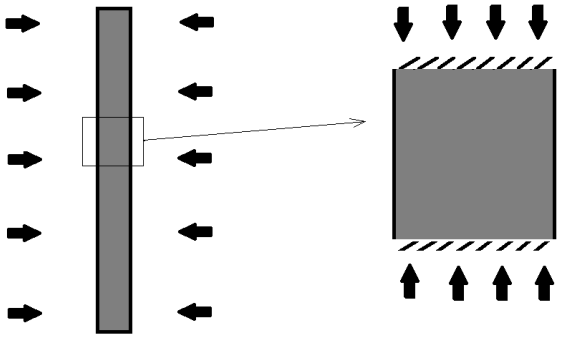

Figure 3.26 Free horizontal deformation due to shrinkage (left). Restricted vertical deformation by shrinkage in middle (right) which causes the horizontal cracks.

3.7 CONCLUSION

3.7.1 CONSLUSIONS

- When the specimens of 120*30*10 mm^3 was upscaled to 360*90*30 mm^3 specimens, the nominal strength and fictitious strain capacity decreased from respectively 13.3±1.5 MPa to 8.4±0.4 MPa and 8.9±1.6 ‰, to 4.9±2.1 ‰. These drops in nominal strength and fictitious strain capacity are both significant and raises concerns since the magnification factor is only 3. The source(s) of this size-effect have yet to be investigated, since this is the general size-effect which contained multiple possible sources.

- The fictitious strain capacity is calculated with the vertical displacement based on a linear elastic model. No cracks were assumed in this model which led to a great underestimation of the true strain. In hindsight it would have been better to measure the elongation to calculate an engineering strain which reflects the deformation of the specimen better.

- It is strongly suspected that the displacement rate has a significant influence on the material behavior. When three specimens of 360*90*30 mm^3 within the same batch were loaded with 0.003 mm/s, 0.025 mm/s, and 0.04 mm/s the nominal strength found in 0.003 mm/s dropped with 22 percent when the displacement rate was increased to 0.025 mm/s, while the fictitious strain capacity dropped 67 percent when the displacement rate was increased to 0.04 mm/s. These observations can be explained by the introduction of the energy into the specimen, where factors such as creep, relaxation, and redistribution of the stresses play a role.

- Crack pattern differences due to size-effect have not been compared due to the variance found in nominal strength between in previous results. However a protocol for the software imageJ to characterize the crack width distribution has been developed for potential future research. This protocol subtracts data from the whole image, opposed to common methods which subtracts data from the gridlines on the image.

3.7.2 RECOMMENDATIONS

- It has been proved that there is a general size-effect between specimens of 120*30*10 mm^3 and 360*90*30 mm^3. The next step is to identify possible sources of size-effect, and quantify and

qualify these per source. In this thesis the fiber effectivity size-effect and fracture mechanics based size-effect will be investigated. Since fibers play a pivotal role in the mechanism developing the multiple fine cracks and fracture mechanics based is a main contributor for size-effect in ordinary concrete. It is recommended that remaining sources will also be investigated since SHCC might behave differently than ordinary concrete.

- The effect of loading (displacement) rate seems to be significant for the nominal strength and strain capacity. More samples have to be tested in order to draw statistical based conclusions.

- A crack pattern characterization for differently sized specimens should be performed to investigate whether upscaling element size will influence the crack pattern. The crack width distribution is an important parameter and can be analyzed with the protocol given in chapter 3.5.4. to do this differently sized specimens should be loaded until a fixed strain and compared with each other.

- The fictitious strain is not reflecting the true strain. A better method which reflects the true strain more is to calculate the engineering strain with the use of LVDT. The fictitious strains is found to be another order than commonly found in literature. Therefor it is recommended that the difference in fictitious strain and engineering strain should be investigated. Furthermore it is recommended that in the future an engineering strain will be measured with the LVDTs or other techniques.

4 FIBER EFFECTIVITY SIZE-EFFECT

4.1 INTRODUCTION

The material performance of SHCC is inherent to the fiber dispersion and orientation. One can design a SHCC mix fulfilling the energy and strength criterion (chapter 2.2.2) and find reduced or no strain-hardening under tension if fiber dispersion and orientation are inadequate.

In the experimental series of chapter 3 it has been proven that significant size-effect has been found in SHCC. One of the possible sources for this is the fiber effectivity size-effect. In this thesis the meaning of fiber effectivity is the effectiveness of a fiber that contributes to the nominal strength and strain-hardening ability of SHCC. Fiber effectivity is evaluated by examining the fibers that are crossing the plane orthogonal to the length of a specimen. Two parameters are used to evaluate this fiber effectivity, these are the amount of fibers crossing the crack plane and their fiber area. Since fiber area can be related to the inclination of the fiber with respect to the tensile stress axis.

In this thesis sections of approximately 40 microns have been used to analyze the fiber effectivity. Thin sections are usually defined as sections with a thickness of 30 micron. However in this thesis sections with a thickness of 40 microns are also called thin sections.

Below a summary of literature study concerning the fiber orientation and dispersion in SHCC is given.

4.2 FIBER ORIENTATION AND DISPERSION

Image analysis provides a powerful tool to examine the fiber orientation in a specimen. In research [8, 9] fiber orientation was examined by analyzing the elliptical shape of the fibers in the cutting plane of a specimen. When using cylindrical fibers, inclined fibers show an ecliptically form in the cutting plane (Figure 4.1). Where d_f is the fiber diameter and l_f the major axis, which is equal to $d_F/cos(\vartheta)$. Thus ϑ, the angle of the fiber with respect to the loading axis can be calculated when d_F and ${}_Fl$ are known. This holds true if the specimen is tested in a UTT. Limitations of this technique are with fibers with relatively lower and higher range of ϑ with respect to the loading axis. In the lower range, the major axis of the fiber l_f change is small and might be bigger than the error introduced by the microscope. For the higher ranges of ϑ, the highly inclined fibers tend to bend due to their low transverse stiffness and therefore detected as less inclined fibers.

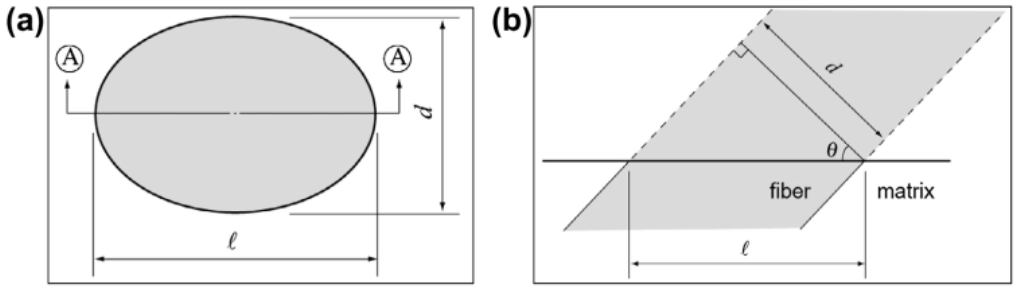

Figure 4.1 Dimensions of inclined fiber (a) and side view of the section A-A [8].

In [24] a similar method computing the ϑ is used, with the ϑ a formula was provided to calculate fiber orientation coefficient (eq. 4.1). Where p(ϑ) is the probability density function of the fiber orientation ϑ. For a 2D and 3D orientation the fiber orientation coefficient is respectively 1/2 and 1/3.

$$\eta_\theta = \int_{\theta_{min}}^{\theta_{max}} p(\theta) cos^2\theta d\theta \qquad \textit{(eq. 4.1)}$$

In research [4] the dispersion in the specimen was analyzed through image analysis. The experimental setup is depicted in Figure 4.2.

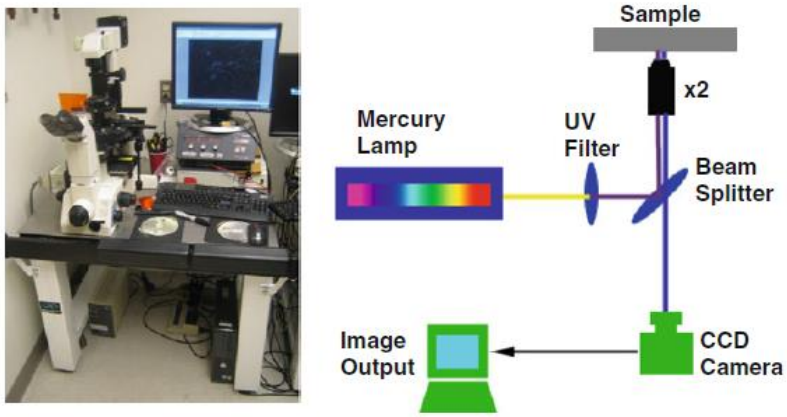

Figure 4.2 Imaging technique and test setup [4].

The use of fluorescence imaging is due to the very high sensitivity to detect treated organic fibers under UV light. In the test setup from [4] a mercury lamp generates a broad range of wavelengths. This is filtered by an UV filter into a specific wavelength and directed to the treated sample. The specimen will fluorescence and emits waves with longer wavelength which is captured by a camera. By stitching multiple images it was possible to construct the whole cross section of the sample. To quantify the fiber dispersion the image of the cross section is divided into a grid consisting of multiple rectangles, called the unit area. Then the coefficient of variation of the fiber count in all unit areas are calculated for the entire image. The coefficient of variation (CV) is defined as the ratio of the standard deviation to the average fibers per unit area, and shows the extent of variability in relation to the mean of the

population, (eq. 4.2). CV is sensitive to the number of unit areas chosen. Then the coefficient of variation is used to calculate the coefficient of fiber dispersion $\alpha_{dispersion}$, see (eq. 4.3).

$$CV = \frac{\sqrt{(\frac{\sum x_i - x_{ave}}{n})}}{x_{ave}} \quad \textit{(eq. 4.2)}$$

$$\alpha_{dispersion} = \exp(-CV(x)) \quad \textit{(eq. 4.3)}$$

4.3 EXPERIMENTAL SET-UP

4.3.1 MECHANICAL TESTING – 4PBT

The experimental setup of the 4-BT is identical to the ML setup in chapter 3.4.1.

4.3.2 WORKABILITY TESTS: MARSH CONE AND V-FUNNEL TEST

The experimental setup of the workability tests is identical to the setup described in chapter 3.4.2 and shown in Figure 3.5.

4.4 EXPERIMENTAL PROCEDURE

4.4.1 INTRODUCTION

This experimental series investigates the effect of the fiber effectivity when the specimen geometry is upscaled. The effectivity is described via the fiber orientation and dispersion. The ML specimens of chapter 3.5.2 will be used the reference. The upscaled specimens are produced by casting the fresh SHCC in a cubical mold with the dimensions 150*150*150 mm^3. From which specimens of 120*30*10 mm^3 will be sawn from. By choosing this specimen size one could make an easy comparison with the ML specimens in chapter 3. To exclude batch variances, the SHCC cube is made from the same batch as batch 2 (see Table 3.5). The nominal strength and strain capacity of the sawn specimens will be compared with the results of the ML specimens from batch 2. Then image analysis will be performed to quantify the fiber dispersion and orientation, which in turn will be related to the nominal strength and strain capacity of the specimens.

4.4.2 SPECIMEN PREPARATION

The ML specimens are prepared as described in chapter 3.5.2. From the same batch of fresh SHCC, a cubical mold of 150*150*150 mm^3 is filled with scoops by hand. Curing of the concrete cube is identical to that of the ML specimens in chapter 3.5.2, with the exception of the sawing procedure which is performed one day prior to testing. This is shown in Figure 4.3. In the first step a layer of 30 mm on all outer surfaces are sawn off to eliminate any Wall effect. The 30 mm is expected to be adequate since PVA fiber length, maximum grain size of the limestone, and cement are respectively 8 mm, 2 mm, and ±200 µm. Then specimens of 120*30*10 mm^3 were sawn out of the cube in three different orientations. These are coded A,B, and C and are orientated as shown in Figure 4.3. For each orientation four specimens will be prepared.

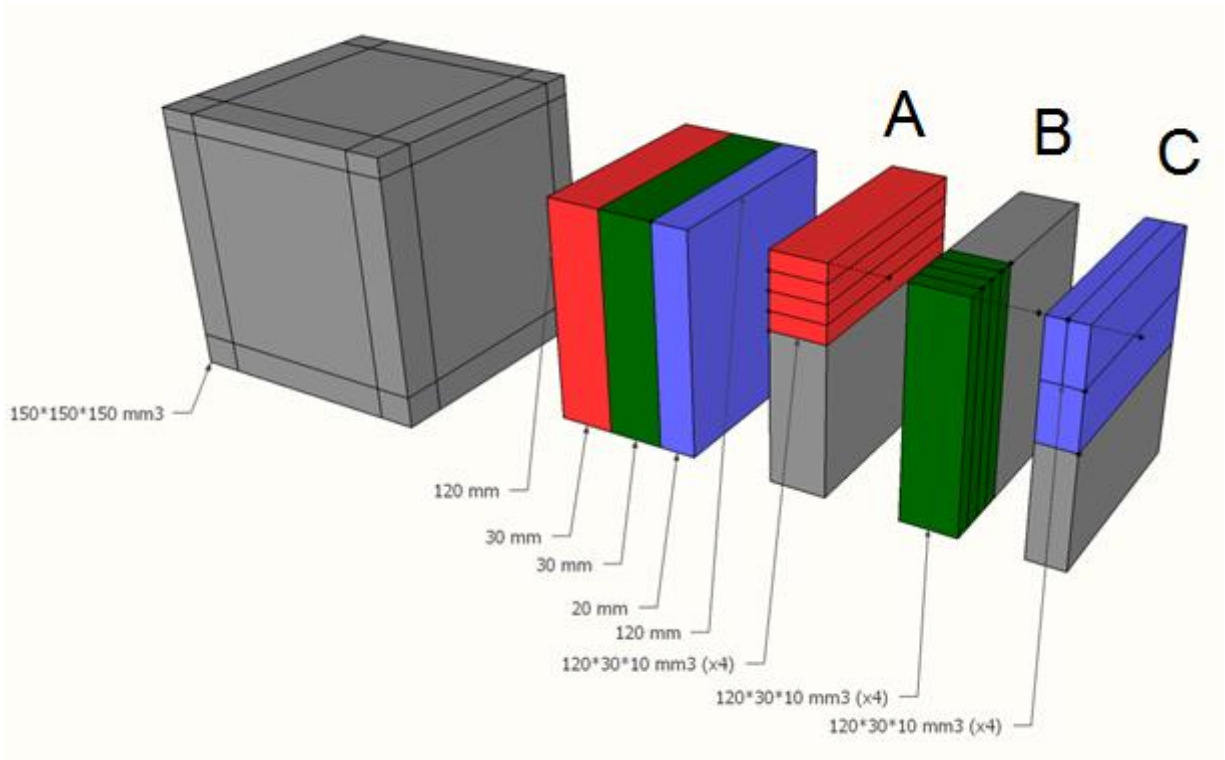

Figure 4.3 Cutting scheme cube. Grey is waste material. Red, green, and blue are specimens with respectively orientation A, B, and C.

4.4.3 MECHANICAL TESTING – 4PBT

All specimens will be tested in 4-PBT as the ML specimen (120*30*10 mm^3) described in chapter 3.5.3.

4.4.4 IMAGE ANALYSIS

To compare the fiber effectivity between the various specimens, the fiber dispersion and orientation will be evaluated by examining multiple 2-dimensional images in the plane orthogonal to the tensile stress axis. Then with the theory of stereology the fiber dispersion and orientation in the three dimensional specimens will be calculated.

In [10] stereology is defined as:

> *"Stereology is a body of mathematical methods relating three-dimensional parameters defining the structure to two-dimensional measurements obtainable on sections of the structure."*

To check the plausibility of the result the Delesse's principle of stereology will be utilized. The Delesse's principle, which is mathematically derived, concerns the relation between the volumetric average fraction with the areal average fraction. If a volume is spatially homogeneous, then the average volume fraction in the volume of a constituent is equal the average fraction of area on a plane section that is

occupied by the same constituent, (eq. 4.4). Where V_{Va} is the volume fraction of constituent A, and A_{Aa} is the area fraction of material a [10].

$$V_{Va} = A_{Aa} \quad \textit{(eq. 4.4)}$$

For the comparison of the fiber orientation it is chosen to not compare the histograms of the inclination of the fibers for each type of specimen, but to present the results by showing the amount of fibers per cm^2 with the corresponding margin of error and the distribution shape of the fiber pixel area. There are various reasons to choose for the latter method of presentation. The main reason is that it makes it possible to quickly compare the variance of the amount of effective fibers per thin section of a specimen. While in a histogram the variance can be shown per fiber inclination, but not per thin section. For the amount of fibers per cm^2 only the fibers between 15 and 100 pixels are considered. The lower limit of the range is based on the theoretical minimum pixel area of a fiber. This is when the fiber circularity is exactly 1 and along the tensile stress axis. The pixel size area corresponding to this pixel area is 18.3. To account for noise introduced by the image resolution a minimum pixel area of 15 pixels is chosen. Reducing the lower limit is irresponsible by including other particles which are not fibers. The upper limit was chosen in order to filter out other particles which are not fibers. This will result into the exclusion of highly inclined fibers.
Eventually for the fiber orientation the amount of fibers per cm^2 with a pixel size between 15 and 100 were compared per type of specimen (A, B, C, or ML). A margin of error of the thin sections within a type of specimen is given. In addition the histogram of the distribution of pixel area is also presented. This is of importance with relation to the fiber inclination. A smaller pixel area of one fiber means a more effective fiber. The histograms are normalized by presenting the fiber count per cm^2

The fiber dispersion in the specimens will be compared by the coefficient of dispersion as given in (eq. 4.3). All images will be divided in 50 unit areas by ten columns and five rows. As the coefficient of dispersion is dependent on the number of unit sizes.

4.4.4.1 THIN SECTION PREPARATION

Thin sections of approximately 40 µm will be prepared. For each orientation (A,B, and C) and the ML specimens one specimen is examined by making multiple thin sections. The cross sections as far away from the constant maximum moment field will be examined. This reduces the probability of disturbed fiber orientation due to the mechanical loading. The sampling positions for the thin sections, seen from the top view of the specimen, are marked by the ovals (Figure 4.4). In this research the specimens A-001, B-001, C-001, and ML-008 were examined.

To distinguish between pores and fibers the specimens will be impregnated with epoxy with fluorescent dye. When the thin sections are put under a compound microscope with a XPL filter, the air pores with fluorescence and the fibers will be clearly visible due to the birefringence.

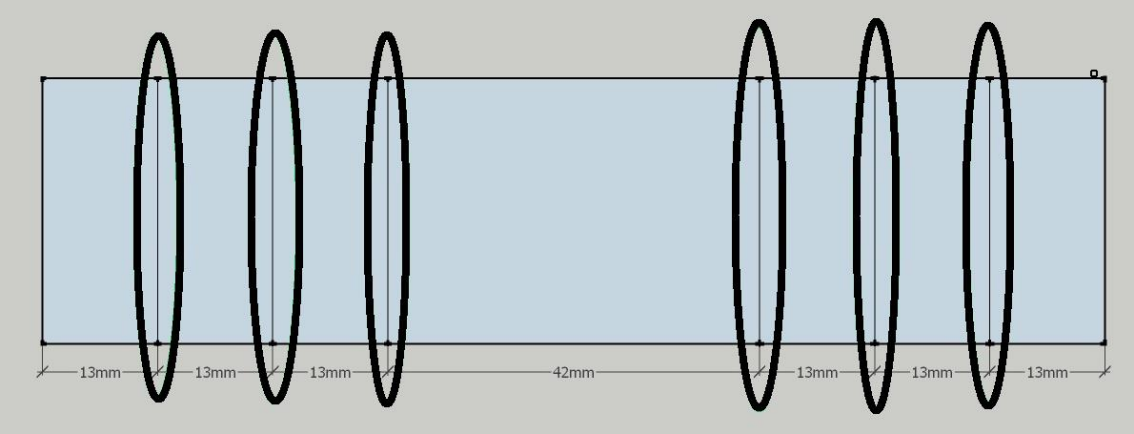

Figure 4.4 Top view of the specimen. Sampling positions of the thin section indicated by the oval marking.

4.4.4.2 IMAGE ANALYSIS PROTOCOL

After images have been taken with the microscope, image analysis will be performed with Fiji, an open source image processing software [11]. Now a step-to-step guide to acquire the image analysis results will be given.

1. Images will be stitched together: *plugins>stitching>grid/collection stitching [12].*
2. Stitched image will be cropped to eliminate pixels not containing the cross section, see Figure 4.5: *image>crop.*
3. Segmentation of the image into two layers: the fibers and non-fiber: *plugins>segmentation> [13].*
4. [If done before, skip to step 5] Train the classifier to use for future cross sections: *if satisfied with the segmentation in two layer save classifier.*
5. Load the classifier: *load classifier from step 4.*
6. Create the mask: *create result.*
7. Check result: *toggle overlay.*
8. Make image RGB color: *image>type>RGB color*
9. Filter the fibers based on color: *image>adjust>color threshold. RGB input R: 0-128, G: 0-255, and B:0-255.*
10. Filter particles based on size and circularity: *analyze>analyze particles> size: 15-100, circularity 0 -1.00. Show masks.*
11. Split clumps of fiber, Figure 4.6: *process>binary>watershed.*
12. Get number of fibers and major axis length, see Figure 4.7: *analyze>analyze particles>15-100, circularity 0 -1.00. Show mask. Check display results (change results by: analyze>set measurements).*
13. Divide the stitched image in unit areas: *image>stacks>tools>montage to stack. Images per row: 10, images per column: 5, border width: 0.*
14. Get number of fibers per unit area: *analyze>analyze particles>15-100, circularity 0 -1.00. Show mask. Check summarize.*
15. Repeat with all other cross sections.

Figure 4.5 Example of a stitched image of thin section under XPL filter.

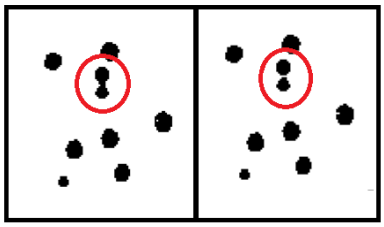

Figure 4.6 Effect of watershed: left is before and right is after.

Figure 4.7 Example of the mask of the filtered fibers in step 12.

4.5 RESULTS AND DISCUSSION

4.5.1 WORKABILITY

The slump diameter and flow are shown as batch 2 in Table 3.4. According to NEN-EN206-9 the slump diameter classifies as SF 2 and the viscosity class to VF1. These are both satisfying the self-compacting ability of the mix. For more information about the classes see chapter 3.6.1.

4.5.2 MECHANICAL PERFORMANCE

In Figure 4.8 to Figure 4.14 the stress-fictitious strain diagrams are shown for all tested specimens. For each type of specimen one photo of the crack pattern after testing is shown below the corresponding stress-fictitious strain diagram. For a complete overview of the crack pattern of all specimens see appendix E.

During mechanical testing of the specimen the testing apparatus malfunctioned and reset itself. For specimen C-004 the reset was after the descending branch, therefor it is included in the results. However for the specimens A-004 and B-002 the testing apparatus was reset halfway the experiment and are excluded from the results.

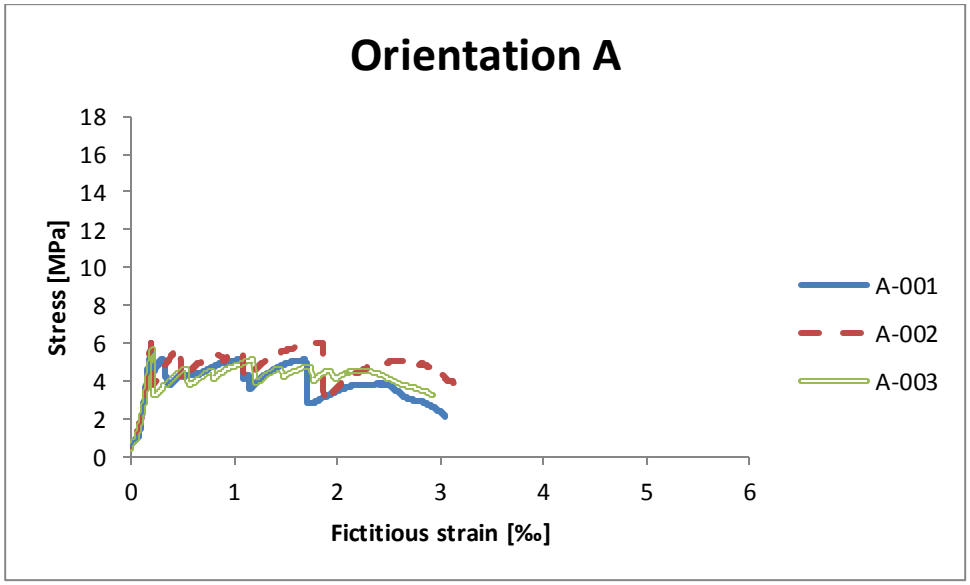

Figure 4.8 Stress-fictitious strain diagram of specimens cut in orientation A.

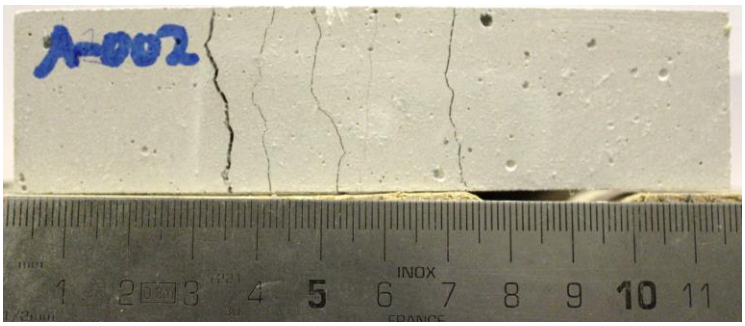

Figure 4.9 Crack pattern of specimen A-002 after loading.

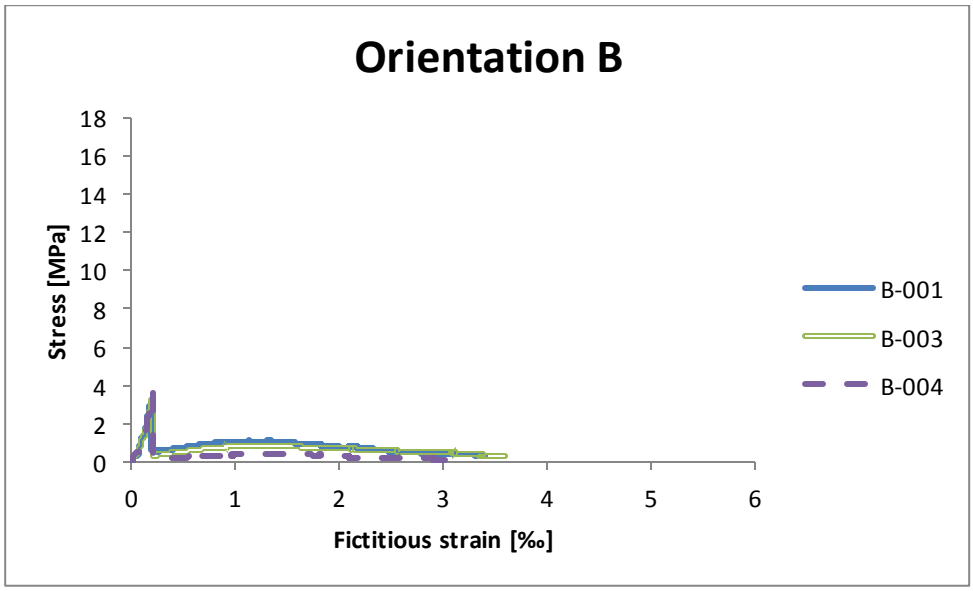

Figure 4.10 Stress-fictitious strain diagram of specimens cut in orientation B.

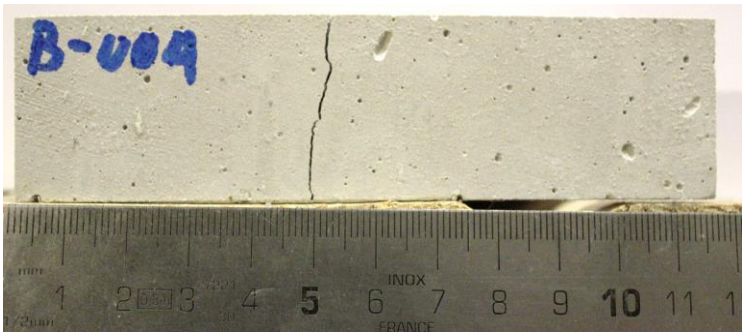

Figure 4.11 Crack pattern of specimen B-004 after loading.

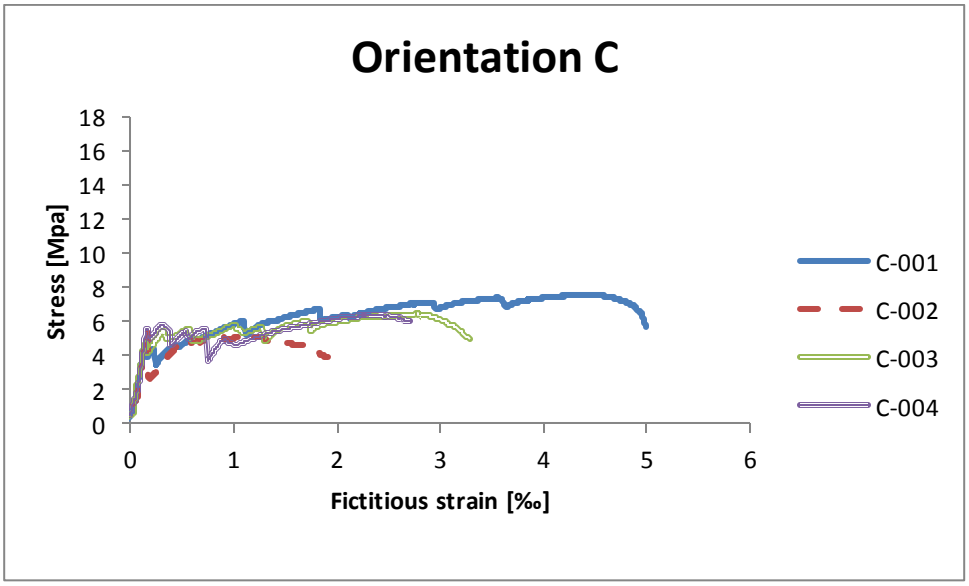

Figure 4.12 diagram of specimens cut in orientation C.

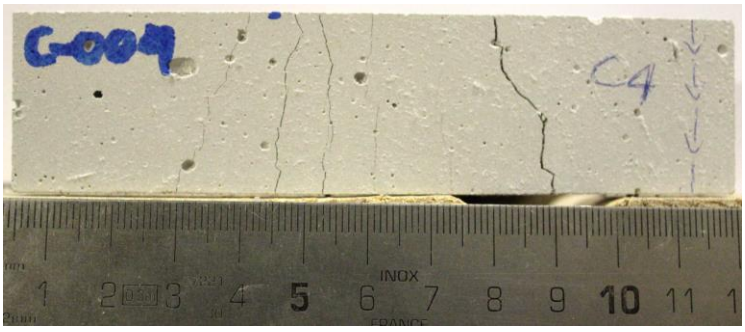

Figure 4.13 Crack pattern of specimen C-004 after loading.

Figure 4.14 Crack pattern of specimen C-002 after loading.

Specimens ML showed a higher nominal strength and strain capacity than the sawn specimens (A, B, and C). One of the reasons is that sawing introduced residual stresses in the A, B, and C specimens. This reduced the nominal strength of the specimens. Aside from the B-specimens and C-002 specimen, all specimens showed strain hardening ability. The B-specimens and C-002 specimen showed a quasi-brittle failure. The nominal strength and strain capacity are shown in Table 4.1. No averages with margin of error for the sawn specimen have been calculated since some of the specimen showed different failure behavior.

Table 4.1 Overview of the results from the 4-PBT.

	Nominal strength [MPa]			**Strain capacity [‰]**		
	Min	Average	Max	Min	Average	Max
A-specimens	5.6	6.0	6.7	0.6	3.7	9.9
B-specimens	3.3	3.7	4.0	0.5	0.6	0.6
C-specimens	5.8	6.8	7.9	0.5	7.3	3.0
	Nominal strength [MPa]			**Strain capacity [‰]**		
ML batch 2	13.68±2.55			8.72 ±3.39		

One might explain the differences in nominal strength and strain capacity by relating it to the fiber effectivity parameters. However as stated before, the relatively low nominal strength of the sawn specimens compared with the ML specimens is partly due to sawing in the specimen preparation.
Figure 4.15 shows the average number of fibers per cm^2 in the specimens. The margin of error represent the variance of the number per fibers per cm^2 between the examined thin sections within each specimen. Figure 4.16 shows the coefficient dispersion of the specimen. The margin of error again represents the variance between the examined thin sections within each specimen type.
A trend can be seen in these results. The nominal strength and strain capacity seems to be in decreasing in the order of ML-, C-, A-, and B-specimens. Coincidentally the minimum value of the fiber effectivity parameters decrease in the same order. The average value of the parameters seem not to be important. This is evidenced by the data from Figure 4.15, where specimens B does have a higher average number of fibers per cm^2 than specimens A, but shows a brittle failure with much less mechanical properties. Figure 4.16 follows the same trend.

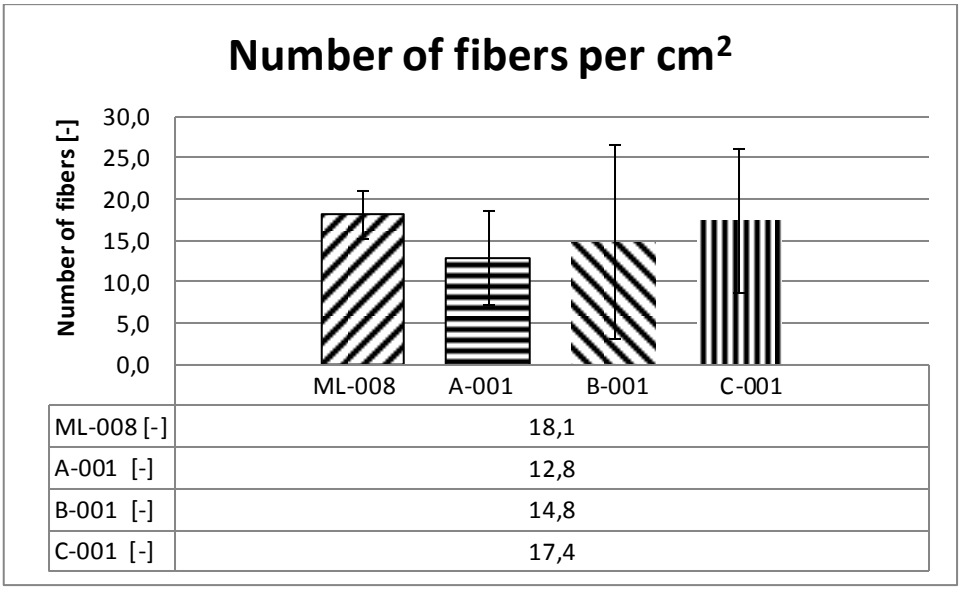

ML-008 [-]	18,1
A-001 [-]	12,8
B-001 [-]	14,8
C-001 [-]	17,4

Figure 4.15 Average number of fibers per cm² with the margin of error between the thin sections.

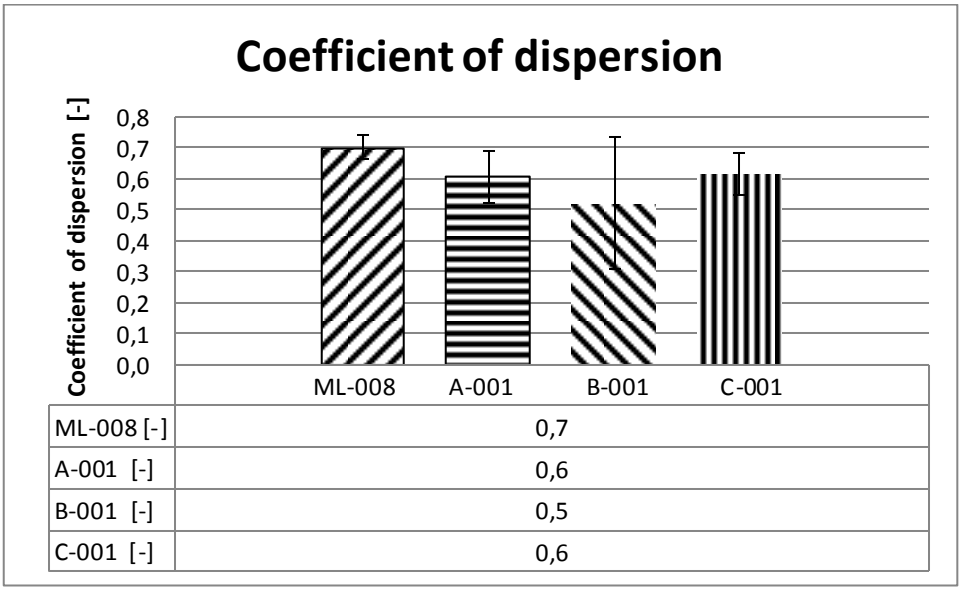

ML-008 [-]	0,7
A-001 [-]	0,6
B-001 [-]	0,5
C-001 [-]	0,6

Figure 4.16 Average coefficient of dispersion with the margin of error between the thin sections.

An explanation can be found in the mechanism of the strain-hardening behavior. In SHCC a crack starts to initiate in the weakest cross section, which is determined by the matrix properties. Two scenarios can occur. The first is that the amount of effective fibers crossing the crack plane are too low to have sufficient bridging capacity to bridge the crack. This will lead to rupture or immediate pullout of the fibers and an immediate brittle failure of the specimen. The second is that there are sufficient effective fibers to bridge the crack. Then the next crack starts to initiate at another location of the specimen and the process repeats. For the latter scenario there is an saturation point where the specimen cannot develop fine cracks anymore. In this case the specimen will also fail by either rupture or pullout of the fibers.

A common concern of conventional fiber concrete where fibers are the primary reinforcement is that the dispersion in the specimen is not good. Which could result into a cross sections with relatively low amount of fibers. This is the weak point of the specimen where the specimen will eventually fail with a (quasi-) brittle failure. For SHCC the crack might not immediately initiate at the cross section with inadequate fibers (see also chapter 4.5.3). However, the more weaker cross sections there are, the higher the chance there is crack initiation at a weak cross section. Which will terminate the development of multiple fine cracks at an early stage. This might explain the differences between the ML-, A-, and C- specimens.
The brittle failure of B-specimens can be explained by the placement of the SHCC in the cube with scoops by hand. Since the fresh SHCC was self-compacting, this led to horizontal layers of SHCC in the SHCC cube. Between these layers there is an interface with weaker properties and probably little fibers crossing the ITZ plane. In specimens B these interfaces are always crossing the whole plane perpendicular of the major axis of the specimen. While for specimens A and C this is not the case. This is depicted in Figure 4.17, where the interfaces are depicted as red planes.
It can be seen that in specimens B the interfaces are dividing the specimen along the major axis of the specimen. The tensile stresses must always cross these planes. In this figure the planes are drawn as perfectly horizontal planes, but in reality this is not the case. However if one plots the locations of the interface on a cross section in specimens B, the whole cross section will always be covered. For the A and C specimens this only can happen if the plane is heavily skewed, which makes the chance of a whole interfaces crossing the tensile stress axis very small, but possible. This might explain the quasi-brittle failure in specimen C-002.

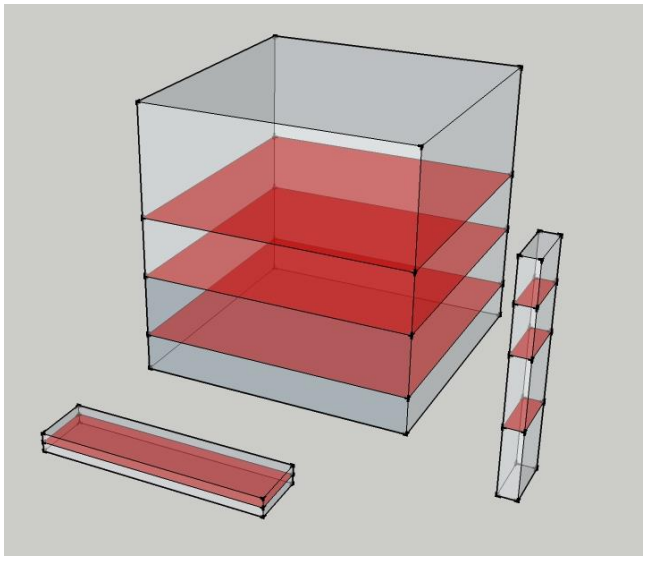

Figure 4.17 Cube with interface between layers due to casting by scoop. Vertical specimens (B) have interfaces dividing the specimens in multiple parts along the tensile axis. Not the case in horizontal specimens (A and C).

Figure 4.18 to Figure 4.21 show the fiber pixel area distribution in every type of specimen. The fiber pixel area distribution can be interpreted as a distribution of the fiber effectivity. The lower the fiber pixel area, the smaller the inclination of the fiber with respect to the tensile stress axis is. It can be seen that all specimens are distributions with one mode, with a peak between 16 and 30 pixels. The distribution of the A, B and C specimens are quite similar. This means that in the cube the fiber arrangement is more or less randomly 3-dimensional orientated. Compared to the ML specimens the area of the columns in the

histogram is smaller, this means there are less fibers crossing the crack plane in the A, B, and C specimens. This is probably due to the fiber Wall effect which is present in the ML specimens, which aligns the fibers along the mold surface.

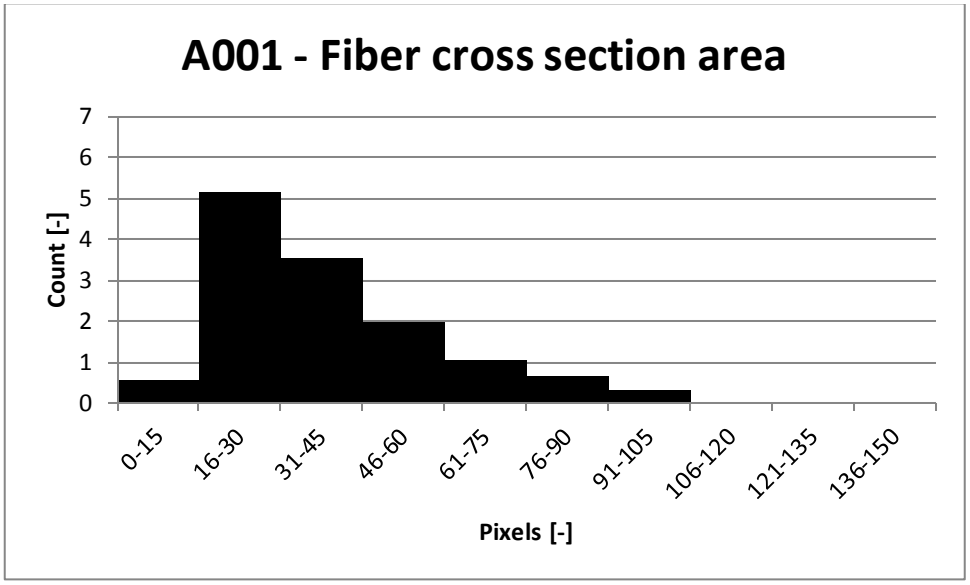

Figure 4.18 Distribution of separate fiber pixel area for specimen A-001.

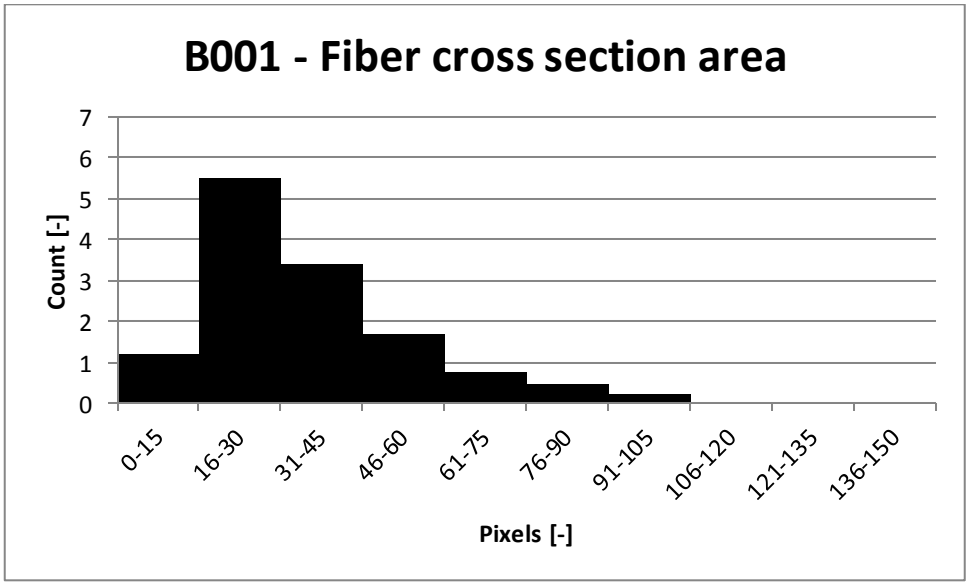

Figure 4.19 Distribution of separate fiber pixel area for specimen B-001.

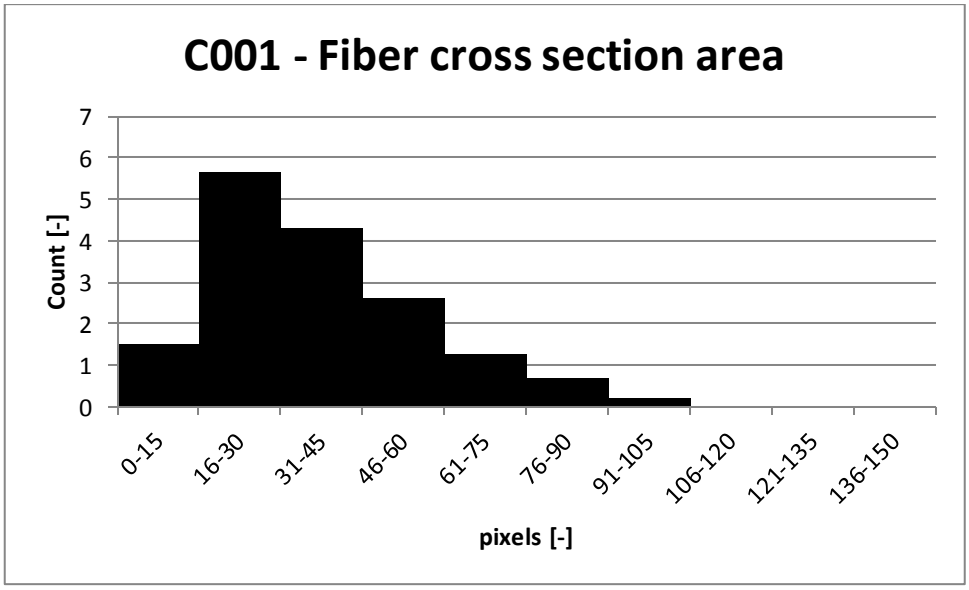

Figure 4.20 Distribution of separate fiber pixel area for specimen C-001.

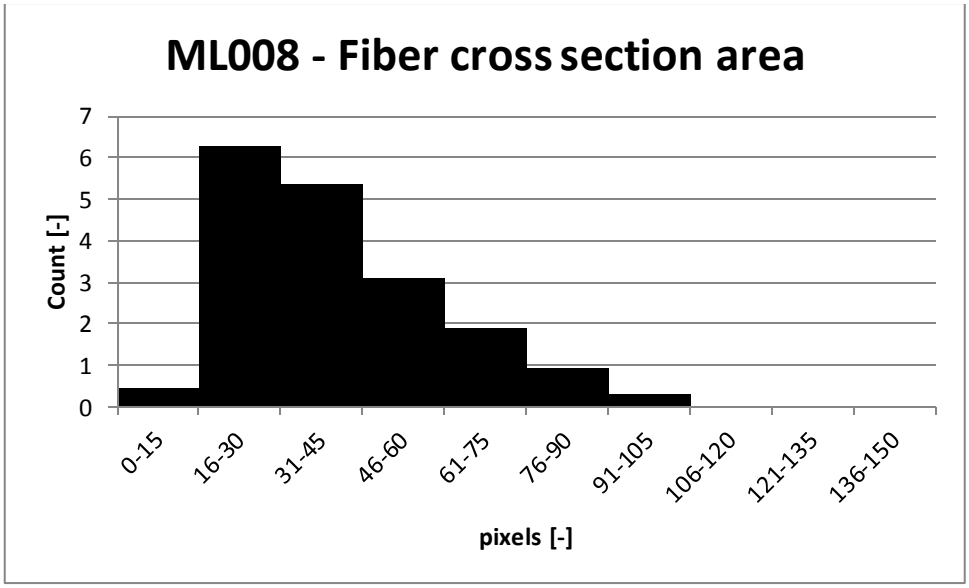

Figure 4.21 Distribution of separate fiber pixel area for specimen ML-008.

The area density of the fiber to the total area is to control the plausibility of the results. The fiber volume fraction in the mix is 2 percent. However not enough samples (thin sections) were examined for a good representation of the whole total specimen. Furthermore the fibers are not spatially homogeneous, because for example the fiber Wall effect in the ML specimens will cause to a higher area density of the fibers. This is also visible in the results, as the ML specimens has the highest fiber area density.

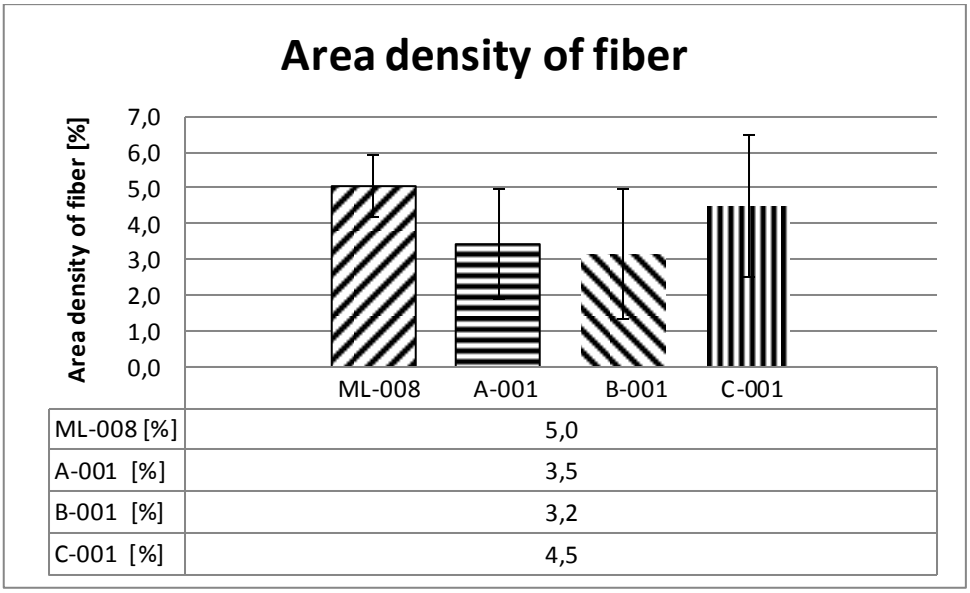

ML-008 [%]	5,0
A-001 [%]	3,5
B-001 [%]	3,2
C-001 [%]	4,5

Figure 4.22 Average area density of fiber with the margin of error between the thin sections.

4.5.3 FIBER-CEMENT MATRIX ITZ

When analyzing the thin sections under UV light with the microscope, it has been confirmed that an ITZ exists between the fibers and the surrounding matrix. Figure 4.23 shows such image, where the fibers are the dark blue round shapes. In the image there is a clear distinction of the brightness of the cement matrix. Around the fibers more bright spots of cement matrix can be observed. This indicates that more UV passed through these parts, from which can be concluded that the porosity is higher in this area. This can be explained by less hydration of cement in these areas due to presence of less hydration water. Which in turn can be caused by the oil-coating of the fibers which is hydrophobic and repel the water. The oil coating was originally applied to diminish the chemical bond between fiber and cement matrix. However a side-effect seems to be that cracks are more likely to initiate and grow at locations where more fibers are. Reducing the probability of crack initiation at an area with fewer fibers.

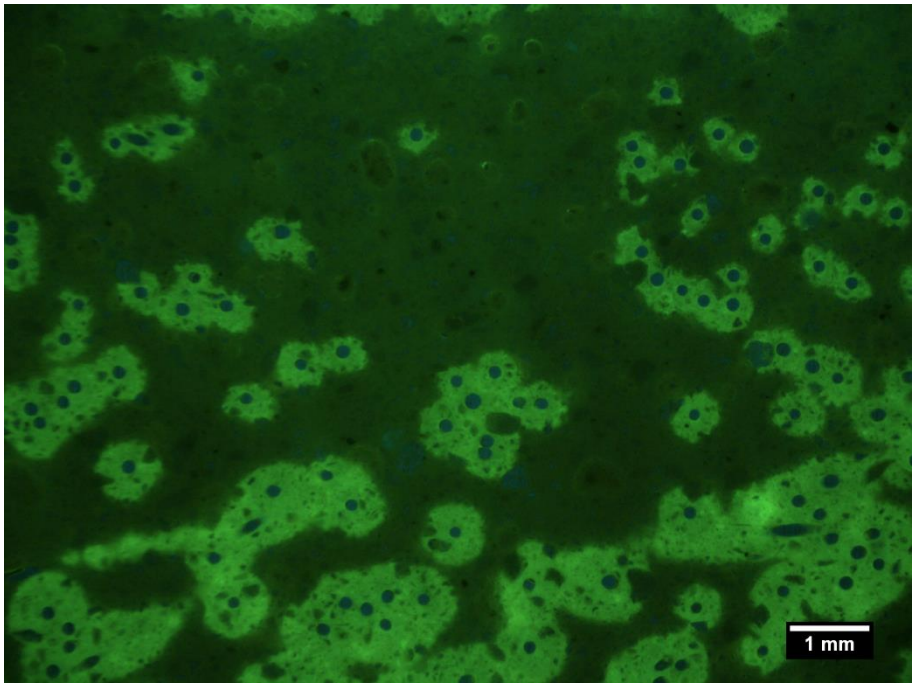

Figure 4.23 Thin section under UV light. Bright green spots indicate relatively higher porosity.

4.6 CONCLUSION AND RECOMMENDATIONS

4.6.1 CONCLUSIONS

- By casting SHCC in a cube of 150*150*150 mm^3 and then sawing out specimens of 120*30*10 mm^3 at different orientations, the effect of fiber effectivity on the nominal strength and strain capacity of thin casted specimen and a thick element (SHCC cube) will be compared in a 4-PBT. With this procedure it has been tried to alter the fiber effectivity of the ML specimens. The fiber effectivity was quantified by the parameters: number of fibers per cm^2 and the coefficient of dispersion, which describe respectively the fiber orientation and dispersion. These have been used to explain the differences in the nominal strength and fictitious strain capacity.

- With analysis of sections with a thickness of 40 microns it has been verified that 3D fiber orientation and dispersion has been achieved for the specimen sawn out of the SHCC cube. The fiber effectivity parameters between these three specimens are more or less the same.

- The nominal strength and strain capacity decreased in the order of the ML-, C-, A-, and B-specimens. Coincidentally this exact order was also found for the minimum of the fiber effectivity parameters. It seems that the average amount is less important, as for the B-specimens all higher numbers of fibers per cm^2 was found than in the A-specimens, but worse mechanical properties were calculated.

- It is speculated that the more weaker cross sections there are, the higher the chance there is for crack initiation at a weak cross section. Which will terminate the development of multiple fine cracks at an early stage. This seems to explain the differences between the ML-, A-, and C-specimens.

- In specimens B quasi-brittle failure is most probably caused by the placement procedure. The SHCC cube was filled by hand with scoop. Due to the small volume of SHCC added per scoop and the self-compacting ability of the fresh mixture, horizontal layers exist in the plane with weaker interfaces for the matrix properties and perhaps little to no fibers crossing the interface plane. This combination leads to crack initiation at a plane where fiber effectivity is simultaneously low. Additionally for specimens B it is expected that each single plane covers the whole cross section if plotted over the cross section. This might explain the quasi-brittle failure found consistently in the B-specimens and specimen C002.

- The credibility of the image analysis method on the sections of 40 microns have been checked with the fiber area density in a section. In the mix design a volume percentage of 2 percentage fibers has been used. However higher amounts of fiber area density have been found. This is probably due to the inadequate amount of sections examined. Furthermore the fibers are not spatially homogeneous, because for example the fiber Wall effect in the ML specimens will cause to a higher area density of the fibers.

- Aside from reducing the chemical bond between the fibers and the cement matrix, the oil coating of the PVA fibers seem to be repelling water in the vicinity of the fibers. Creating a ITZ with higher porosity. This zone might lead to easier crack initiation in areas where fibers are present.

4.6.2 RECOMMENDATIONS

- When designing with SHCC it is recommended to acquire relevant parameters in experiments with specimens that have comparable specimen height as the design of the structure. For thicker SHCC elements this lead to a different arrangement of fiber orientation than in common specimen dimensions in literature study. Common specimen dimensions will lead to an unsafe overestimation of the nominal strength and strain capacity.

- The calculation of the stresses can be improved by measuring the true cross section area, because sawing cuts have a thickness. Furthermore it is recommended to investigate the effect of sawing on the nominal strength and strain capacity.

- A placing method to eliminate the weak interfaces which are responsible for the brittle failure in specimens tested in the orientation B should be developed. It is expected that a continuous placing of the composite, in combination with a mixture with low yield stress and high viscosity may lead to elimination of these weak interfaces and prevent brittle failures.
  The effect of including primary steel bar reinforcement in specimens B should also be investigated. The steel bar reinforcement might avoid the brittle failure, while the fibers are primarily responsible for to the development of multiple fine cracks.

5 FRACTURE MECHANICS BASED SIZE-EFFECT

5.1 INTRODUCTION

Fracture mechanics based size-effect is based on the Linear elastic fracture mechanics (LEFM) theory (see chapter 2.5) and is one of the main contributors to size-effect in concrete. This source of size-effect in concrete is significant for larger structures.

This chapter starts with the findings of a literature study on the fracture mechanics based size-effect in SHCC [14] in chapter 5.2. In this particular research no fracture mechanics based size-effect has been found for SHCC. However it should be noted that size-effect concerns strictly the nominal strength. As for SHCC the nominal strength is not what it distinguishes the composite from other cement-based materials. One of the key characteristics of SHCC is the high strain capacity compared to concrete, which translates to a better durability when used correct. Therefor in this experimental series a 4-PBT test will be performed instead of the 3-PBT performed in [14]. By choosing a 4-PBT it is also possible to investigate the strain capacity along with the nominal strength when the geometry of the element is upscaled. Furthermore the results of this experimental series can be used to compare with the findings of [14].

5.2 FRACTURE MECHANICS BASED SIZE-EFFECT IN SHCC

In [14] the size-effect between normal reinforced concrete, SHCC and a R/SHCC beam under flexural load (3-PBT) was compared. Where specimens with varying span, constant span to height ratio, and constant width have been tested. The nominal strength was plotted against a normalized beam height. These specimens ranged from small scale testing to 'reasonable' structurally sized specimen (span of 0.175 m to 2.8 m).

It was shown that in these specimens the reinforced concrete showed significant size-effect, while in the SHCC and R/SHCC beams there was little to no size-effect (Figure 5.1). The authors of this research attributed this to the different types of failure of reinforced concrete, and SHCC and R/SHCC beams. Reinforced concrete fails due to the localization of a single macro-crack which accommodates nearly all the deformation in the specimen. While SHCC and R/SHCC does not show this behavior and is characterized by the development of multiple cracks. Their explanation was that in quasi-brittle materials, such as reinforced concrete, the characteristic length l_{ch} is much smaller than in a ductile material like SHCC. Figure 5.2 shows the size-effect law for a quasi-brittle material. The nominal strength is plotted on the *y*-axis against the logarithmic nominal size on the *x*-axis. In this figure three zones are indicated: the most left is the strength zone where no size-effect exists, the middle zone is the non-linear fracture mechanics zone where mild size-effect exists, and the most right zone is the LEFM zone where strong size-effect exists. The size-effect in the LEFM zone is shown by a descending curve with slope of -0.5. As ductile material have longer l_{ch}, material with the same characteristic dimension D, tends to shift left along the x-axis. Compared to a quasi-brittle material, the nominal strength of big elements will shift all the way to the strength zone where no size-effect exists if the material is adequately ductile. This has also been backed up by diminished size-effect for specimens with increasing fiber volume content (1.0, 1.5 and 2.0 %) and hence ductility.

It was noted that although size-effect was limited for SHCC it was not entirely eliminated. This is because other sources of size-effect, such as the Wall effect statistical size-effect (Weibull's weakest link statistics), are probably still present. The authors suggested future research can be performed in these areas.

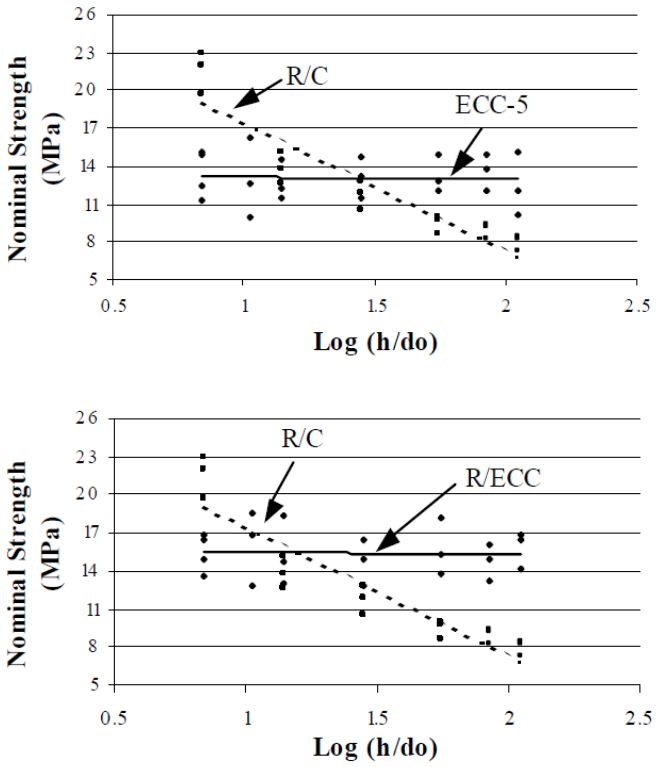

Figure 5.1 Size-effect in R/C, SHCC (2% volume content), and R/SHCC specimens [14].

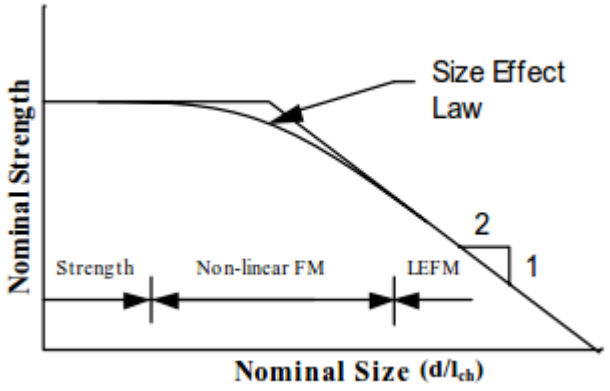

Figure 5.2 Size-effect law for concrete or other quasi brittle material [14].

5.3 EXPERIMENTAL SET-UP

5.3.1 WORKABILITY TEST

Aside from the inner dimensions of the V-funnel test, the test setup of the workability tests is the same as described in chapter 3.4.2. The different setup for the V-funnel test was due to the available lab equipment. The V-funnel test in this chapter is suited for mixtures with particle group of 0-16 mm, while the one in chapter 3.4.2 for 0-8 mm [15].

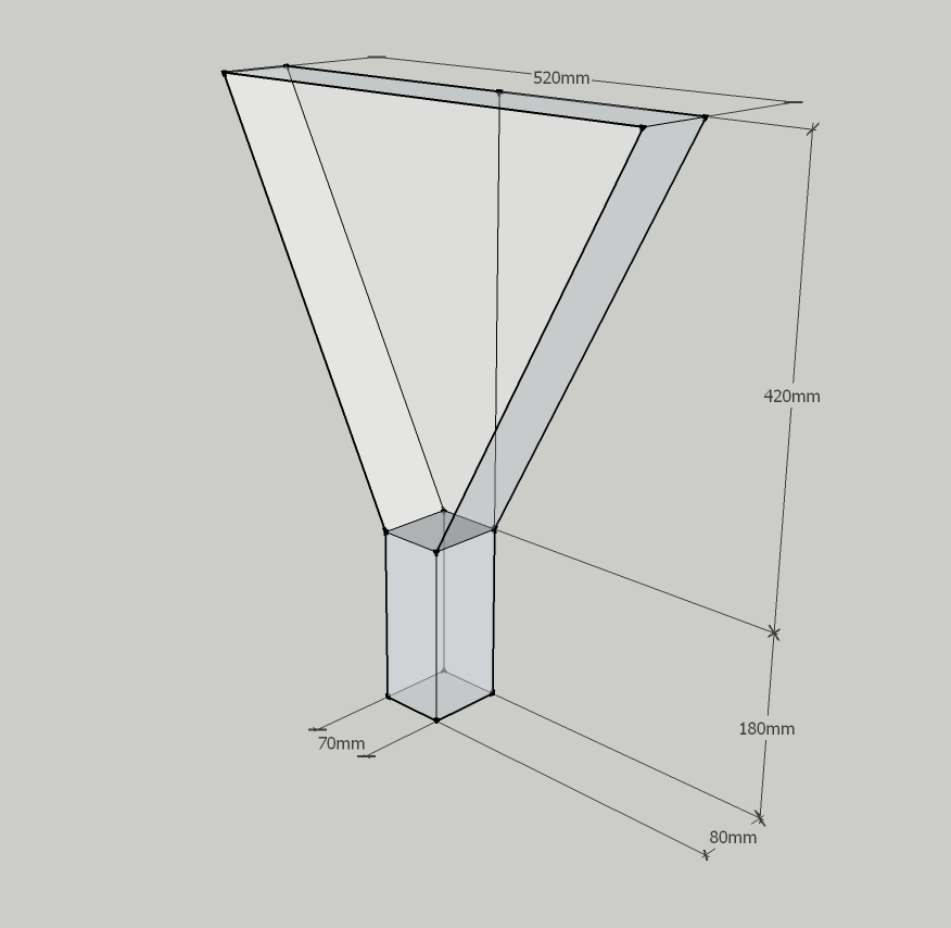

Figure 5.3 Inner dimensions for the V-funnel test in chapter 5.

5.3.2 MECHANICAL TEST

Due to the high range of span length the FM-175 and FM-350 specimens will be tested in the same test setup as in chapter 3.4.1, while the FM-700 and FM-2100 specimens in the setup shown in Figure 5.4. For the specimen coding see Figure 5.7 and Table 5.3.

The test setup of the FM-700 and FM-2100 specimens consists of a steel framework and a piston with a capacity of approximately 100 kN. Between the piston and specimen a steel block is used to spread the load of the piston into the two inner support loads. The weight of the steel block is 11.8 and 16.3 kg for respectively the FM700 and FM2100 specimens.

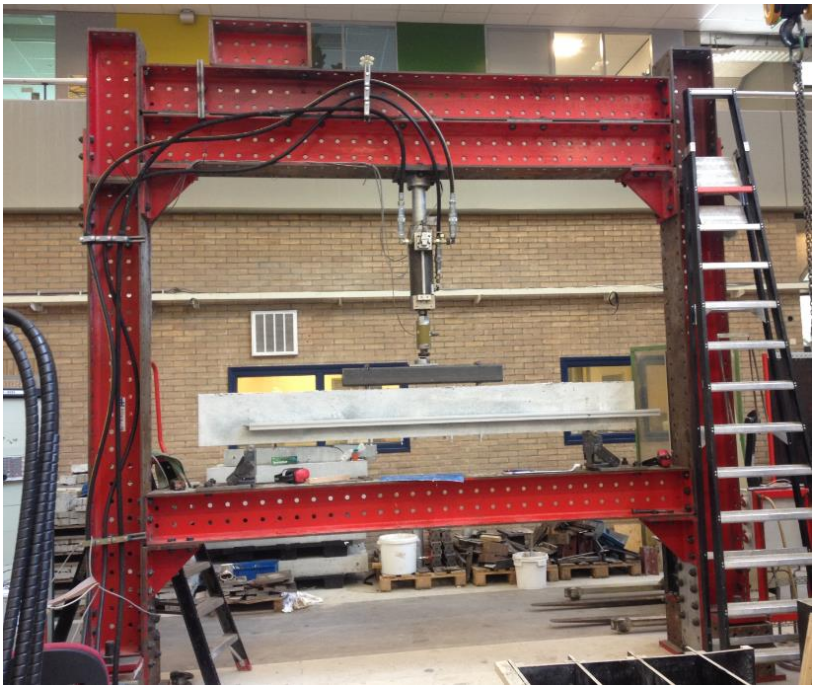

Figure 5.4 4-PBT setup for the FM-700 and FM-2100 specimens.

The setup for the cubical compression test is shown in Figure 5.5. The specimen will be put in between two steel plates which exert the compressive force.

Figure 5.5 Test setup for the cube compression test in chapter 5.

5.4 EXPERIMENTAL PROCEDURE

To solely investigate the fracture mechanics based size-effect other sources of size-effect have to be eliminated or diminished as much as possible. These includes size-effect introduced by the Wall-effect, diffusion phenomena, hydration heat, and statistical inhomogeneity of the material. By increasing the specimen span while retaining a constant thickness and span to height ratio one can achieve this.

5.4.1 MIX DESIGN

Table 5.1 shows the mix design of this experimental series. Compared to the prior mix designs in this thesis it has a reduced w/p. This was in order to increase the low V-funnel flow time which was recorded during test batching. A higher flow time was desired because it related to a better fiber dispersion according to literature study.

Three batches were made to produce all specimens. The first batch had a w/p of 0.25. However during charging of the mixing water an unknown amount of water leaked away. Therefor the exact w/p is unknown, but smaller than 0.25. For the second and third batch the w/p is 0.23.

Table 5.1 Mix design used in chapter 5.

Mix	CEM III/B 42.5 N LH HSR	LP	BFS	w/p	SP	PVA fiber (by volume)
Batch 1	1	1	-	<0.25*	0.0027	2%
Batch 2	1	1	-	0.23	0.0027	2%
Batch 3	1	1	-	0.23	0.0027	2%

**See text above.*

5.4.2 SPECIMEN PREPARATION

The mix procedure has been adjusted compared to previous experiments. This was due to the amount of volume that has to be mixed which led to the use of large scale mixing equipment (Figure 5.6). The procedure is based on the mixing procedure in [16] and shown in Table 2.10.

Table 5.2 Mixing procedure for specimens in chapter 5.

Activity no.	Activity	Elapsed time (minutes)
1	Charge all dry ingredients	4
2	Charge mixing water and all superplasticizer	4
3	Mix for 5 minutes or until material is homogeneous	5
4	Charge fibers	2
5	Mix for 5 minutes or until material is homogeneous	5
6	Slump and funnel time test	
7	Mix at high rpm for 5 minutes or until material is homogeneous	5
	Total	25

Figure 5.6 Mixing equipment for large scale production of SHCC.

In step 6 of the mixing procedure the plastic mixture will be tested for workability with the V-funnel test and mini-slump test as described in respectively chapter 3.5.2.1 and 3.5.2.2. After the workability tests the specimens will be casted in the molds and covered with plastic foil. Placement of the fresh SHCC is done by hand-scooping into the mold. After 28±1 days the specimens will be tested. One day prior to testing the specimens are demolded and painted with chalk and black spraying paint. This was done in order to apply the Digital Image Correlation (DIC) technique for accurate image analysis (see chapter 5.4.4).

Specimen geometry are shown Figure 5.7 and Table 5.3. The width of the beam is kept constant at 0.075 m. Each geometry of the beam will be produced three times. Three batches of approximately 100L had to be made to produce all specimens. To accommodate for batch variances, each batch was used to fill one of the three specimens of each geometry. Along with casting of the beams, three cubes of 150*150*150 mm^3 were casted for compression tests.

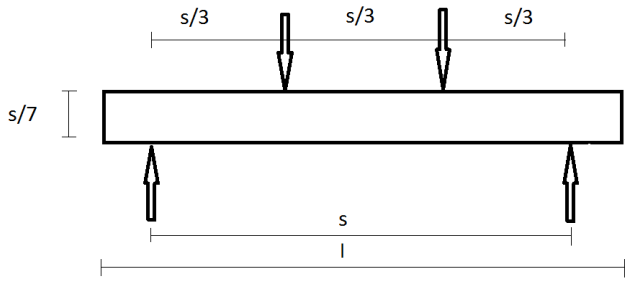

Figure 5.7 Specimen geometry. For length (l) and span (s) see Table 5.3.

Table 5.3 Specimen coding span lengths.

Specimen code*	Span [m]	Length [m]
FM-175#$_i$	0.175	0.225
FM-350#$_i$	0.35	0.45
FM-700#$_i$	0.7	0.9
FM-2100#$_i$	2.1	2.7
**With #$_i$ for specimen number, with i = 1, 2, and 3.*		

5.4.2.1 LVDT PLACEMENT

For the FM-175 and FM-350 specimens LVDTs are used to measure the horizontal displacement in the maximum moment field as displayed in Figure 5.8 and Figure 5.9. The vertical displacement is measured with the INSTRON machine. For the FM-700 and FM-700 specimens LVDTs are used to measure the horizontal displacement in the maximum moment field as displayed in Figure 5.10 and Figure 5.11. The vertical displacement of these specimens are measured with a LVDT since the vertical displacement measured in the piston might be inaccurate due to possible deformation of the steel framework. The LVDT measures between the bottom of the beam with respect to the neutral axis above the outer supports. A construction was designed for his purpose and shown in Figure 5.12.

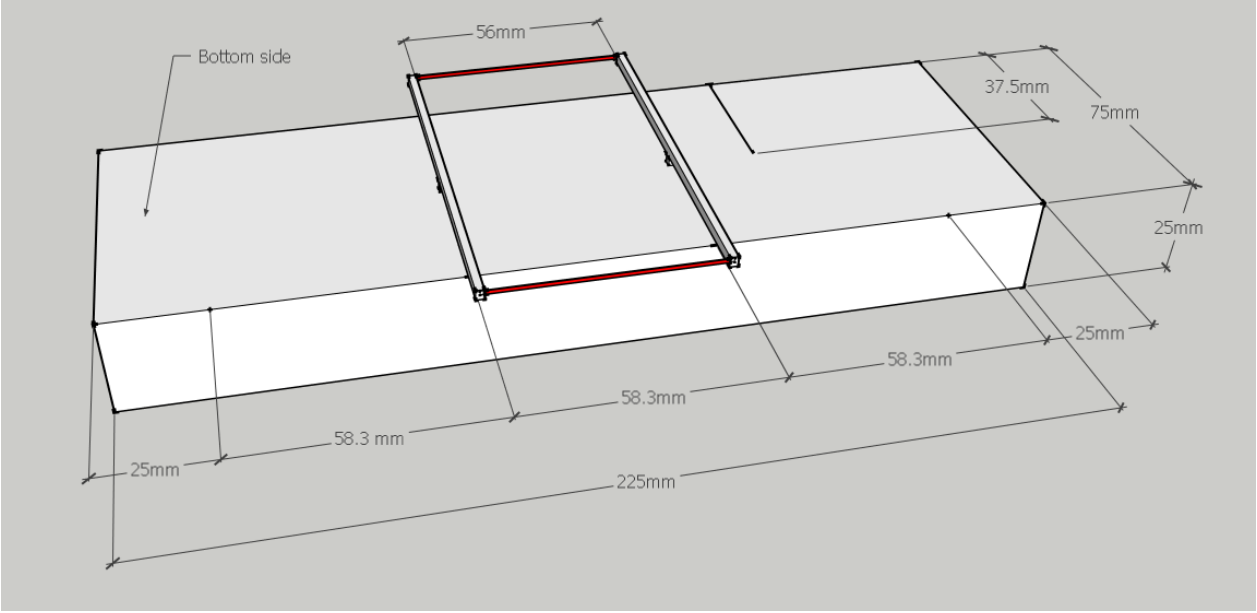

Figure 5.8 Placement of the LVDTs for the FM-175 specimens on bottom side. LVDTs measures between red lines.

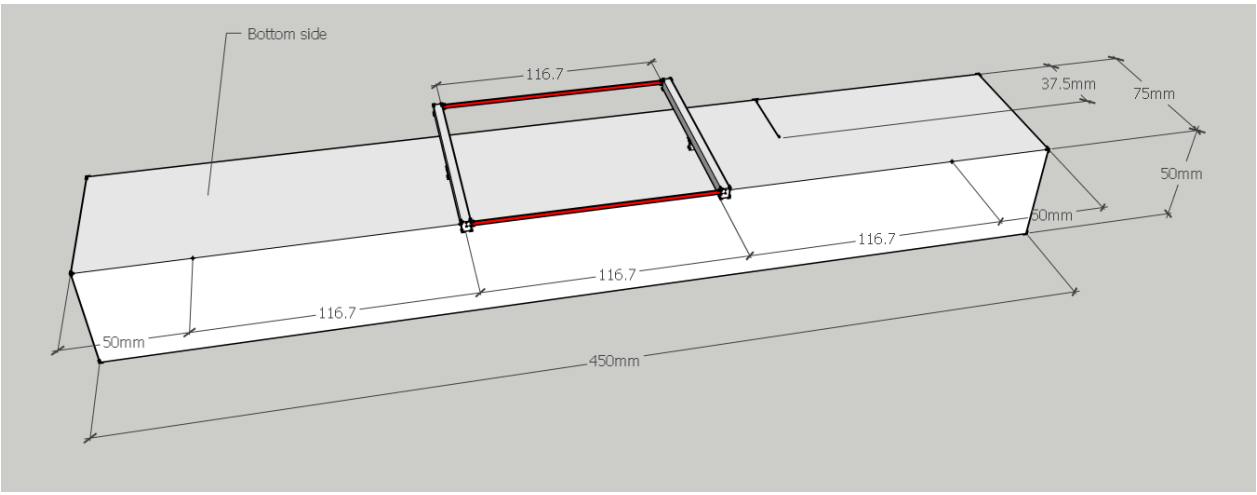

Figure 5.9 Placement of the LVDTs for the FM-350 specimens on bottom side. LVDTs measures between red lines.

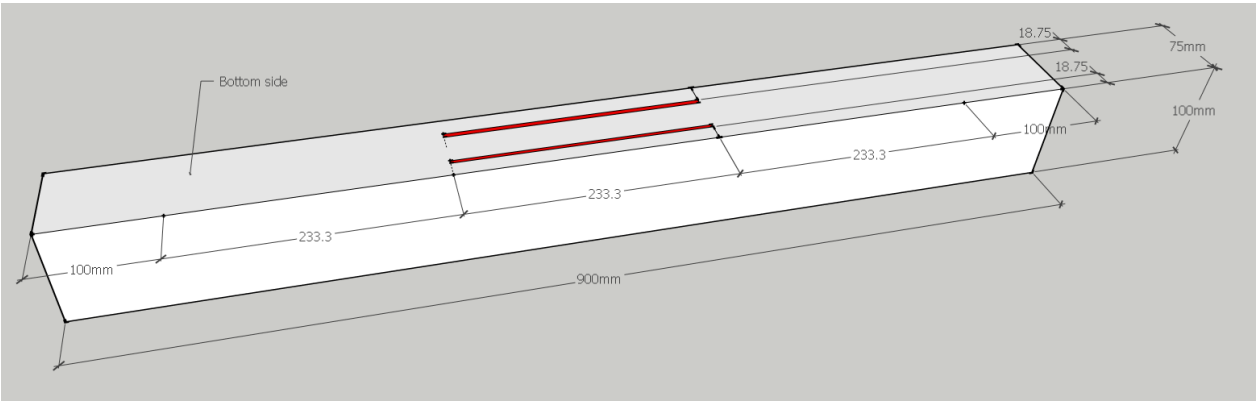

Figure 5.10 Placement of the LVDTs for the FM-700 specimens on bottom side. LVDTs measures between red lines.

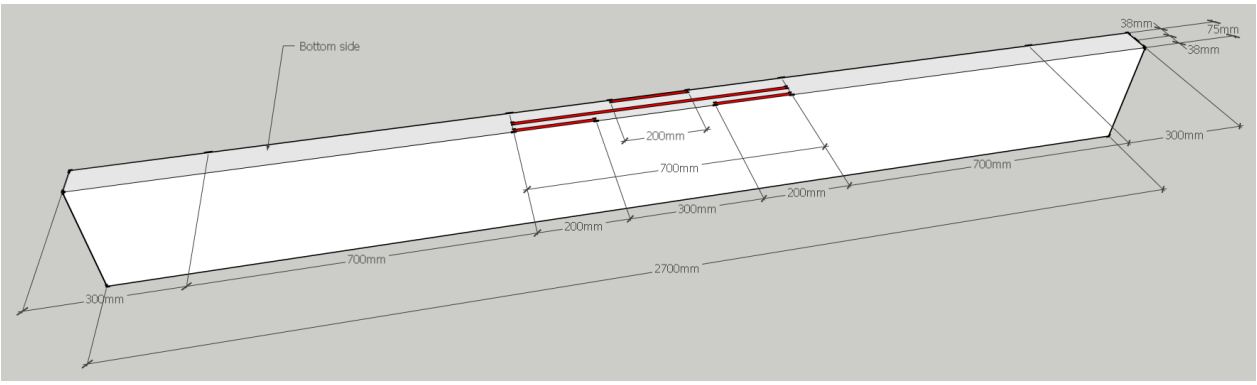

Figure 5.11 Placement of the LVDTs for the FM-2100 specimens on bottom side. LVDTs measures between red lines.

Figure 5.12 Setup for the measurement of the vertical displacement with LVDT for specimens FM-700 and FM-2100.

5.4.3 MECHANICAL TESTING

It was not possible to test all specimens in 4-PBT on one day. Therefor it is chosen to test the specimens in a span of three days with an age of 32±1 days. The 4-PBT is displacement controlled with a displacement rate shown in Table 5.4. Stress-strain curves are constructed by calculating the stress and strain as described in respectively chapter 3.5.3.1 and (eq. 3.8). In addition a camera is set to make photos at a constant time interval. With DIC software [17] the displacement of the beam during testing has been tracked. For more information see chapter 5.4.4.

Table 5.4 Displacement rate of 4-PBT.

Specimen name	Displacement rate [mm/s]
FM-175#$_i$	0.01
FM-350#$_i$	0.01
FM-700#$_i$	0.01
FM-2100#$_i$	0.01

Cube compression tests will all be performed at 28 day age so the results can be compared with ordinary concrete. A specimen will be placed in testing apparatus and loaded at constant rate of 13.5 kN. The testing apparatus will automatically stop when failure has reached.

5.4.4 DIGITAL IMAGE CORRELATION (DIC)

Digital image correlation (DIC) is a technique that tracks the movement of the pixels during testing. During the mechanical test images are taken at a constant time interval. Correlation calculations which are based on the pattern and the gray level of each individual pixel make it possible to track the pixel movement.

This technique has been used to make a plot of the strain in the maximum moment of field on the side surface, where after the strain between two points in the image could be measured. The camera was set taking photos from the side of the specimen as in Figure 5.13. During the 4-PBT photos were taken at a time interval of 5 seconds. The first image is used as a base image and markers are positioned in a grid over a specified area (Figure 5.14). The distance between the markers are shown in Table 5.5. The distance between the vertical markers are increased to decrease the computation time. The distance between the horizontal markers are kept the same. With this marker grid one can maintain good resolution over the horizontal displacement while measure the strain along the height. After

correlation calculation one can construct a series of images of the pixel displacement at each position in the marker grid (Figure 5.15) and also a corresponding gradient plot of the strain (Figure 5.16). This plot can be used to select two points where the strain will be measured in between.

Table 5.5 Pixels between the horizontal and vertical markers.

Specimen	Pixels between horizontal markers [-]	Pixels between vertical markers [-]
FM175	25	25
FM350	25	25
FM700	25	150
FM2100	25	150

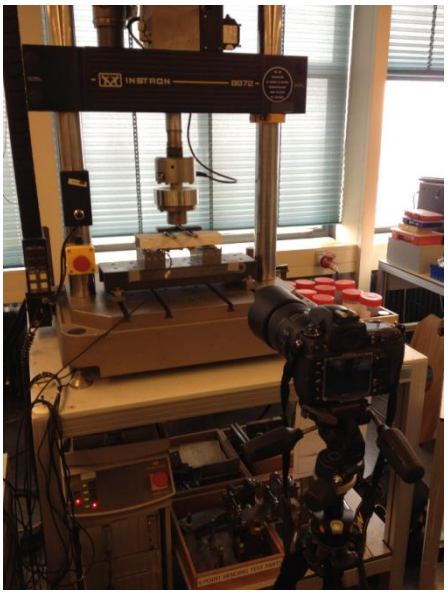

Figure 5.13 Setup for the DIC technique.

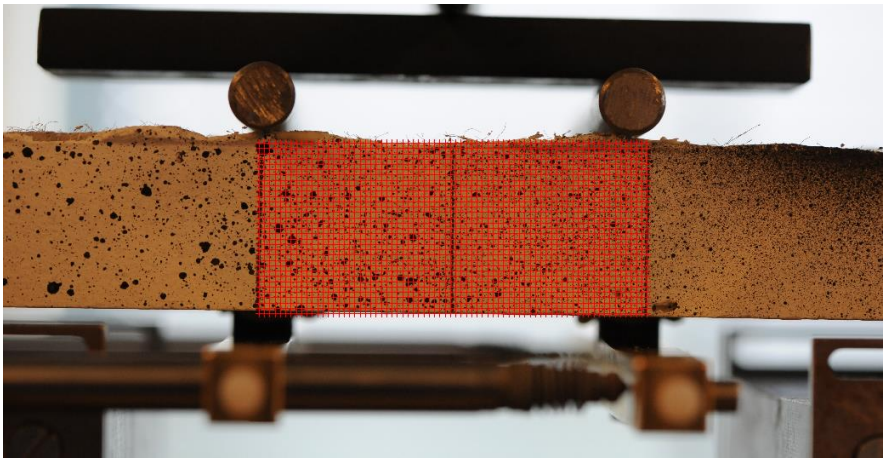

Figure 5.14 Example of grid of markers positioned over the area of interest.

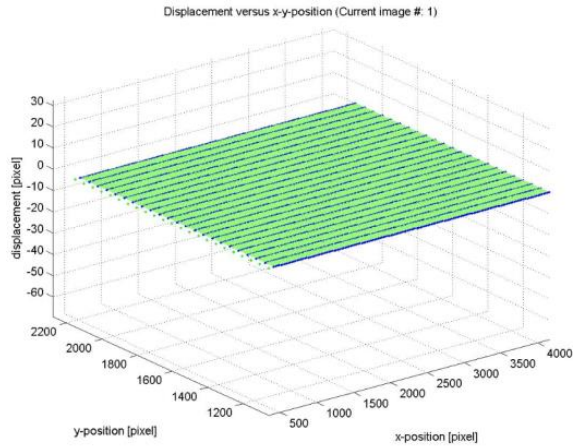

.....

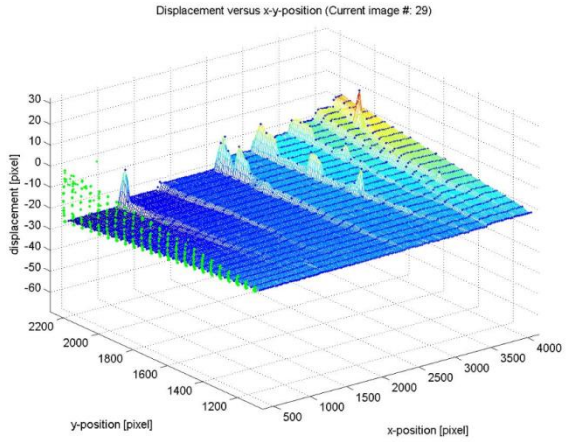

.....

.....

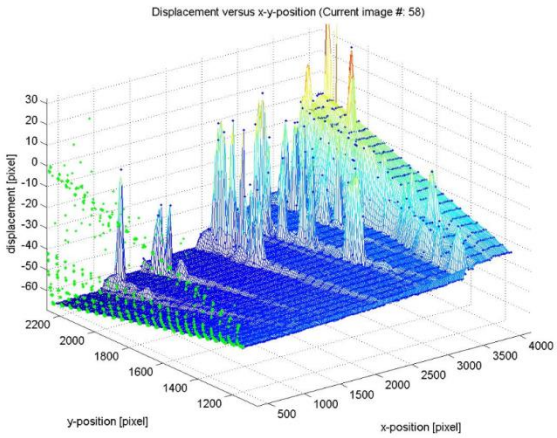

Figure 5.15 Example of displacement of markers over time.

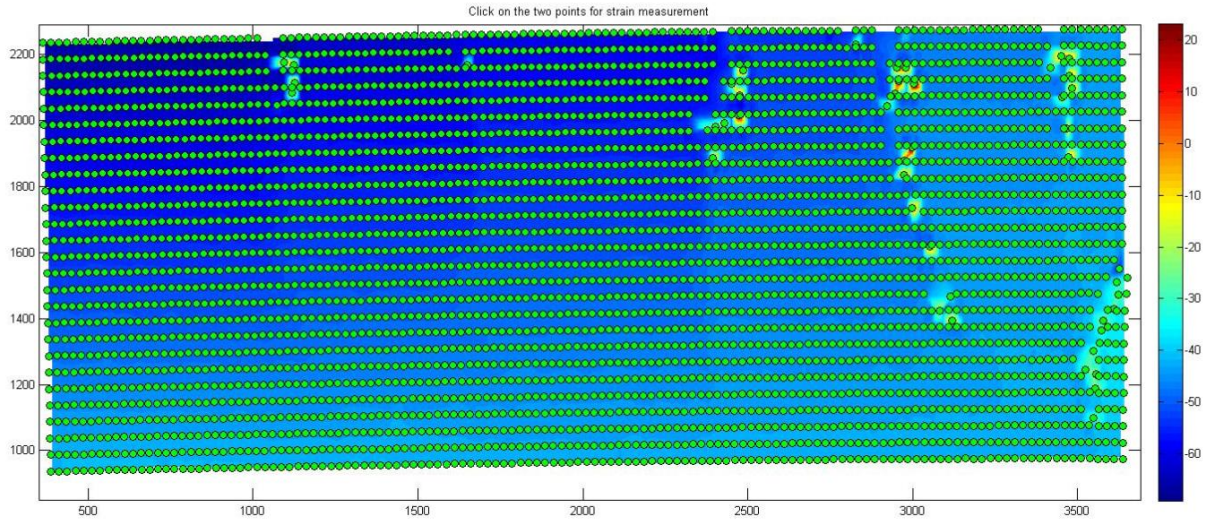

Figure 5.16 Example of gradient plot of the strain.

The position and number of cracks in the plots of Figure 5.15 will be compared with the photographs to verify the DIC results. From the gradient plots, for example Figure 5.16, a strain diagram along the height of the cross section in the constant maximum moment field and the crack width along the crack will be constructed and analyzed.

5.5 RESULTS AND DISCUSSION

5.5.1 WORKABILITY

The mini-slump diameter and V-funnel flow time are shown in respectively Table 5.6 and Table 5.7. The mini-slump diameters are all within the SF1 consistence class and is sufficient for self-compacting concrete for our purposes (chapter 3.6.1). The V-funnel flow time is in VF1 class and is favorable for self-compacting concrete, but predicts a poor fiber dispersion. After batch 1 it has been tried to increase the flow time by reducing the w/p to 0.23. Ultimately it did not lead to the desired flow time. However in chapter 4 it was found that reasonable fiber dispersion and orientation was found with lower flow time than the literature study. Therefor these results have been accepted.

Table 5.6 Mini-slump diameter of the batches.

	Mini-slump diameter[mm]
Batch 1	63.5
Batch 2	63.5
Batch 3	61.5

Table 5.7 V-funnel flow time of the batches.

	V-funnel flow time [s]
Batch 1	2.7
Batch 2	3.6
Batch 3	2.7

5.5.2 MECHANICAL PERFORMANCE

During testing multiple LVDTs at different locations and measuring lengths have been utilized. In the figures below all LVDTs shown in chapter 5.4.2.1 that cross an entire maximum moment of field have been used to calculate the strain. This means the three LVDTs that measure over distance of 20 mm in the FM2100 specimens have been excluded in the results. When choosing different measuring length for the LVDTs the stress-strain diagram will be influenced. If a cracks appears energy dissipates and there is relaxation of the elastically stretched parts next to the crack. One can compare this to a elastically stretched a rubber band when a small tear develops which unloads the elastic strain. This effect is more pronounced when the measured length of the LVDT is increased. However in an experiment where the nominal strength is different between the specimens one will find a different magnitude of this effect if the measured length is kept the same. If the measured length is exactly as the width of the crack band than theoretically this effect is zero. With the DIC technique one can choose the measuring length and then minimize this effect.

Figure 5.17 to Figure 5.20 show the stress-strain diagrams of the specimens. All specimens show strain-hardening. It seems that there is a gradual drop in strain-capacity when increasing the specimen span. The nominal strength seem to remain constant for the three smallest sizes. It is very clear that the FM2100 specimens have significantly less nominal strength and strain capacity.
Low strain capacity can be explained by a quick localization to a single macro crack in the specimen. This was also observed during the test and post-testing examination of the crack pattern for the specimens FM350-002 and FM2100.

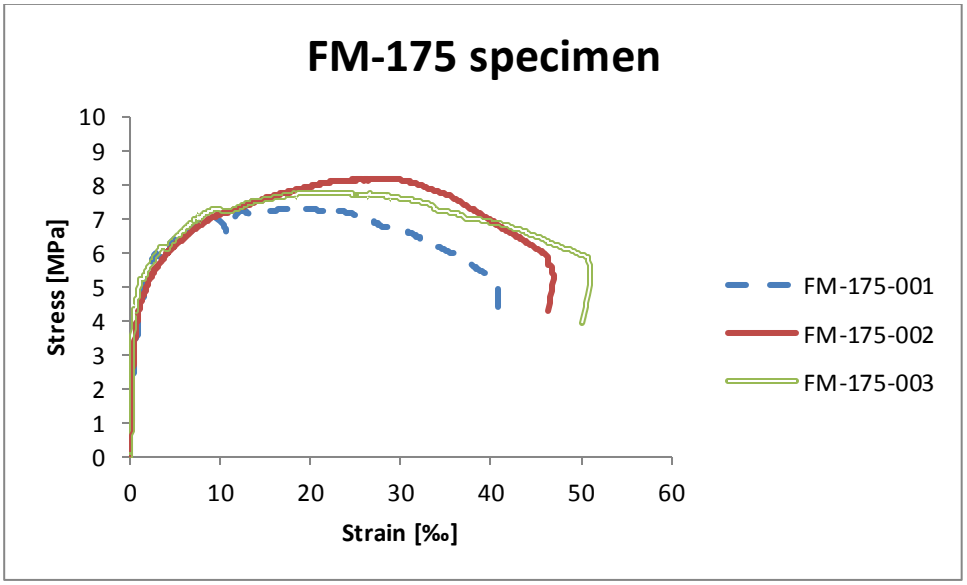

Figure 5.17 Stress-strain diagram of FM-175.

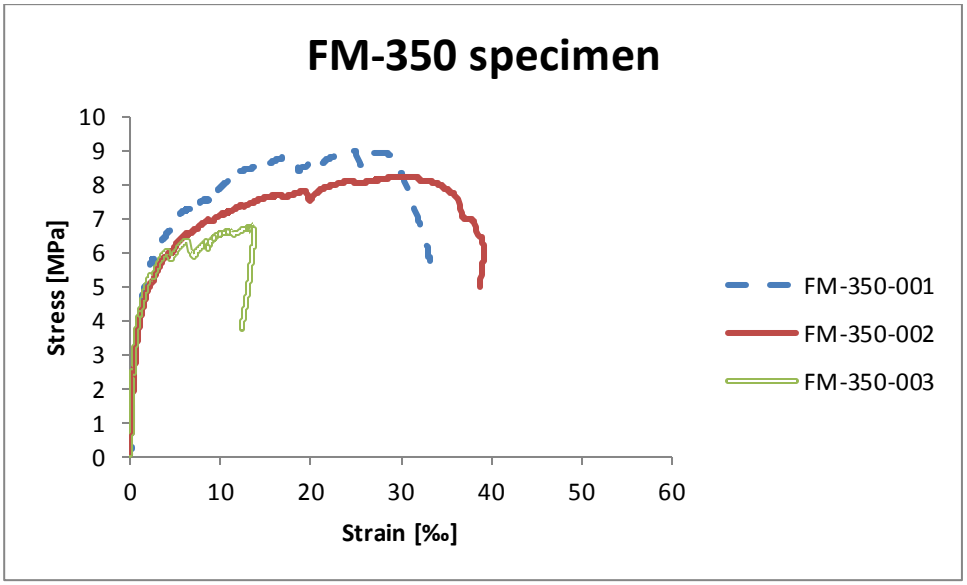

Figure 5.18 Stress-strain diagram of FM-350.

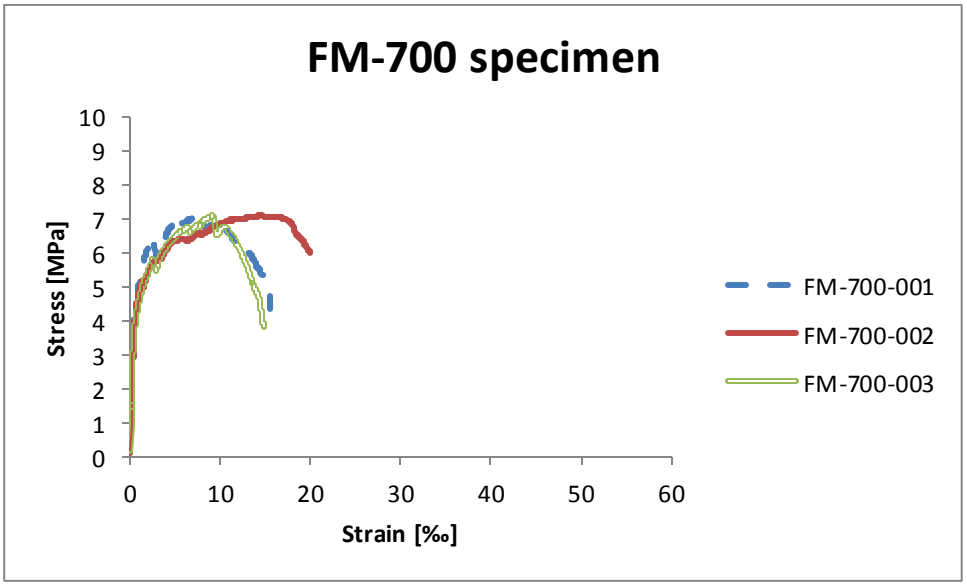

Figure 5.19 Stress-strain diagram of FM-700.

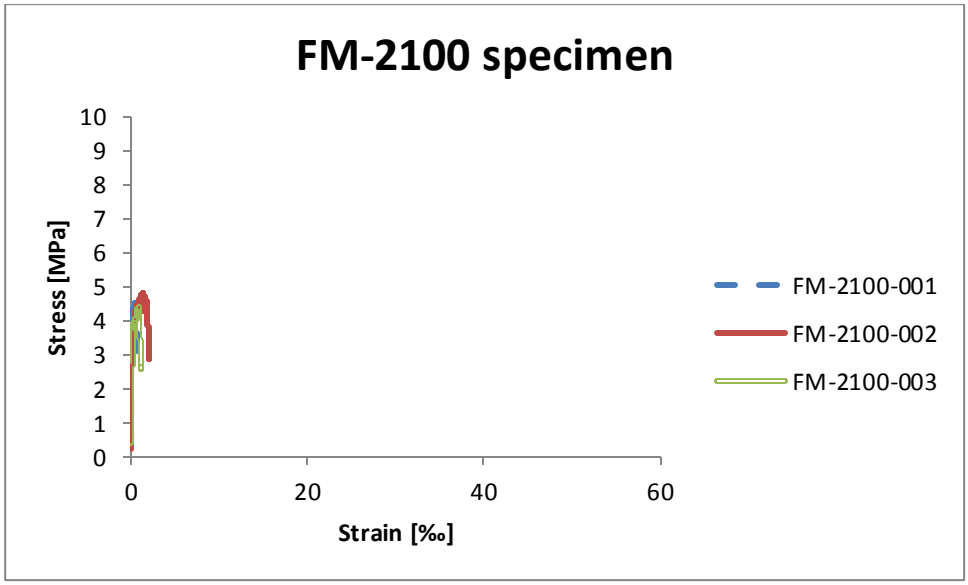

Figure 5.20 Stress-strain diagram of FM-2100.

In Figure 5.21 the nominal strength is plotted against the logarithmic *D*, where *D* is the specimen span. A linear trend line (black) has been included to compare with the results in research [14]. For a better fit a polynomial trend line (red) was fitted between the data point. This trend line shows a trend line more similar to that of ordinary concrete. The difference between the red trend line and that of research [14] is due to the lower nominal strength for the FM2100 specimens. The difference can be explained by the following model.

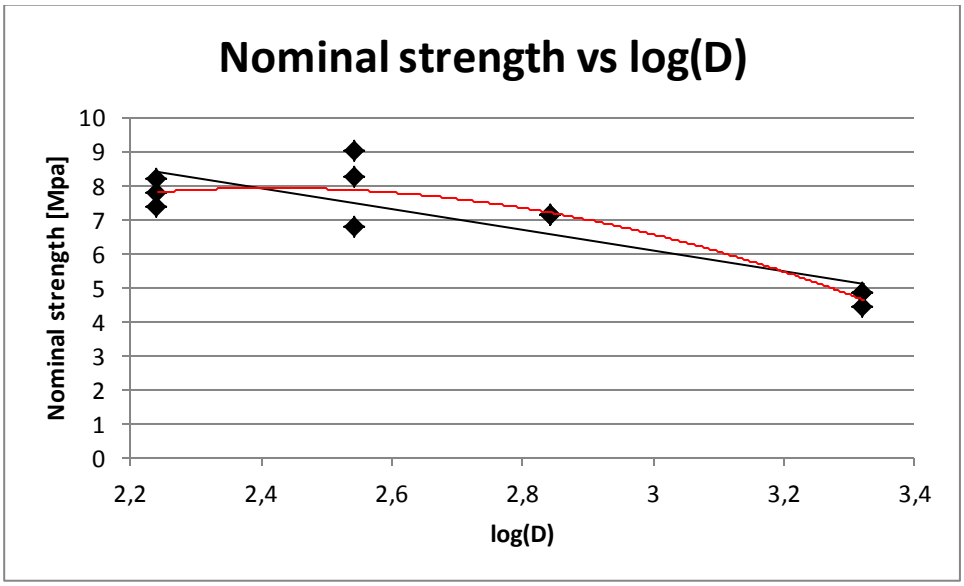

Figure 5.21 Size-effect in the SHCC specimens with linear trend line (black) and polynomic trend line (red).

This model is based on the length of the strain-hardening branch in the stress-strain diagram. If there is a crack in the specimen one can attribute the strength along the cracked cross section based on the

stress-strain diagram. In case of ordinary concrete, consider the moment just before failure which is at the point of limit of LOP, the strength of the crack tip is the nominal strength in the stress-strain diagram and gradually decreases since crack width is greater at crack mouth. This situation is depicted with the markers in Figure 5.22 a. Further loading will widen the crack and the strength along the crack will decrease as depicted in Figure 5.22 b. When the applied load is the same or increased then the diminished strength will lead to specimen failure.
In SHCC this is different, the specimen will not decrease in strength after LOP. The strength of the composite along the crack width where the first crack is fully developed is shown in Figure 5.22 c. When the crack is widened fibers may not be able to bridge the crack and the strength at bigger crack width is decreased as shown in Figure 5.22 d. As long there is an increase in the strength during widening of the crack the specimen will not fail. Only if one of the markers in the figure has moved horizontal past the nominal strength then the specimen will fail.

This model can explain size-effect if the crack width is higher for specimen with bigger size. This will be verified in chapter 5.5.3.3.

Based on this model, one possible explanation of the diminished nominal strength of the FM2100 specimens is that the strain-hardening branch in the stress-strain diagram is not long enough. When size of the specimens is increased the crack width increases faster than for smaller specimens. Resulting in a quicker horizontal shift of the markers as depicted in Figure 5.22.

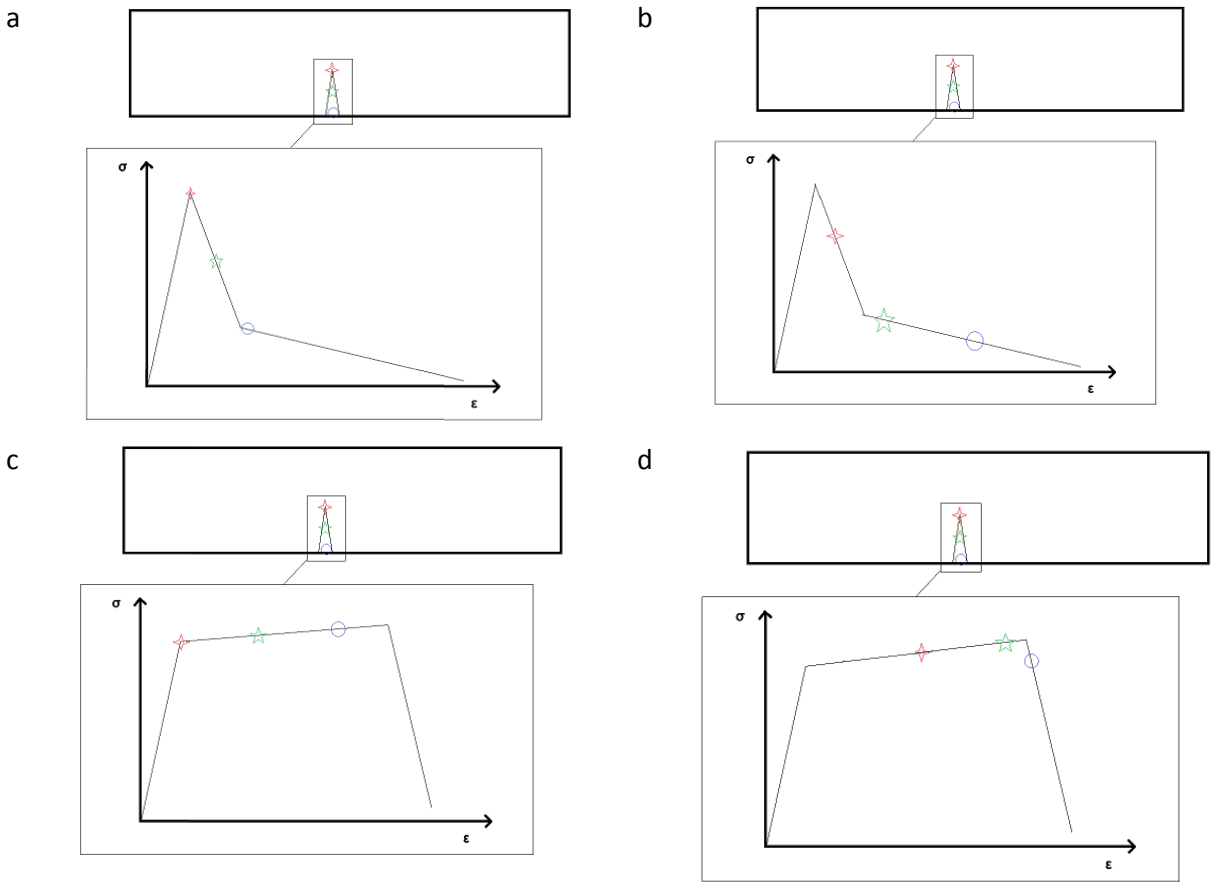

Figure 5.22 Theoretical model to explain size-effect in SHCC. Stress-strain diagram with markers corresponding to markers along the crack in a specimen.

It is worthy to note that in chapter 3 size-effect was found in a smaller increase of element size. From the results above it can be concluded that this size-effect was not caused by the fracture mechanics based size-effect. In that experiment the specimen width was not kept constant, therefor sources mentioned in chapter 2.5 could be the reason for the size-effect.

In Figure 5.23 the strain capacity is plotted against the logarithmic D. It shows a very clear drop in the strain capacity. Since in many applications of SHCC strain capacity is one of the most important characteristic, this is a crucial discovery. In research [14] the focus was on the nominal strength when the element size was upscaled. However for SHCC it is much more interesting to focus on the strain capacity when the element size is upscaled, because high strain capacity is inherent to the development of multiple fine cracks and leads to increased durability when designed correctly.
The explanation of this drop in strain capacity is that, as mentioned above, the crack width might be bigger with increased size. Leading to a higher possibility of a Griffith type of crack instead of the steady state flat cracks (Figure 2.3). This results to the development of fewer number of cracks and thus a lower strain capacity.

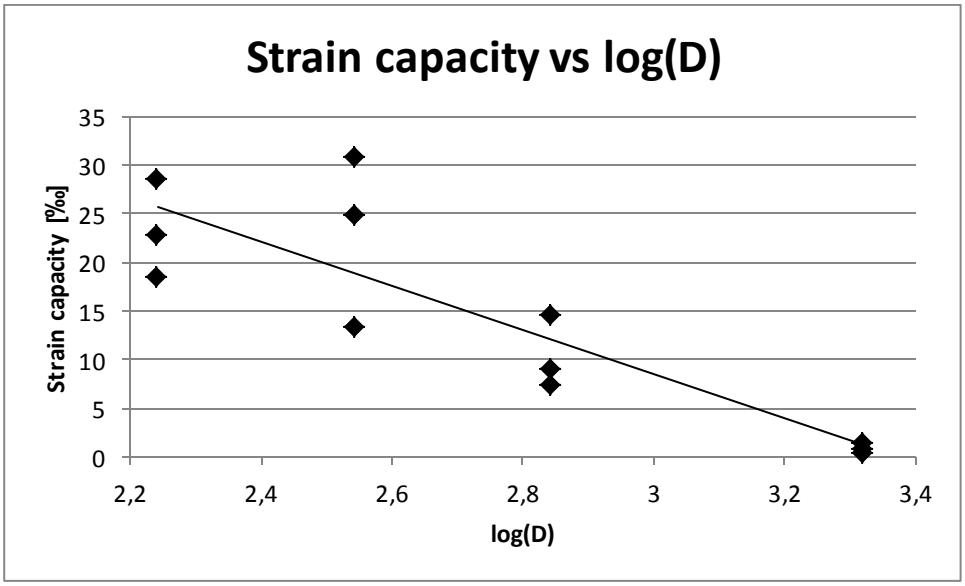

Figure 5.23 Strain capacity in the SHCC specimens.

Also noteworthy is the variation of the LVDT in the FM700 and FM2100 specimens. These specimens were all tested in the same test setup, where localization of the macro crack consistently occurred at one same side of the test setup. Most probably this was due uneven loading by the piston. Calibration of the test setup and/or reproducing the tests at a different setup might provide a solution.

Lastly, for comparative reasons with ordinary concrete or other materials the cubic compressive strength at 28 days age is given in
Table 5.8.

Table 5.8 Cubic compressive strength at 28 days.

Batch	Compressive strength [MPa]
1	57.85
2	55.76
3	57.65

5.5.3 DIGITAL IMAGE CORRELATION

In this chapter the DIC analysis is performed on the specimens FM175-001, FM350-003, FM700-002, and FM2100-001. First a verification of this technique is performed by comparing crack pattern of the specimens and the results obtained with the DIC technique. Furthermore the strain calculated from the LVDT will be compared to the DIC strain. Finally the development of the crack width along the height of a crack is analyzed to verify the assumption made in our theoretical model.

Important is to note that the display of images by ordinary image software and the DIC software (Matlab script) is different. In ordinary image software the pixel (1,1) starts at the top left corner and for Matlab at the bottom left corner. This leads to mirrored images around the horizontal axis when comparing Matlab generated images with normal images.

5.5.3.1 VERIFICATION DIC RESULTS

Figure 5.24 to Figure 5.27 show the displacement in pixels versus the position of the pixel in the image. The horizontal position is described by the x-position axis, while the vertical position by the y-position axis. It can be seen that very good correlation exists between the cracks, marked with a green line in the pictures, and the peaks in the displacement versus position plot.

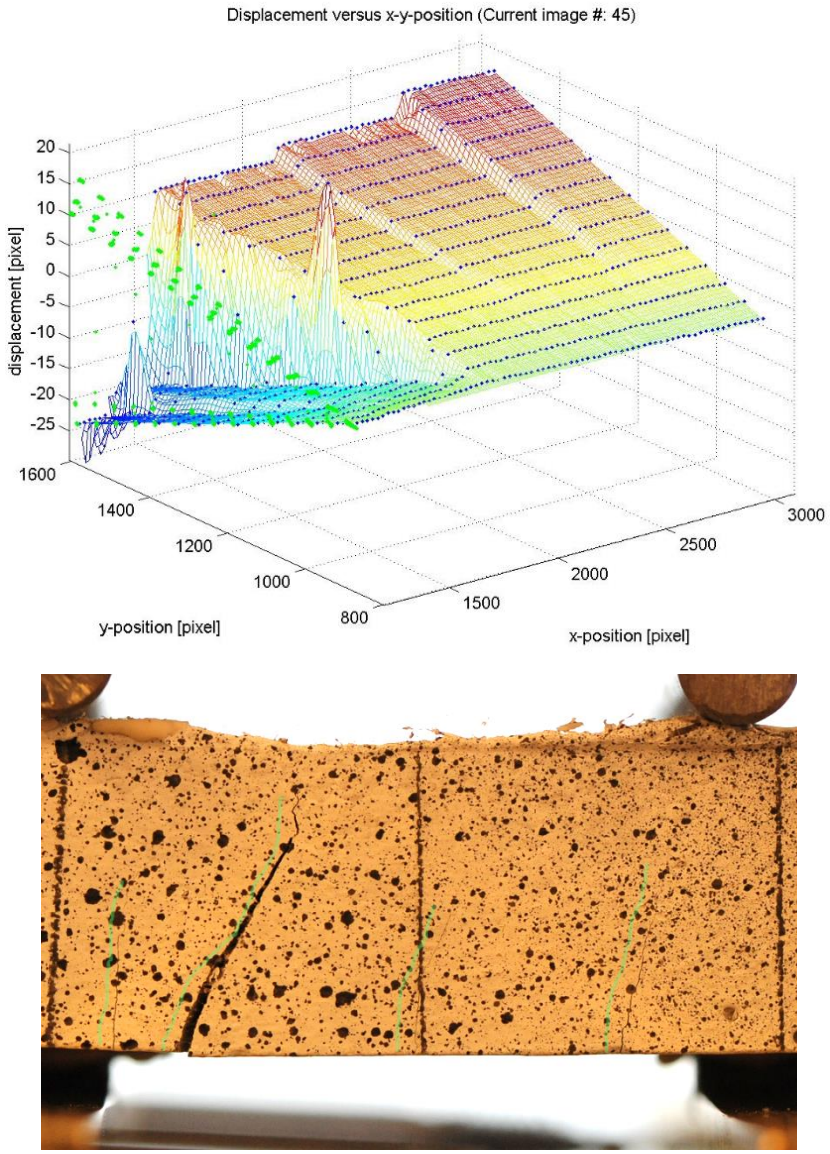

Figure 5.24 The displacement versus the pixel location (upper) for specimen FM175-001, and corresponding picture with cracks highlighted with green lines (lower).

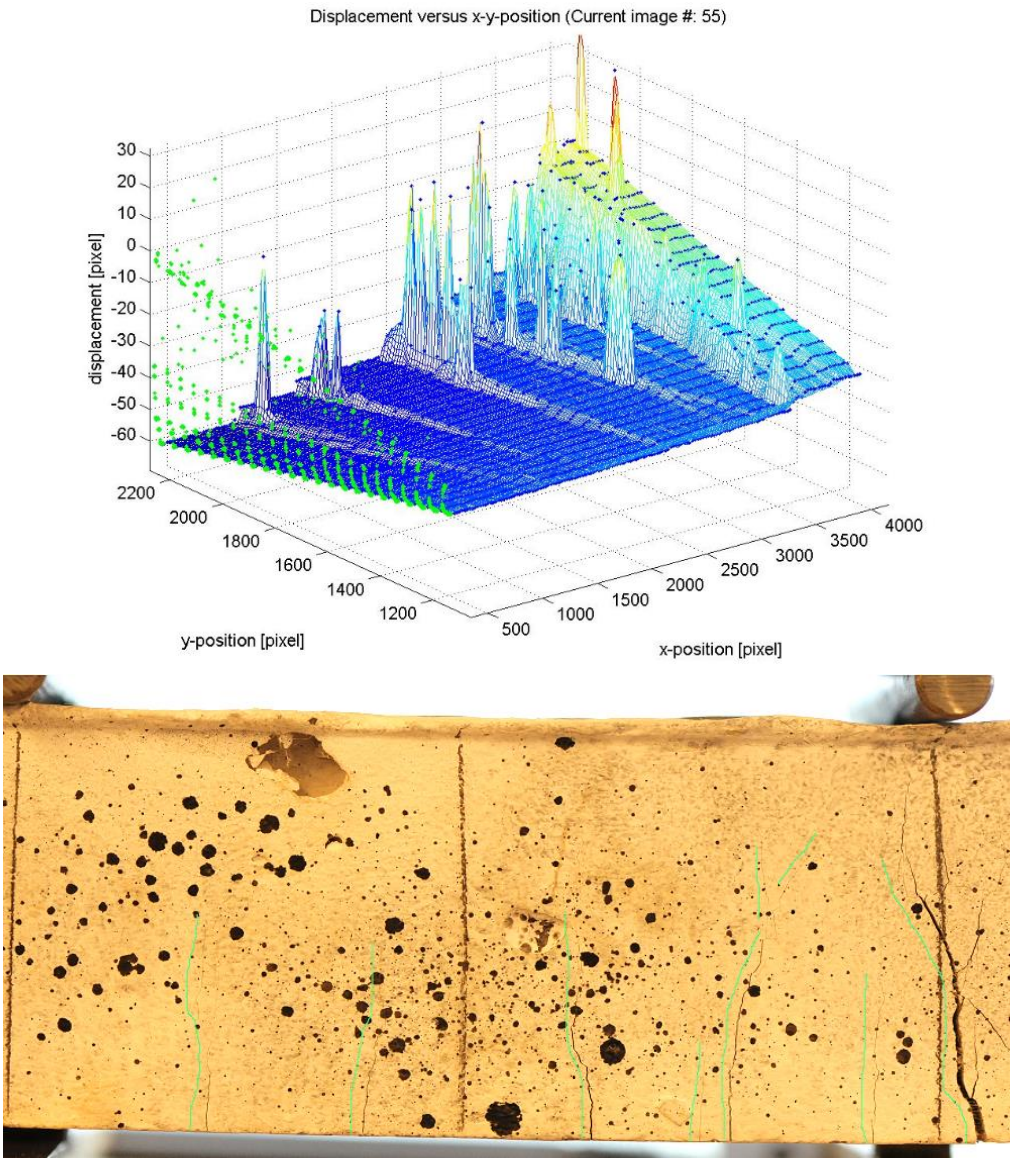

Figure 5.25 The displacement versus the pixel location (upper) for specimen FM350-003, and corresponding picture of analyzed area with cracks highlighted with green lines (lower).

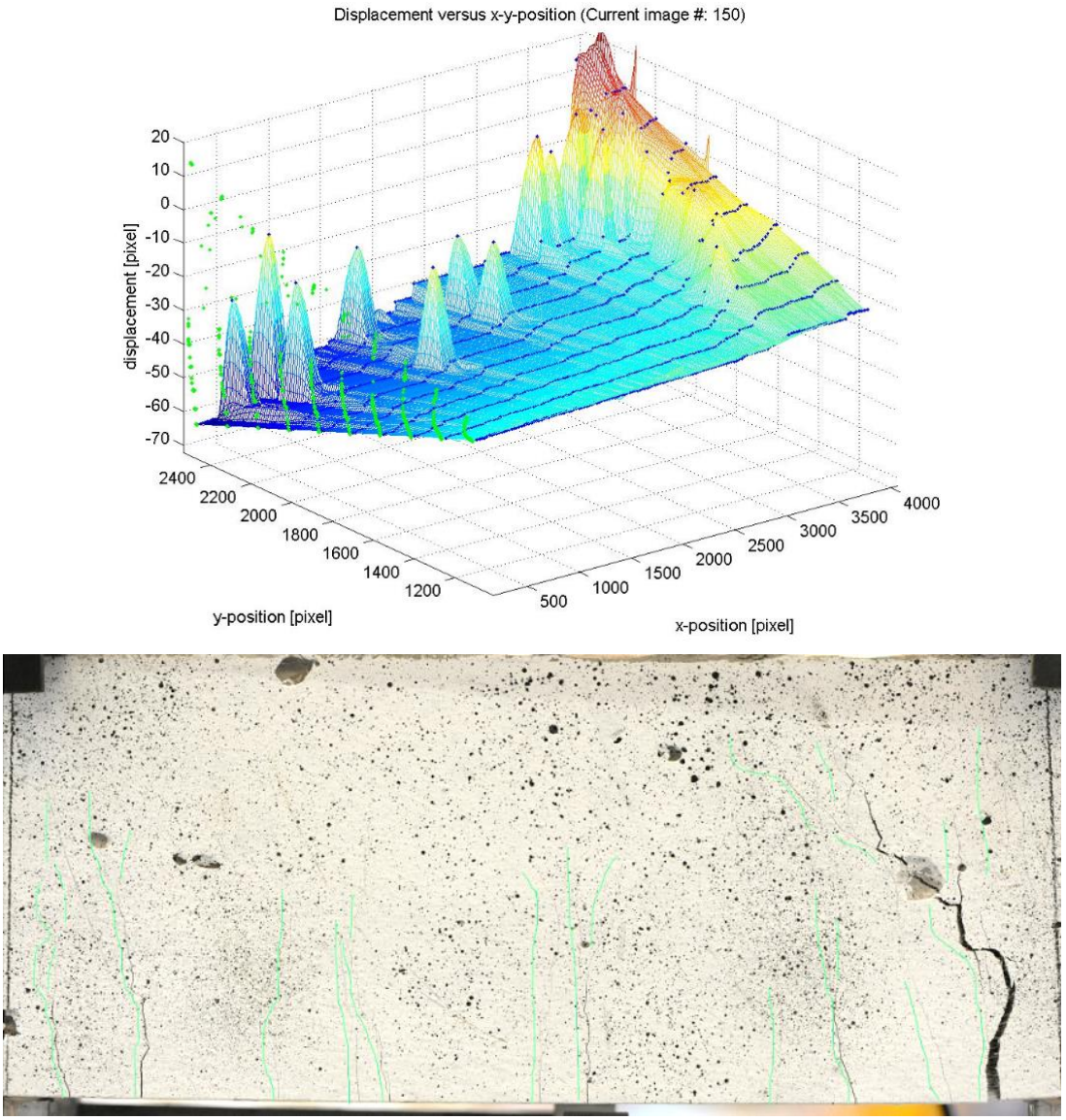

Figure 5.26 The displacement versus the pixel location (upper) for specimen FM700-002, and corresponding picture of analyzed area with cracks highlighted with green lines (lower).

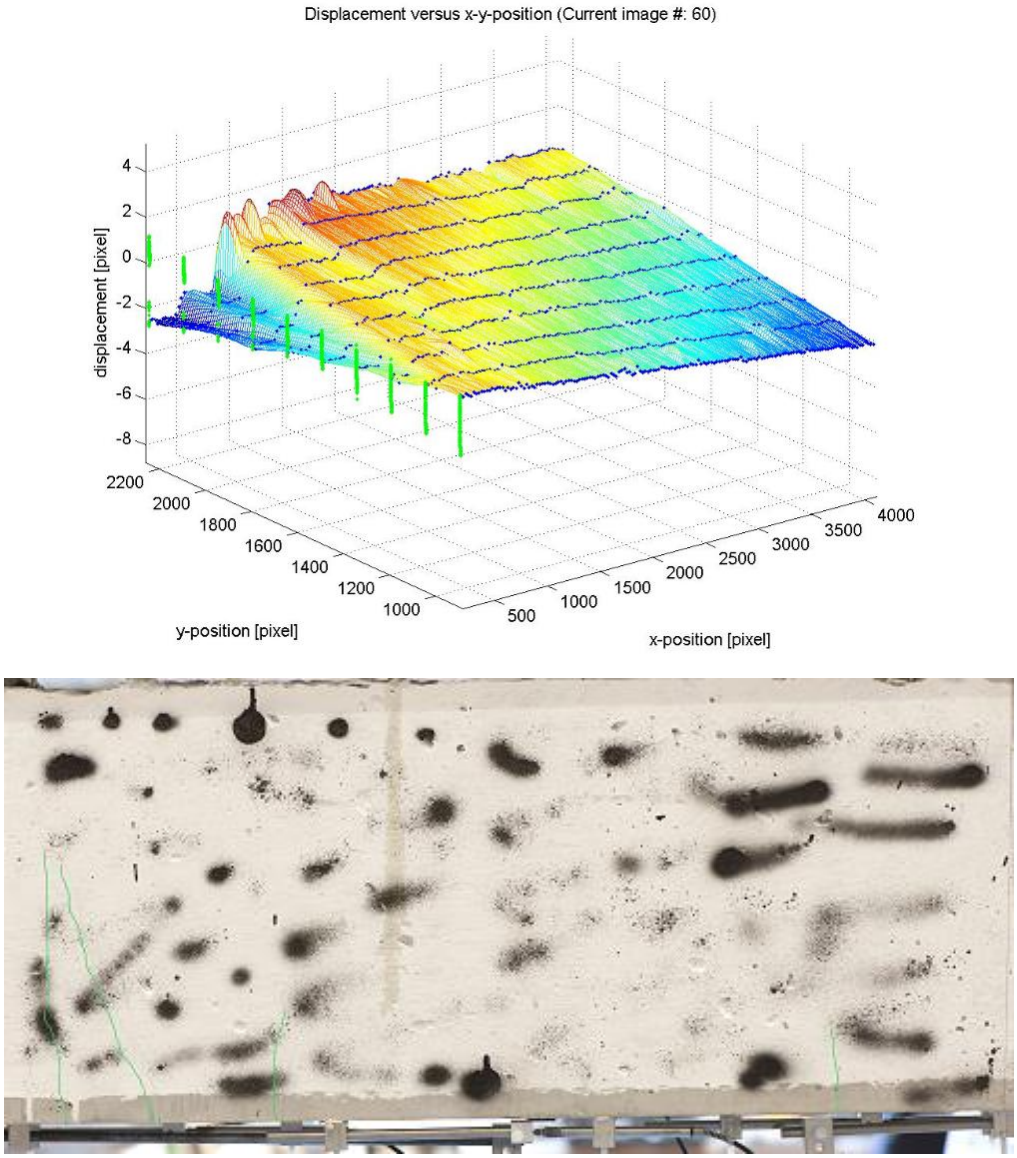

Figure 5.27 The displacement versus the pixel location (upper) for specimen FM2100-001, and corresponding picture of analyzed area with cracks highlighted with green lines (lower).

Table 5.9 compares the strain at MOR measured with the LVDT, defined engineering strain, and measured with the DIC, defined DIC strain. Specimen FM2100-001 is excluded in this table since the start of loading and pictures are on different times making it impossible to track the correct image number for the strain capacity. An review of the engineering strain from the LVDT vs the DIC strain is given in chapter 5.5.4.

Table 5.9 Strain capacity by engineering strain vs DIC strain.

Specimen	Engineering strain capacity [‰]	DIC strain capacity [‰]
FM175-001	18,3	11,7
FM350-003	13,4	14,1
FM700-002	7,4	13,6

5.5.3.2 CROSS SECTION STRAIN PROFILE

In Figure 5.28 and Figure 5.29 the strain profiles along the height of respectively the specimen FM175-001 and FM2100-003 are depicted. One can see the development of the strain during loading. For the FM175-001 specimen the MOR occurred around picture 32 and for FM2100-001 around picture 121. The DIC technique is not perfect since a full the strain profile in Figure 5.29 is shown to be fully compressed in picture 15.

However one can see the trend of a gradual upward shift of the neutral axis during loading. This shift is relatively bigger for FM175-001 compared with FM2100-001 and can be coupled to stronger plastic behavior of FM175-001. This is in accordance with the findings in the stress-strain diagrams in chapter 5.5.2.

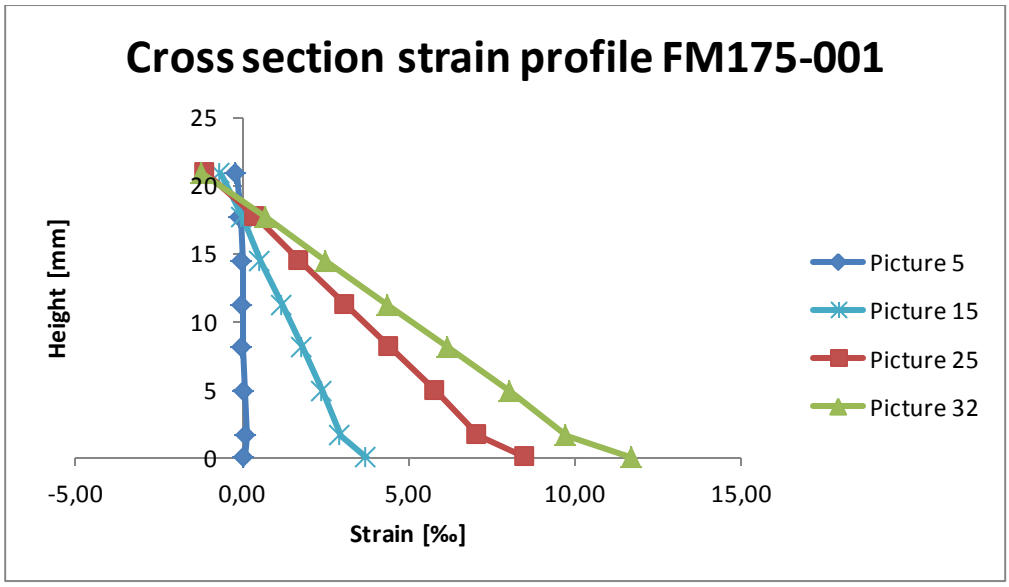

Figure 5.28 Strain profile of FM175-001 along the height of the specimen.

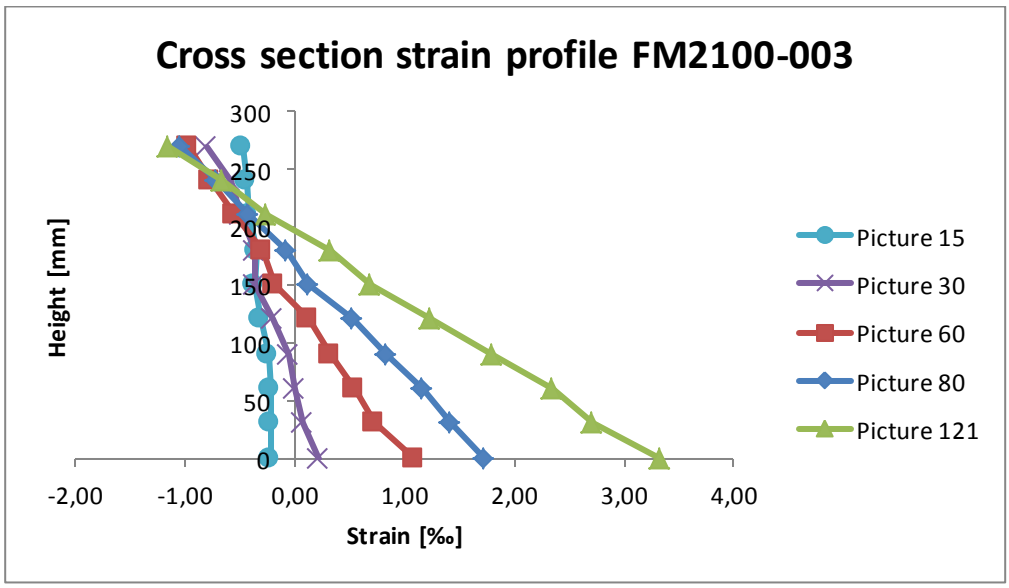

Figure 5.29 Strain profile of FM2100-002 along the height of the specimen.

5.5.3.3 CRACK WIDTH PROFILE

For the analysis of the crack width a measuring length of 15 mm was used for the FM175-001, FM350-003, and FM700-002, while for the FM2100-001 a length of 50 mm was used. This was due to the lower resolution of the images in the latter. In Figure 5.30 the specimen height is plotted against the crack width. The crack profile that is chosen to be analyzed is the localized macro crack at the moment of MOR. Figure 5.30 gives an indication on how deep the crack is. However the area close to the crack tip revealed such small strains that it was not possible to accurately follow the crack path and retrieve information over the full crack. It is recommended to improve the visualization of the strain gradient plot and the guide to selection of the pixel in the plot of the software.

From the stress-strain diagrams in chapter 5.5.2 it was seen that the nominal strength only dropped with the FM2100 specimens, while the strain capacity dropped gradually with the strain capacity. From Figure 5.30 one can see that these trends can be coupled with the crack width measured with the DIC for the specimens FM175-001, FM350-003, and FM2100-001. Specimen FM700-002 does not follow the expected trend and has the biggest crack width since the crack width at opening is not between that of FM350-003 and FM2100-01. An explanation is that the measured crack width is on one side-surface of the specimen, while the distribution of the crack width of one crack over the bottom of the specimen may vary. It may be possible that the crack width for the FM700-002 specimen is coincidentally relatively bigger at the surface where photos were taken of. This can be improved by taking making photos of the bottom of the specimen during loading. Figure 5.31 gives the crack profile of the localized macro crack for each specimen viewed from the bottom of the specimen. These photos were taken after the 4-PBT. The side where the camera made photos for the DIC analysis is indicated with the arrow. It can be speculated that the crack width distribution of the FM700-002 specimen over the beam thickness was different with relatively wider crack width at the side where the camera made photos. Which could explain the results in Figure 5.30. However Figure 5.31 shows the state of the crack after the 4-PBT while the state at MOR should be compared. For the crack width profile of specimens FM175 and FM350 see Appendix F.

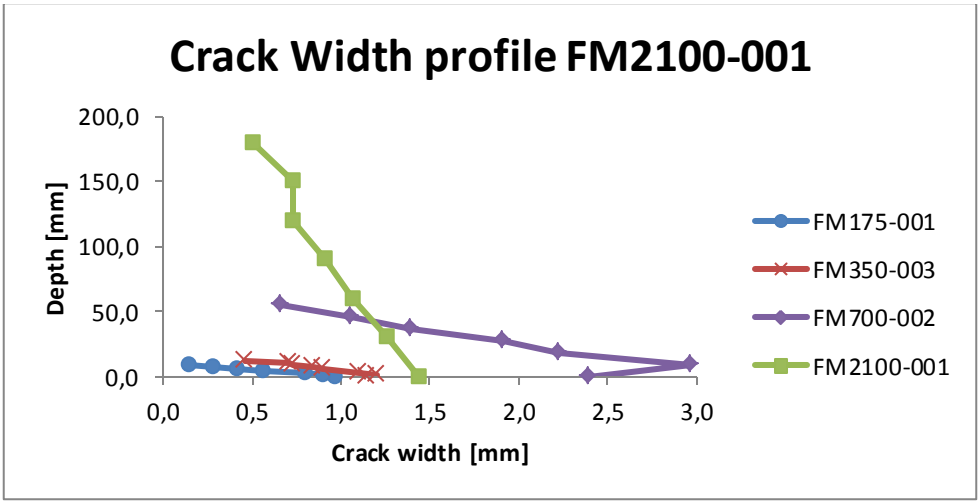

Figure 5.30 Crack width profile of localized macro crack at nominal strength.

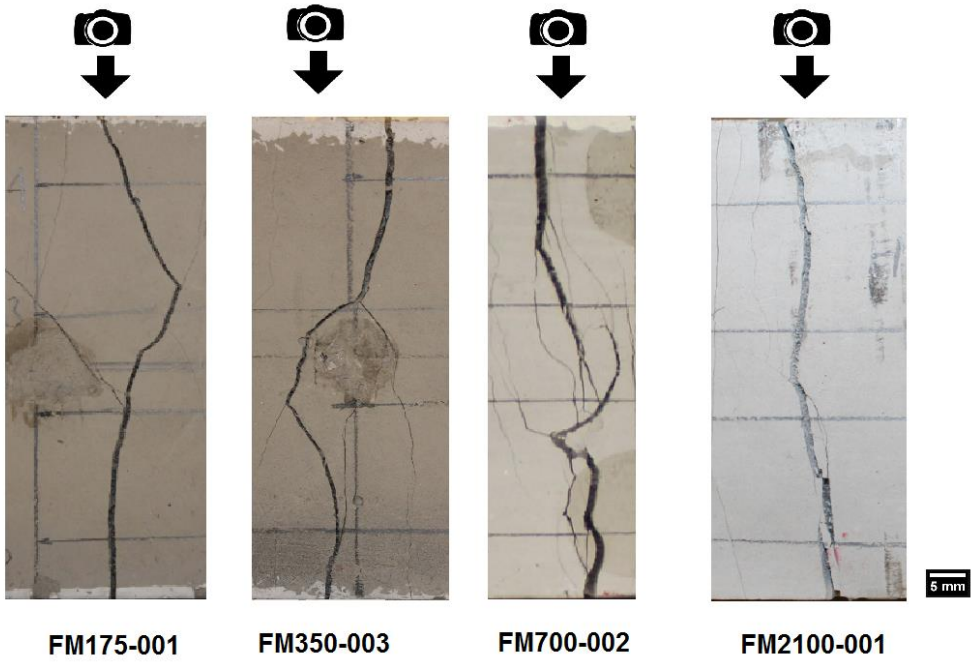

Figure 5.31 Crack pattern viewed from bottom of the specimens. Arrow gives side of camera surface in DIC.

5.5.4 FICTITIOUS STRAIN, ENGINEERING STRAIN, AND DIC STRAIN

5.5.4.1 FICTITIOUS STRAIN VS ENGINEERING STRAIN

In chapter 3 and 4 the fictitious strain which is based on linear elasticity and the beam deflection was used to analyze the strain of the specimens. However in literature study often the engineering strain is used to describe the strain capacity. It is expected that the fictitious strain resulted into much lower values compared to the engineering strain. As can be seen in Figure 5.32 the engineering strain is of a different order than the fictitious strain. The explanation for this observation was already given in chapter 3.5.3.2.

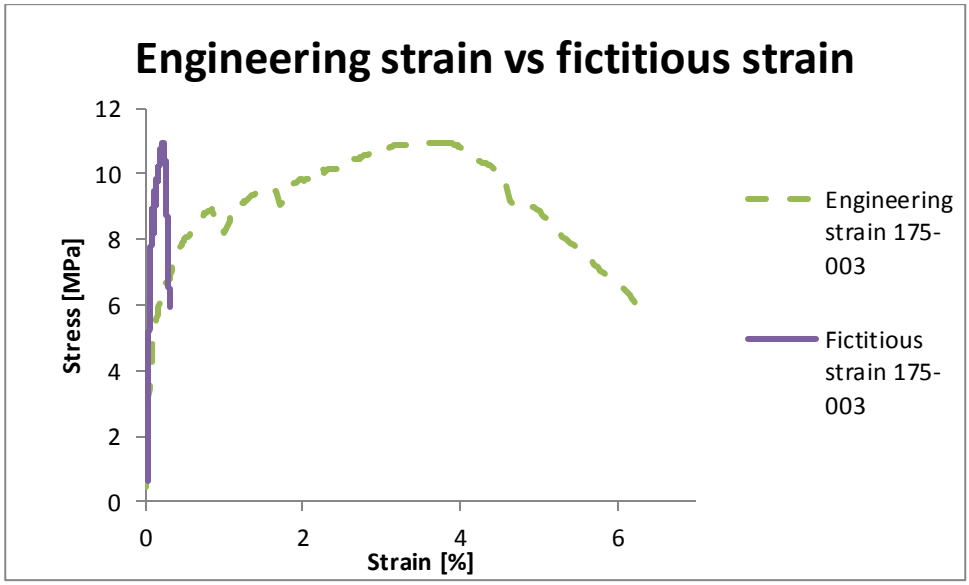

Figure 5.32 Measured engineering strain versus the calculated fictitious strain of specimen 175-003.

5.5.4.2 ENGINEERING STRAIN VS DIC STRAIN

The engineering strain was measured with a LVDT, while the DIC strain with the DIC technique. One would expect a larger strain when measuring with a LVDT. In Figure 5.33 the position of a LVDT after significant deformation from the 4-PBT is shown. The LVDT measures the deformation along the red line, while the horizontal elongation shown as the blue line is smaller. Furthermore the LVDT measures at a distance beneath the bottom of the specimen which introduces an eccentricity. This is depicted as the green arrow in Figure 5.33. While with the DIC technique one can measure directly at the bottom of the specimen without eccentricity.

The distortion in the DIC technique can be introduced by badly tracked markers. Also a time interval of pictures is chosen to be 5 seconds. It is impossible to precisely match the photographs with the data from the data from the INSTRON.

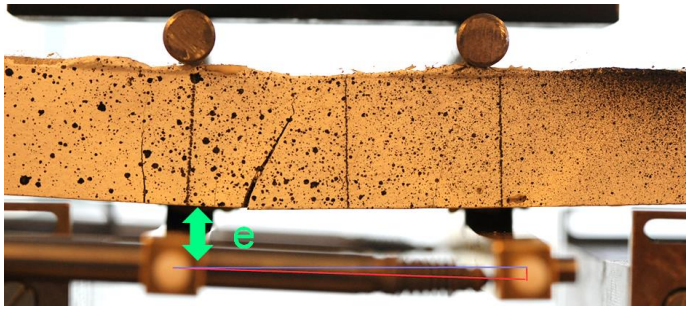

Figure 5.33 Position of LVDT during loading. Eccentricity by green arrow. Horizontal displacement blue line, but due to deformation LVDT measures red line.

5.5.4.3 STRAIN MEASUREMENT REVIEW

The fictitious strain calculated in chapter 3 and 4 were based on the displacement in the piston and linear elasticity. In reality the deflection of the beam is not equal to the displacement of the piston due

to deforming of the test setup. Furthermore it should be clear that the SHCC specimens does not behave linear elastic during testing.
The DIC strain can identify separate cracks in an efficient way and measures without eccentricity (Figure 5.33). However the accuracy depends on the time interval at which photos are taken and on the accuracy of the selection of the points where strain is measured. Both accuracies are not on the desired level yet. However it can easily measure the strain over an area compared to the method with LVDTs. Strain levels close to zero are not to be trusted, for example picture 15 in Figure 5.29. However this might be improved with calibration of the technique.
The engineering strain is the common method used in experiments. Compared to the DIC it has some disadvantages as described above. Furthermore it can only measure the elongation in the direction of its major axis (Figure 5.33). Another problem is the selection of the measuring length of the LVDT, which can influence the results significantly.
To conclude, the engineering strain measured with the LVDT is currently the most dependable. However the DIC strain is promising since it has multiple advantages over the engineering strain, but is currently not dependent due to the results which are illogical . This might be solved by calibration of the method.

5.6 CONCLUSIONS

5.6.1 CONCLUSIONS

- The fracture mechanics based size-effect was investigated by comparing the nominal strength and strain capacity of specimens with a fixed thickness of 0.075 m, fixed span-height ratio of 7, and span lengths of 0.175, 0.350, 0.700, and 2.100 m. This minimizes sources of size-effect introduced by the Wall-effect, diffusion phenomena, hydration heat, and statistical inhomogeneity of the material.

- It was observed that the nominal strength remains fairly constant for the smallest three specimen sizes, but drops with the biggest specimen size. A theoretical model has been developed which could explain the observations. This model is based on the length of the strain-hardening branch in the stress-strain diagram and describes how the strength along the height of the beam is related to this diagram. In the model it is suspected that size-effect exists due to a bigger crack width for the bigger specimens. An attempt was made to verify this with the DIC technique. However not a convincing result has been found. This might be due to the crack width profile which is differently distributed along the specimen thickness.

- A gradual drop in the strain capacity is seen in all specimen sizes. There is reason for concern, since not the nominal strength, but the strain capacity is the main reason for application of SHCC. A possible explanation for this drop is that the crack widths increases with increasing element size and which leads to the development of Griffith types of cracks instead of the steady state flat crack needed for the development of multiple fine cracks.

- Different measuring length of LVDTs may lead to a different magnitude of elastically loading and unloading of the specimen which occurs at the initiation of a crack. In theory this effect is eliminated when the measuring length is equal to the crack band width. With the DIC technique one can measure the strain at two desired points. However with current the current software it is not possible to accurately distinguish the crack band and to accurately select the desired pixel.

- The presumption concerning the fictitious strain based on linear elasticity and deflection of the specimen, and the engineering strain calculated from LVDT in chapter 3 and 4 have been verified. It has been shown that in the same specimen different strain values are found, where the fictitious strain is an underestimation of the strain due to its assumption of linear elasticity. The values of the engineering strain are in the same order of the SHCC in other literature.

- A comparison between the fictitious strain, engineering strain measured with LVDT, and DIC strain has been made. The engineering strain measured with the LVDT is currently the most dependable and common method. On the contrary the DIC strain is promising since it has multiple advantages over the engineering strain: no eccentricity, easier to cover whole area, and less influence by selection measuring length. However the results from the DIC strain at low strain levels are illogical. This might be solved by calibration of the method. Furthermore accuracy can be increased with improvement of the camera and software.

5.6.2 RECOMMENDATIONS

- It is recommended to improve the quality of the results by improving the mix design, specimen preparation, and calibration of the test setup.
  It was found that the flow time of the fresh mixture was not effectively altered by varying the w/p. It is advised to use a VMA.
  In order to minimize the badly tracked markers in the DIC software one should make an irregular pattern. In this research this has been achieved with a black painting spray. It should be noted that the composite is porous and an evenly painted surface will be painted. In order to avoid the button of the spray has been pushed halfway. This has produced satisfying results at times. An improvement would be different painting techniques which produce irregular dots.
  During the 4-PBT the localization of the macro crack occurred consistently at the same location for all FM700 and FM2100 specimens. This hints to a uneven loading by the piston. It is recommended to repeat the experiments after calibration of the testing apparatus.

- It is recommended that several assumptions and hypotheses have to be investigated for the proposed theoretical model.
  The proposed model that explains the size-effect depends on the bigger crack width with increasing specimen size. The results seem to be influenced by the distribution of the crack width over the thickness of the specimens. In this research photos were taken from the side of the specimens. The test setup for the DIC technique can be improved by photographs taken from the bottom of the specimens. Furthermore, if true then an explanation for this observation should be developed.
  The explanation of size-effect of the literature study and the model proposed in this thesis can both explain the decrease in the nominal strength for the FM2100 specimens if a shorter strain-hardening branch can be found by a UTT with the mix design used in chapter 5 compared to in the literature study.

- As concluded the strain measurement with the DIC technique shows many advantages to a method based on LVDTs. It is recommended to continue develop this method of strain measurement. Furthermore calibration of this measuring technique may improve the results.
  The software used for the DIC technique to measure strain between two points can improve its accuracy by including the pixel position of the selection tool in the gradient plot. Furthermore

the visualization by a contour plot instead of a gradient plot would increase the accuracy of selecting the measuring points even more.

- The time of LOP is now influenced by a couple of factors. The deflection of the FM175 and FM350 specimens were not directly measured from the beam, but the displacement of the piston. Differences can be introduced by the deformation of the test setup during testing and by the elastic deformation of objects put between the piston and specimen. Furthermore to spread the load of the piston in the FM700 and FM2100 specimens into two loads steel beams with significant weight was used. These were loaded on the specimens as instantaneous loads.
  It is recommended to develop a method to minimize these effects of energy introduction in the specimens introduced due to the loading rate and its influence on the results.

REFERENCE LIST PART III

[1] Zhou, Jian, et al. "Development of engineered cementitious composites with limestone powder and blast furnace slag." Materials and Structures 43.6 (2010): 803-814.
[2] Ostergaard, L., Walter, R., & Olesen, J. F. (2005). Method for determination of tensile properties of engineered cementitious composites (ECC). Proceedings of ConMat'05.
[3] Qian, S., & Li, V. C. (2007). Simplified inverse method for determining the tensile strain capacity of strain hardening cementitious composites. Journal of Advanced Concrete Technology, 5(2), 235-246.
[4] Li, M., & Li, V. C. (2013). Rheology, fiber dispersion, and robust properties of Engineered Cementitious Composites. Materials and structures, 46(3), 405-420.
[5] Şahmaran, M., Bilici, Z., Ozbay, E., Erdem, T. K., Yucel, H. E., & Lachemi, M. (2013). Improving the workability and rheological properties of Engineered Cementitious Composites using factorial experimental design. Composites Part B: Engineering, 45(1), 356-368.
[6] Li, V. C. (1998). Engineered Cementitious Composites-Tailored Composites Through Micromechanical Modeling.
[7] Concrete, S. C. (2005). The European Guidelines for Self-Compacting Concrete
[8] Tosun-Felekoğlu, K., Felekoğlu, B., Ranade, R., Lee, B. Y., & Li, V. C. (2014). The role of flaw size and fiber distribution on tensile ductility of PVA-ECC. Composites Part B: Engineering, 56, 536-545.
[9] Lee, B. Y., Kim, J. K., Kim, J. S., & Kim, Y. Y. (2009). Quantitative evaluation technique of Polyvinyl Alcohol (PVA) fiber dispersion in engineered cementitious composites. Cement and Concrete Composites, 31(6), 408-417.
[10] Baddeley, A., & Jensen, E. B. V. (2004). Stereology for statisticians. CRC Press.
[11] Schindelin, J., Arganda-Carreras, I., Frise, E., Kaynig, V., Longair, M., Pietzsch, T., ... & Cardona, A. (2012). Fiji: an open-source platform for biological-image analysis. Nature methods, 9(7), 676-682.
[12]Preibisch, S., Saalfeld, S., & Tomancak, P. (2009). Globally optimal stitching of tiled 3D microscopic image acquisitions. Bioinformatics, 25(11), 1463-1465.
[13] Mark Hall, Eibe Frank, Geoffrey Holmes, Bernhard Pfahringer, Peter Reutemann, Ian H. Witten (2009); The WEKA Data Mining Software: An Update; SIGKDD Explorations, Volume 11, Issue 1.
[14] Lepech, M., & Li, V. C. (2004). Size-effect in ECC structural members in flexure. Proc., FRAMCOS-5, Colorado, Eds. VC Li et al, 1059-1066.
[15] http://www.abmbv.nl/en/catalog/articlegroup/529623/vfunnel-apparatus, access date 12-05-2015
[16] Lepech, M. D., & Li, V. C. (2008). Large-scale processing of engineered cementitious composites. ACI Materials Journal, 105(4).
[17] Erbhl, C., http://www.mathworks.com/matlabcentral/fileexchange/12413-digital-image-correlation-and-tracking, access date 15-05-2015.

PART IV: CONCLUSIONS

6 CONCLUSIONS AND RECOMMENDATIONS

6.1 INTRODUCTION

At the end of chapters 0, 4, and 5 an extended version of the conclusions and recommendations are given per sub-question. This chapter is a summary of those conclusions and recommendation containing minor additions in order to connect the previous conclusions and recommendations with the aim of this thesis.

6.2 CONCLUSIONS

Literature study showed limited research on size-effect in SHCC. One research mentioned that there was no fracture mechanics based size-effect. Therefor first an experimental series was set up to prove whether there is size-effect to be found in SHCC. The purpose of this experimental series was not to investigate any of these sources separately and therefor called the 'general' size-effect.

- **3 GENERAL SIZE EFFECT:** When specimens of 120*30*10 mm^3 was upscaled to 360*90*30 mm^3 specimens, the nominal strength and fictitious strain capacity decreased from respectively 13.3±1.5 MPa to 8.4±0.4 MPa and 8.9±1.6 ‰, to 4.9±2.1 ‰. These drops in nominal strength and fictitious strain capacity are both significant and raises concerns since the magnification factor is 3.

- **3 GENERAL SIZE EFFECT:** It is strongly suspected that the displacement rate has a significant influence on the material behavior. When three specimens of 360*90*30 mm^3 within the same batch were loaded with 0.003mm/s, 0.025 mm/s, and 0.04 mm/s the nominal strength found in 0.003 mm/s dropped from 22 percent when the displacement rate was increased to 0.025 mm/s, while the fictitious strain capacity dropped 67 percent when the displacement rate was increased to 0.04 mm/s. This can be explained by the introduction of the energy into the specimens, where factors such as creep, relaxation, and redistribution of the stresses play a role.

After general size-effect was found it was decided to investigate two possible sources of size-effect: the fiber-effectivity size-effect and fracture mechanics based size-effect. Since fibers play a pivotal role in the mechanism developing the multiple fine cracks and fracture mechanics based is a main contributor for size-effect in ordinary concrete.

- **4 FIBER EFFECTIVITY SIZE-EFFECT:** By casting SHCC in a cube of 150*150*150 mm^3 and then sawing out specimens of 120*30*10 mm^3 at different orientations, the effect of fiber effectivity on the nominal strength and strain capacity of thin casted specimen and a thick element (SHCC cube) will be compared in a 4-PBT. With analysis of sections with a thickness of 40 microns it has been verified that 3D fiber orientation and dispersion has been achieved for the specimen sawn out of the SHCC cube.

- **4 FIBER EFFECTIVITY SIZE-EFFECT:** The nominal strength and strain capacity decreased in the order of the ML-, C-, A-, and B-specimens. Coincidentally this exact order was also found for the

minimum of the fiber effectivity parameters. It seems that the average amount is less important, as for the B-specimens all higher numbers of fibers per cm^2 was found than in the A-specimens, but worse mechanical properties were calculated.
It is speculated that the more weaker cross sections there are, the higher the chance there is for crack initiation at a weak cross section. Which will terminate the development of multiple fine cracks at an early stage. This seems to explain the differences between the ML-, A-, and C-specimens.

- **4 FIBER EFFECTIVITY SIZE-EFFECT:** In specimens B quasi-brittle failure is most probably caused by the placement procedure. The SHCC cube was filled by hand with scoop. Due to the small volume of SHCC added per scoop and the self-compacting ability of the fresh mixture, horizontal layers exist in the plane with weaker interfaces for the matrix properties and perhaps little to no fibers crossing the interface plane. This combination leads to crack initiation at a plane where fiber effectivity is simultaneously low. Additionally for specimens B it is expected that each single plane covers the whole cross section if plotted over the cross section. This might explain the quasi-brittle failure found consistently in the B-specimens and specimen C002.

- **5 FRACTURE MECHANCS BASED SIZE-EFFECT:** The fracture mechanics based size-effect was investigated by comparing the nominal strength and strain capacity of specimens with a fixed thickness of 0.075 m, fixed span-height ratio of 7, and span lengths of 0.175, 0.350, 0.700, and 2.100 m. This minimizes sources of size-effect introduced by the Wall-effect, diffusion phenomena, hydration heat, and statistical inhomogeneity of the material.
It was observed that the nominal strength remains fairly constant for the smallest three specimen sizes, but drops with the biggest specimen size. A theoretical model has been developed which could explain the observations. This model is based on the length of the strain-hardening branch in the stress-strain diagram and describes how the strength along the height of the beam is related to this diagram. In the model it is suspected that size-effect exists because of a bigger crack width for the bigger specimens. An attempt was made to verify this with the DIC technique. However not a convincing result has been found. This might be due to the crack width which is differently distributed along the specimen thickness.
A gradual drop in the strain capacity is seen in all specimen sizes. There is reason for concern since not the nominal strength, but the strain capacity is the main reason for application of SHCC. A possible explanation for this drop is that the crack widths increases with increasing element size and reduced steady state flat cracks type cracks will develop.

- **5 FRACTURE MECHANCS BASED SIZE-EFFECT:** A comparison between the fictitious strain, engineering strain measured with LVDT, and DIC strain has been made. The engineering strain measured with the LVDT is currently the most dependable and common method. On the contrary the DIC strain is promising since it has multiple advantages over the engineering strain: no eccentricity, easier to cover whole area, and less influence by selection measuring length. However the results from the DIC strain at low strain levels are illogical. This might be solved by calibration of the method. Furthermore accuracy can be increased with improvement of the camera and software.

6.3 RECOMMENDATIONS

- It has been proved that there is a general size-effect between specimens of 120*30*10 mm^3 and 360*90*30 mm^3. The next step is to identify possible sources of size-effect, and quantify and qualify the size-effect per source. In this thesis the fiber-effectivity size-effect and fracture mechanics based size-effect will be investigated. Since fibers play a pivotal role in the mechanism developing the multiple fine cracks and fracture mechanics based is a main contributor for size-effect in ordinary concrete. It is recommended that remaining sources will also be investigated since SHCC might behave differently than ordinary concrete.

- The effect of loading (displacement) rate seems to be significant for the nominal strength and strain capacity. More samples have to be tested in order to draw statistical based conclusions.

- A crack pattern characterization for differently sized specimens should be performed to investigate whether upscaling element size has influence on the crack pattern. The crack width distribution is an important diagram and can be analyzed with the protocol given in chapter 3.5.4. Differently sized specimens should be loaded until a fixed strain and compared with each other.

- When designing with SHCC one should acquire relevant parameters in experiments with specimens that have comparable specimen height as the design of the structure. For thicker SHCC elements this lead to a different arrangement of fiber orientation than in common specimen dimensions in literature study. Common specimen dimensions in the lab will lead to an unsafe overestimation of the nominal strength and strain capacity.

- A placing method to eliminate the weak interfaces which are responsible for the brittle failure in specimens with orientation B should be developed. It is expected that a continuous placing of the composite, in combination with a mixture with low yield stress and high viscosity may lead to elimination of these weak interfaces and prevent brittle failures.
  The effect of including primary steel bar reinforcement in specimens B should be investigated. It might be that the steel bar reinforcement avoids the brittle failure, while the fibers are primarily responsible for to the development of multiple fine cracks.

- It is recommended to improve the quality of the results by improving the mix design, specimen preparation, and calibration of the test setup.
  It was found that the flow time of the fresh mixture was not effectively altered by varying the w/p. It is advised to use a VMA.
  In order to minimize the badly tracked markers in the DIC software one should make an irregular pattern. In this research this has been achieved with a black painting spray. It should be noted that the composite is porous and an evenly painted surface will be painted. In order to avoid the button of the spray has been pushed halfway. This has produced satisfying results at times. An improvement would be different painting techniques which produce irregular dots.
  During the 4-PBT the localization of the macro crack occurred consistently at the same location for all FM700 and FM2100 specimens. This hints to a uneven loading by the piston. It is recommended to repeat the experiments after calibration of the testing apparatus.

- It is recommended that several assumptions and hypotheses have to be verified to increase the validation of the proposed theoretical model.

The proposed model that explains the size-effect depends on the bigger crack width with increasing specimen size. The results seem to be influenced by the distribution of the crack width over the thickness of the specimens. In this research photos were taken from the side of the specimens. The test setup for the DIC technique can be improved by photographs taken from the bottom of the specimens. Furthermore, if true then an explanation for this observation should be developed.
The explanation of size-effect of the literature study and the model proposed in this thesis can both explain the decrease in the nominal strength for the FM2100 specimens if a shorter strain-hardening branch can be found by a UTT with the mix design used in chapter 5 compared to in the literature study.

- As concluded the strain measurement with the DIC technique shows many advantages to a method based on LVDTs. It is recommended to continue develop this method of strain measurement. Furthermore calibration of this measuring technique may improve the results. The software used for the DIC technique to measure strain between two points can improve its accuracy by including the pixel position of the selection tool in the gradient plot. Furthermore the visualization by a contour plot instead of a gradient plot would increase the accuracy of selecting the measuring points even more.

- The time of LOP is now influenced by a couple of factors. The deflection of the FM175 and FM350 specimens were not directly measured from the beam, but the displacement of the piston. Differences can be introduced by the deformation of the test setup during testing and by the elastic deformation of objects put between the piston and specimen. Furthermore to spread the load of the piston in the FM700 and FM2100 specimens into two loads steel beams with significant weight was used. This were loaded on the specimen as instantaneous loads.
It is recommended to develop a method to minimize these effects of energy introduction in the specimen introduced by the loading rate and hence its influence on the results.

APPENDICES

APPENDIX-A: SINGLE FIBER PULLOUT TEST

Three important physically meaningful parameters in the fiber-matrix interface are:

- Chemical bond strength (G_d), quantified by interfacial fracture toughness
- Initial frictional bond strength (τ_0) for small sliding movements of the fibers
- Slip-hardening coefficient (β), that characterizes the increasing effective frictional bond during large sliding (pullout).

These parameters can be found via the single fiber pullout test. In SHCC most often fibers with high aspect ratio are used, for example PVA-fibers. These are extremely brittle of nature.. Therefor accurate alignment of the fiber is important. Furthermore the fiber should not bend while testing. In [1] a method for producing single fiber pullout specimen is described (App. A - figure 1).

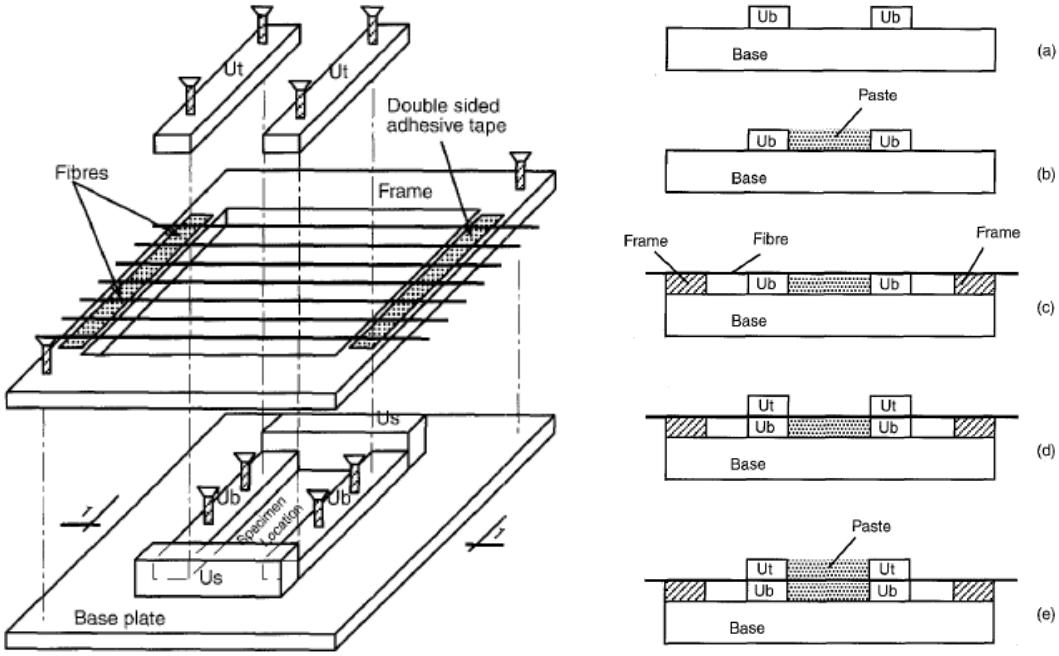

App. A - figure 1 Setup of the mold and the fibers (left), and cross section 1-1 through the mold and working order [1].

The casting setup consists of a base plate with components *Us* and *Ub*. First this part of the mold is filled with SHCC to the level of *Ub*. Then a frame with accurately aligned fibers attached by tape is placed upon the base plate. The final parts of the mold *Ut* are mounted on *Ub* and the mold will be completely filled with SHCC. A needle is used to stir the concrete between the two layers. After hardening the specimen can be taken out by demounting *Ub* and *Ut*, cut, and installed in the loading cell stage as in App. A - figure 2.

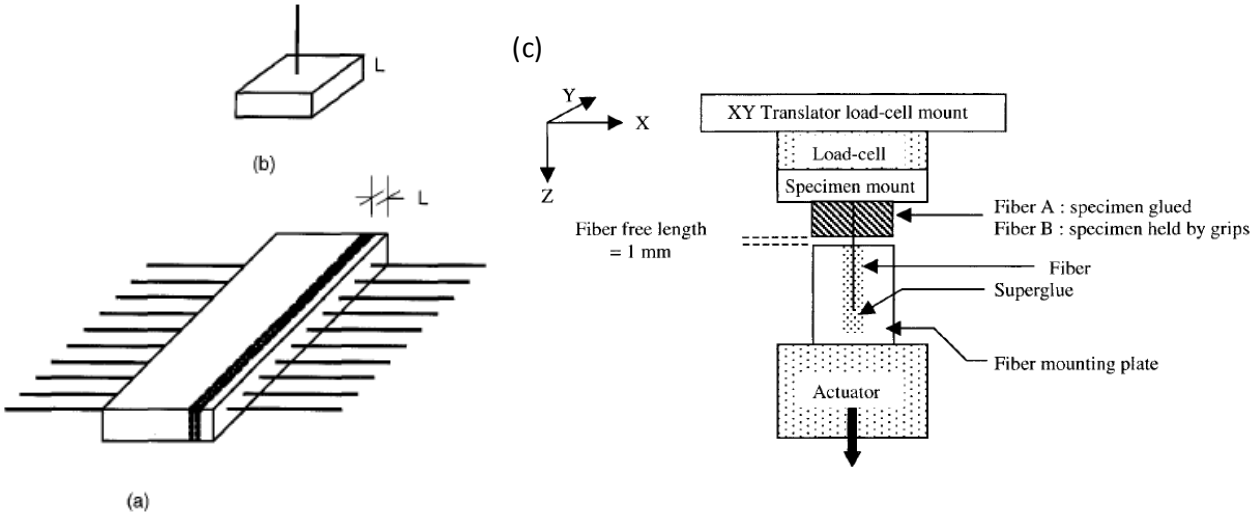

App. A - figure 2 Specimen after demolding (a) and cutting (b) [1], and installed in experimental set-up (c) [2].

App. A - figure 3 shows a general profile of a single fiber pullout curve. Where l_d is the debonded length and l_e the embedded length of the fiber. The curve starts with an elastic part, this is the elastic stretching of the free fiber length. Then debonding of the fiber takes place: at load P_a there is a sudden load drop to P_b. If the load drop is big it is due to the presence of a chemical bond between the fiber and matrix. In case of little to no drop the fibers are non-chemically bonded with the matrix. The following part of the curve is due to frictional bond. Three cases with different slip hardening coefficient are presented: $\beta<0$, $\beta=0$, and $\beta>0$ for respectively slip softening, constant friction, and slip hardening. The cases are likely depending on the fiber hardness. Soft fibers tend to show slip-hardening. Conversely constant friction or slip-softening is often observed with fibers with fiber hardness higher than that of the surrounding matrix [2].

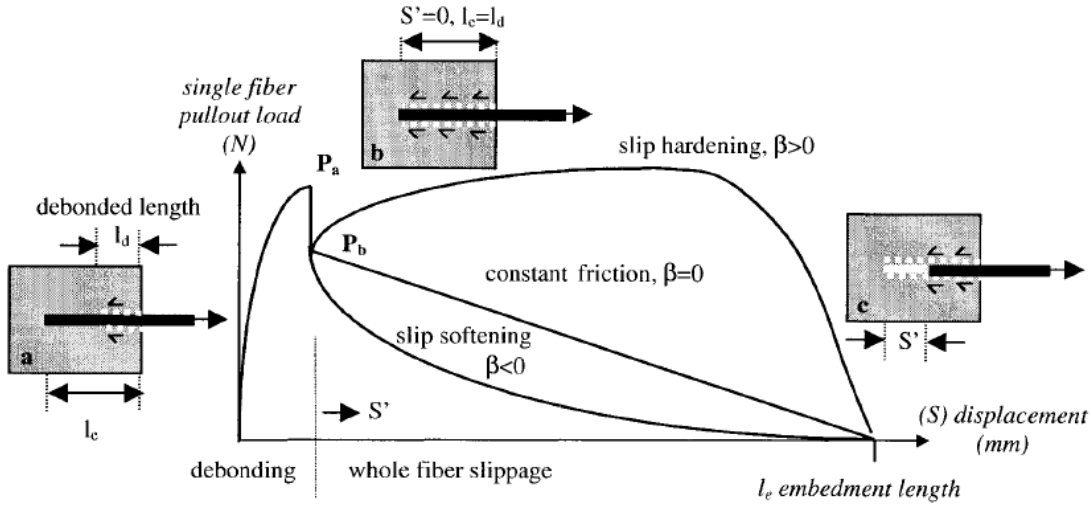

App. A - figure 3 General profile of a single fiber pullout curve [2].

With (eq. 6.1), (eq. 6.2), and (eq. 6.3) one can respectively calculate the chemical bond, frictional bond and friction coefficient. Where E_f, l_f, and d_f are respectively the fiber's Young's modulus, length, and diameter and S is the displacement of the fiber.

$$G_d = \frac{2(P_a - P_b)^2}{\pi^2 E_f {d_f}^2} \qquad \textit{(eq. 6.1)}$$

$$\tau_0 = \frac{P_b}{\pi d_f l_e} \qquad \textit{(eq. 6.2)}$$

$$\beta = \left(\frac{d_f}{l_f}\right)\left[\left(\frac{1}{\tau_0 \pi d_f}\right)\left(\frac{\Delta P}{\Delta S'}\right)\Big|_{S'\to 0} + 1\right] \qquad \textit{(eq. 6.3)}$$

[1] Katz, A., & Li, V. C. (1996). A special technique for determining the bond strength of micro-fibres in cement matrix by pullout test. Journal of materials science letters, 15(20), 1821-1823.
[2] Redon, C., Li, V. C., Wu, C., Hoshiro, H., Saito, T., & Ogawa, A. (2001). Measuring and modifying interface properties of PVA fibers in ECC matrix. Journal of Materials in Civil Engineering, 13(6), 399-406.

APPENDIX B: FILLER MATERIALS AND PARTICLE SIZE-DISTRIBUTION

In recent years due to environmental and economic reasons, industrial by-products have been used as supplementary materials in concrete mixtures. Among them are blast furnace slag, fly ash, limestone powder, and silica fume. In some cases these are used as material enhancer.

BLAST FURNACE SLAG (BFS) [1]

BFS is a glassy material, which is sandy sized, sharp pointed, and irregularly shaped. It is the main cement replacement used in the Netherlands. BFS is produced as by-product of manufacturing the pig iron in blast furnaces.

Addition of BFS to the cement mixture improves the long term strength and lowers the heat of hydration. However the early strength (first 24 hours) will also be lowered. Use of slag in a cementitious materials increases the ratio of tensile to compressive strength. Furthermore addition of BFS leads to a finer pore system of the composite which is beneficial for the durability of a structure. Additionally BFS protects against swelling by alkali reaction and/or resistance to sulphates. However BFS reduces the resistance against carbonation.

FLY ASH (FA)

FA consists of a mixture of alumina-silicate glass and some crystalline constituents. It is mainly small and spherical shaped. There are two classes of FA, class F and C [ASTM C618 2008a]. Class F is the class that is mainly available in the Netherlands. It is produced by the burning of anthracite or bituminous coals. This FA has a low lime content and is pozzolanic. Class C is produced from lignitic coal and has a higher CaO content with some hydraulic properties.

The addition of FA lowers the hydration heat, suppresses the alkali-aggregate reaction, and increases the workability. The addition of FA may increase the sensitivity to carbonation of the concrete. However it should also be stated that concretes containing FA will have lower lime content than OPC. Thus the amount of material to be carbonated is lower. The long term compressive strength and durability of FA concrete will be higher than that of concrete with OPC [1].

Another research [2] states that addition of FA to SHCC lowers the interfacial chemical bond and the matrix toughness, while the interfacial frictional bond is enhanced. This all in favor of the tensile ductility of SHCC. Though in [3] it is noted that the increase of tensile ductility by increasing FA and slag conten, is accompanied by a reduction of fracture toughness of matrix, and the compressive and flexural strengths of SHCC. In this the effect of two amounts of FA-cement ratio have been investigated: 1.1 and 2.2.

Relevant conclusions of this research were:

- FA-SHCC compared to slag-SHCC measured more deflection capacity, which translates in tensile ductility. FA-SHCC also lead to tighter crack widths.
- Mixtures with higher aggregate content and grain sizes increase the matrix cracking toughness, thus decreasing the tensile ductility. This negative influence is almost negated by the addition of FA-cement ratio of 2.2 in the SHCC.

SILICA FUME (SF)

SF consists of very fine particles of almost exclusively amorphous SiO_2. The particles are 100 times finer than those of OPC. It is a by-product of the fabrication of silicon metal, ferrosilicon alloys, or zirconium. SF is a very reactive pozzolane. However it is more expensive than cement.

Addition of SF in concrete decreases the bleeding and creates a more compact zone around the aggregates. The reaction of SF is activated in alkaline environments. Thus an increased replacement of OPC with SF, which decreases the pH of the pore solution, will slow down the reaction of SF. Resulting into different findings of early strength due to SF replacement for cement [1].

LIMESTONE POWDER (LP)

Limestone powder consists of mainly calcium carbonate. For use in concrete the calcium carbonate should be at least of 75% by weight and the amount of magnesia content limited. This impurity may react with water and potentially cause expansion in the hardened cement paste. LP is produced by finely grinding limestone, which is used as aggregate and raw material for cement.

Addition of LP accelerates the early cement hydration and forms more CH, which can be later consumed by BFS if added. Early strength will be higher, while compressive strength at 28 days lower through the addition of LP. In general concretes with LP have lower porosity than pure OPC concrete[1].

PARTICLE SIZE DISTRIBUTION

A proper mix design should include careful particle size distribution of the cement, mineral admixtures and filler material. By designing a closely packed material matrix one could achieve enhance the flowability, workability, the fiber-matrix interface properties, and the stability of the mix. This can be achieved by the use of the Fuller curve. Funk and Dinge made an modification of this curve [1] given in (eq. 6.4). Where CPFT is the cumulative percent of particles finer than a particle with a diameter of D, D_l the largest grain size, D_s the smallest grain size, and q an adjustment factor depending on the particle size. Funk and Dinger proposed a value of 0.37 for the optimum.

$$CPFT = 100\left(\frac{D^q - {D_s}^q}{{D_L}^q - {D_s}^q}\right) \qquad \textit{(eq. 6.4)}$$

[1] Sierra-Beltran, M. G. (2011). Ductile Cement-Based Composites with Wood Fibres-material design and experimental approach. TU Delft, Delft University of Technology.

[2] Sahmaran, M., Lachemi, M., Hossain, K. M., Ranade, R., & Li, V. C. (2009). Influence of aggregate type and size on ductility and mechanical properties of engineered cementitious composites. ACI Materials Journal, 106(3).

[3] Şahmaran, M. S., Yücel, H. E., Demirhan, S., & C Li, V. (2012). Combined Effect of Aggregate and Mineral Admixtures on Tensile Ductility of Engineered Cementitious Composites. ACI Materials Journal, 109(6).

APPENDIX C: PRODUCT INFO LP AND CEMIII/B 42.5 N LH HSR

CARMEUSE
NATURAL SOLUTIONS

TECHNISCHE FICHE

CALCITEC 2001M

KALKSTEENMEEL – $CaCO_3$

CHEMISCHE ANALYSE (gemiddelde waarden)

	Absolute Eis BRL 1804	Eis BRL 1804	90% gebied	Gemiddelde
Carbonaten	≥ 87	≥ 90	94-100	99,4 %
$CaCO_3$	≥ 72	≥ 75	94-100	98,9 %
MgO				0,26 %
SiO_2				0,17 %
Al_2O_3				0,03 %
Fe_2O_3				0,04 %

Reactiviteit tov alkaliën	niet reactief
$Na_2O_{eq} = Na_2O + 0,658 \times K_2O$	0,01 %
Vochtgehalte	0,08 %
Totaal zwavelgehalte (S)	0,02 %
In zuur oplosbare sulfaten (SO_3)	Cat. AS0.2 0,04 %
In water oplosbare chloorionen (Cl^-)	< 0,008 %
Organische stoffen	geen O.S.
pH	9,4

FYSISCHE PARAMETERS & KORRELVERDELING (gemiddelde waarden)

VISEAANSE KALKSTEEN	
Reële volumieke massa	2.690 kg/m³
Los stortgewicht	900 kg/m³
Aangestampt stortgewicht	1.350 kg/m³
Specifieke oppervlakte Blaine	470 m²/kg
Specifieke oppervlakte BET	1,14 m²/kg
Methyleen blauw waarde MB	0.66 %
Witheid FY	57
Hardheid (Mohs)	3

KORRELVERDELING
Laser SYMPATEC

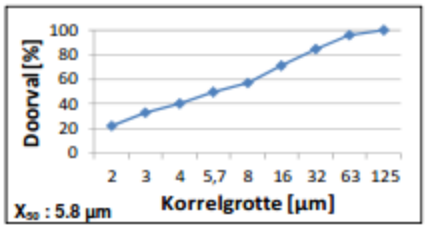

Luchtstraalzeven	Eis BRL 1804 % m/m	90% gebied % m/m	Gemiddelde % m/m
2 mm	100	100	100
500 µm	-	99 - 100	100
125 µm	85 - 100	90 - 100	99
63 µm	70 - 100	90 - 100	94

PRODUCTIELOCATIE
B - 4520 MOHA

VEILIGHEID
Veiligheidsfiche verkrijgbaar op aanvraag

BEHANDELING & OPSLAG
Droog opslaan. Het product is inert en niet gevaarlijk

REF/NORMEN
EINECS 215-279-6
CAS 471-34-1
Vrij van REACH
0785-CPR-31-217-13
EN 12620
EN 13139

CE 0785

DoP: 0785-CPR-31217-13-Mo-1502-1306

Daar het product van natuurlijk oorsprong is, zijn de vermelde waarden gemiddeldes die enigzins kunnen variëren en die niet bindend zijn voor het bedrijf.

UPDATE 18/04/2014 **EDITIE** 20.55.230 **CARMEUSE SA** **www.carmeuse.be** **info@carmeuse.be**

CEM III/B

april 2014

Hoogovencement

CEM III/B 42,5 N-LH/SR

CEM III/B 42,5 N-LH/SR

ENCI
Technische Voorlichting
Postbus 3233
5203 DE 's-Hertogenbosch
Tel: 073 640 12 20
Fax: 073 640 12 18
tv@enci.nl
www.enci.nl

CBR Cementbedrijven
Afdeling Technische Voorlichting
Terhulpsesteenweg 185
1170 Brussel
Tel: 02 678 35 10
Fax: 02 675 23 91
communication@cbr.be
www.cbr.be

1. Normen en certificaten

Type cement	Certificaat	Norm	
CEM III/B 42,5 N-LH/SR	CE	EN 197-1	0956-CPR-1103.1067
CEM III/B 42,5 N-LH/SR	KOMO	BRL 2601	1103-14-1067
CEM III/B 42,5 N-LH/SR	BENOR	NBN B12	14-11-171-1

2. Opgegeven samenstelling

	Eenheden	Gemiddelde waarden	Normeisen	
			min.	max.
Bestanddelen in % van de som van de hoofd- en nevenbestanddelen				
Klinker (K)	%	29	20	34
Hoogovenslak (S)	%	68	66	80
Filler	%	3	–	5
Toevoegingen in % van het cement				
Bindtijdregelaar	%	5,3	–	–
Maalhulpstof	%	0,035	–	–
Reductiemiddel*	%	0	–	–

* Overeenkomstig de Europese richtlijn 2003/53/CE en KB 2861/2004 wordt aan sommige cementen een reductiemiddel toegevoegd om het gehalte aan oplosbaar chroom (VI) te beperken tot maximaal 0,0002%.

3. Chemische kenmerken

De chemische kenmerken van het cement worden bepaald volgens EN 196-2.

	Eenheden	Gemiddelde waarden	Normeisen	
			min.	max.
CaO	%	45	–	–
SiO_2	%	28	–	–
Al_2O_3	%	10	–	–
Fe_2O_3	%	1	–	–
C_3A	%	–	–	–
Sulfaat SO_3	%	2,8	–	4,0
Onoplosbare rest	%	2,5	–	5,0
Gloeiverlies	%	0,7	–	5,0
Chloride	%	0,03	–	0,10
Chroom (VI)*	%	< 0,0002	–	0,0002
Na_2O equivalent	%	0,65	–	–

* Overeenkomstig de Europese Verordening (EG) nr. 1907/2006 (REACH) moet het gehalte aan oplosbaar chroom (VI) beperkt zijn tot maximaal 0,0002%. Dit gehalte wordt bepaald volgens EN 196-10.

Rotterdam

4. Fysische kenmerken

De fysische kenmerken worden bepaald volgens de genormaliseerde proefmethoden vermeld in de kolom.

	Proef-methode	Eenheden	Gemiddelde waarden	Normeisen	
				min.	max.
Waterbehoefte	EN 196-3	%	30,5	–	–
Begin van de binding	EN 196-3	minuten	230	60	–
Einde van de binding	EN 196-3	uren	04:30	–	–
Vormhoudendheid	EN 196-3	mm	0	–	10
Specifiek oppervlak (Blaine)	EN 196-6	cm²/g	4110	–	–
Zeefrest op 200 µm	EN 196-6	%	–	–	–
Hydratatiewarmte op 7 d	–	J/g	233	–	270
Volumieke massa					
Absoluut	–	kg/m³	2940	–	–
Stortgewicht	–	kg/m³	1100	–	–
Beta-p	–	–	–	–	–
C-Waarde	–	–	1,55	–	–

5. Mechanische kenmerken

De druksterkte van het cement, gemeten op proefstukken gemaakt van een genormaliseerde mortel, wordt bepaald volgens EN 196-1.

Druksterkte	Eenheden	Gemiddelde waarden	Normeisen	
			min.	max.
Na 1 dag	MPa	4	–	–
Na 2 dagen	MPa	11	10,0	–
Na 7 dagen	MPa	31	–	–
Na 28 dagen	MPa	55	42,5	62,5

6. Productie en levering

Dit cement wordt geproduceerd op de locatie van ENCI in Rotterdam en kan op de volgende wijze worden afgeleverd:

Scheepsbulk	Autobulk	Verpakt
x	x	–

7. Het managementsysteem van de fabriek is gecertificeerd

8. Prestatieverklaring conform CPR(EU) Nr.305/2011

Identificatie: 0956-CPR-1103.1067

Website: www.enci.nl

De resultaten weergegeven in de tabellen zijn gebaseerd op gemiddelde waarden en zijn louter indicatief. Enkel de normeisen worden gewaarborgd.

Rotterdam CEM III/B 42,5 N-LH - April 2014

APPENDIX D: DERIVATION OF DISPLACEMENT-STRAIN RELATION

Consider the beam with length *L* as depicted in App. D - Figure 1. Where *u* is defined as the elongation along the *x*-axis, and *w* as the deflection along the z-axis. The strain along *z,* the height of the beam, at a random cross section can be calculated as given in (eq. 6.5). Where ε is the first derivative of *u* as a function of *x*, and κ_z is equal to the negative second derivative of *w*.

$$\varepsilon(z) = \varepsilon + \kappa_z z \qquad \textit{(eq. 6.5)}$$

With the help of beam formulas one can express the maximum deflection δ of the beam in a 4PBT as (eq. 6.6). Where *P, a, and L* are respectively the total force applied by the inner supports, the distance between the outer and inner support, and *a*, the distance between the outer supports.

$$\delta = \frac{0.5Pa}{24EI_{zz}}(3L^2 - 4a^2) \qquad \textit{(eq. 6.6)}$$

By rearranging terms one can find (eq. 6.7) for *P*.

$$P = \frac{12EI_{zz}\delta}{(3aL^2 - 4a^3)} \qquad \textit{(eq. 6.7)}$$

*Mz, t*he maximum constant moment in the 4-PBT can be calculated by (eq. 6.8)(eq. 6.8).

$$M_z = \frac{1}{2}Pa \qquad \textit{(eq. 6.8)}$$

(eq. 6.9) shows the constitutive relation of the bending moment.

$$M_z = EI_{zz}\kappa_z \qquad \textit{(eq. 6.9)}$$

By substituting (eq. 6.7) into (eq. 6.8) and then solving κ_z with (eq. 6.9), κ_z can be calculated by (eq. 6.9).

$$\kappa_z = \frac{6\delta}{(3L^2 - 4a^2)} \qquad \textit{(eq. 6.10)}$$

Combining (eq. 6.10) with (eq. 6.5) gives to (eq. 6.11), which gives the strain of a beam section along the height of the beam. By choosing an appropriate *z* one can calculate the strain in the outer tensile fiber, since deflection has been measured and the dimensions *L* and *a* are known. Where the origin of *z* lies on the neutral axis of the beam.

$$\varepsilon(z) = \frac{6\delta z}{(3L^2 - 4a^2)} \qquad \textit{(eq. 6.11)}$$

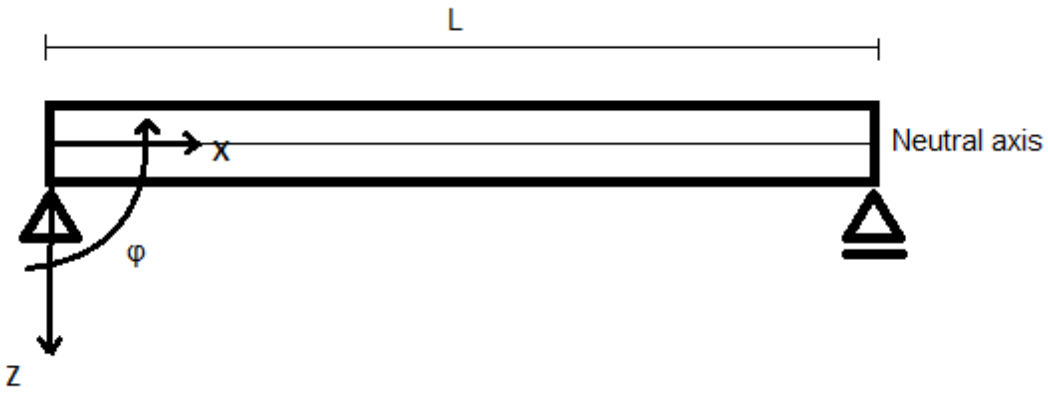

App. D - Figure 1Chosen coordinate axis for the calculation of the strain in beam with length l under bending.

APPENDIX E: CRACK PATTERN SPECIMENS CHAPTER 4

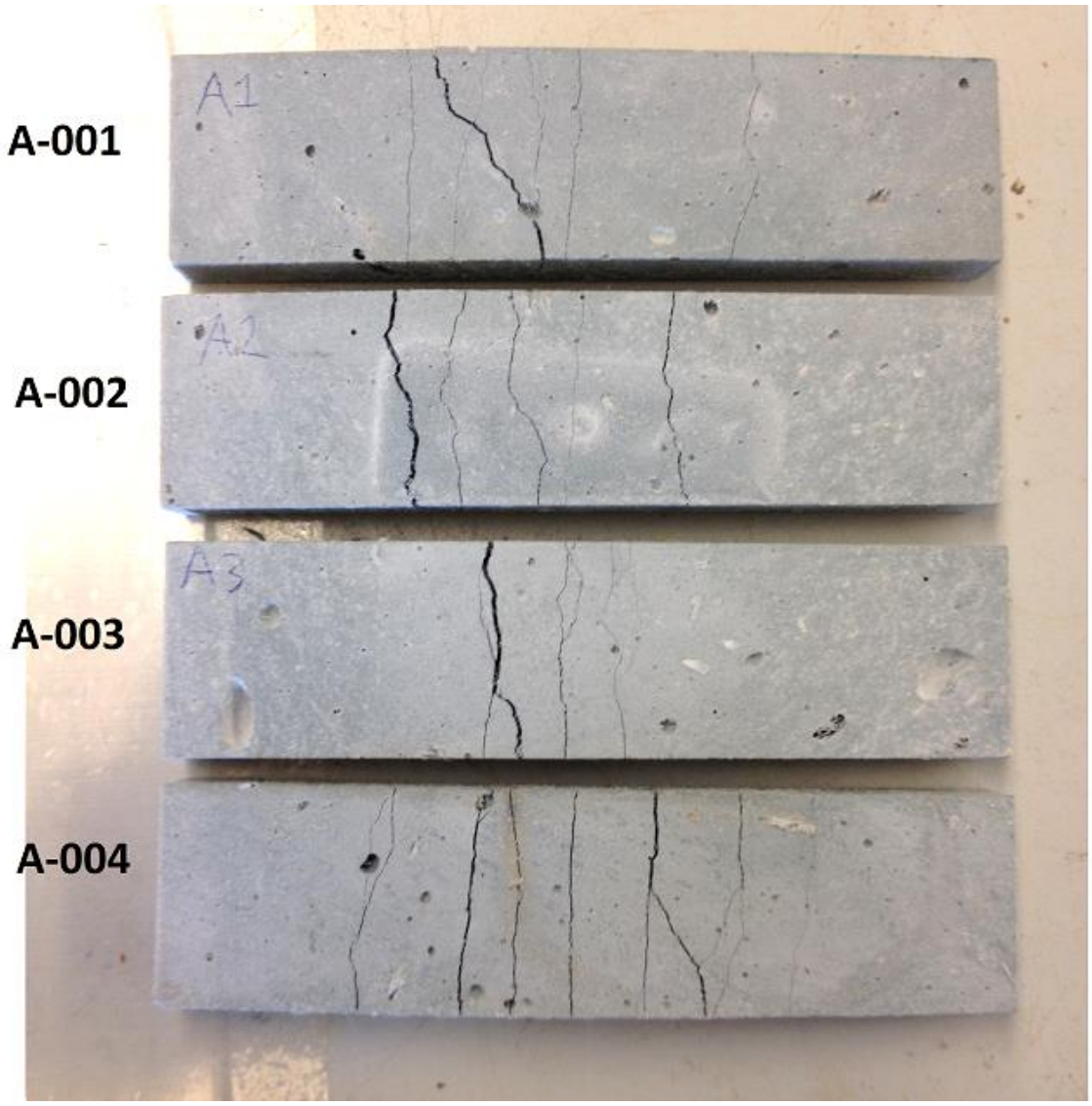

App. E - Figure 1 Crack Pattern of specimens A.

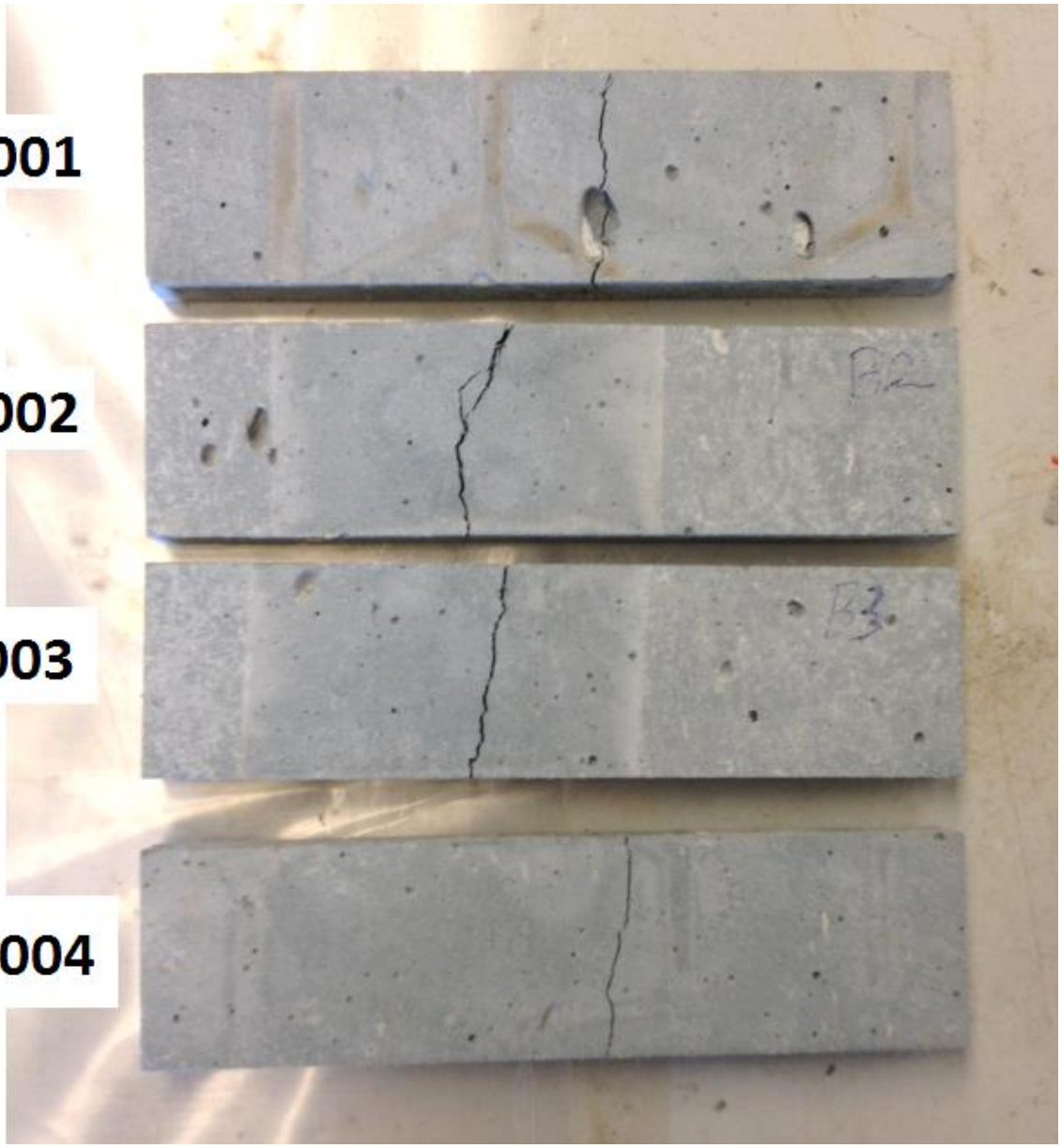

App. E - Figure 2 Crack Pattern of specimens B.

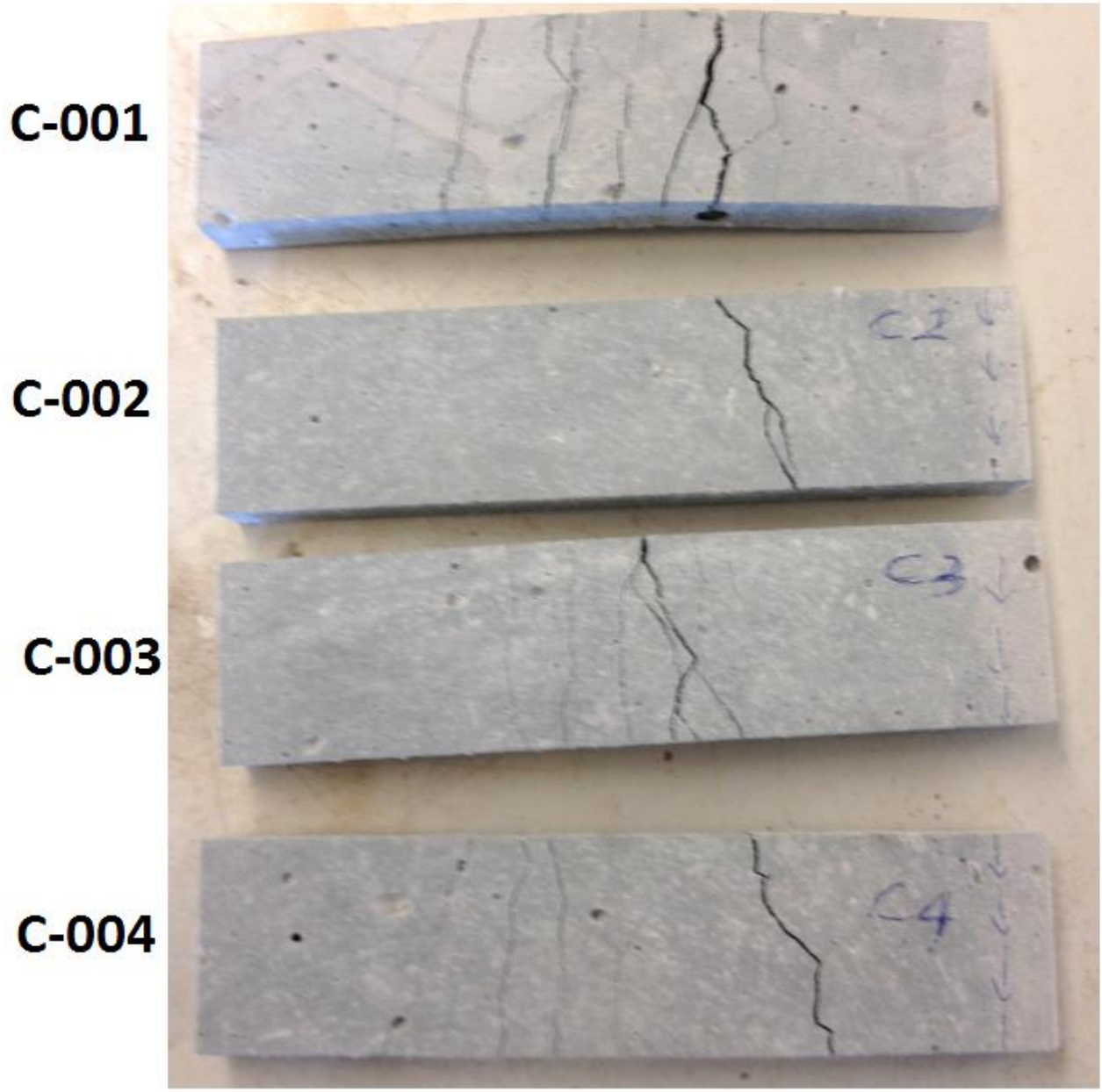

App. E - Figure 3 Crack Pattern of specimens C.

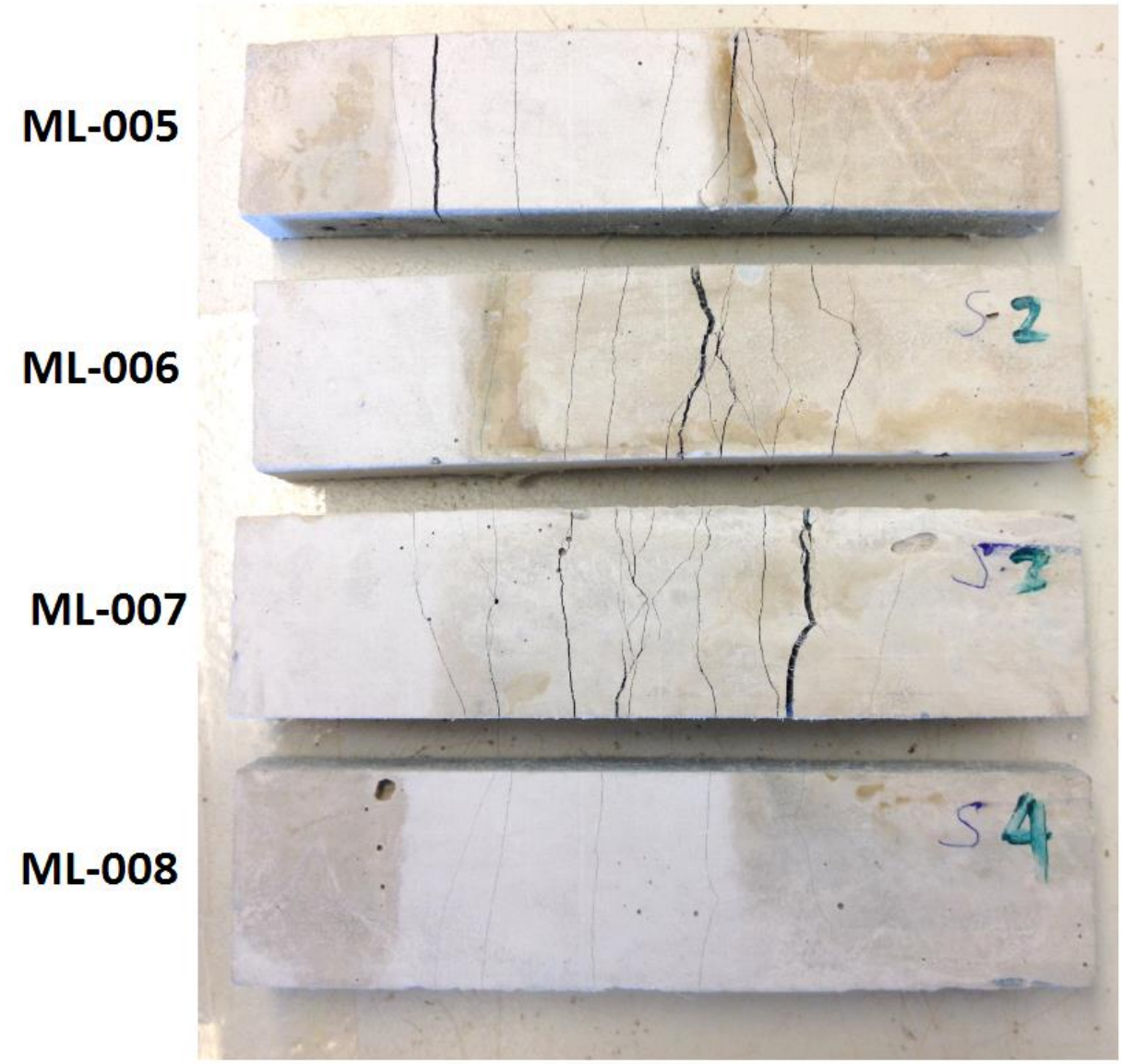

App. E - Figure 4 Crack Pattern of specimen ML specimens batch 2.

APPENDIX F: CRACK PATTERN OF FM175 AND FM350 SPECIMENs

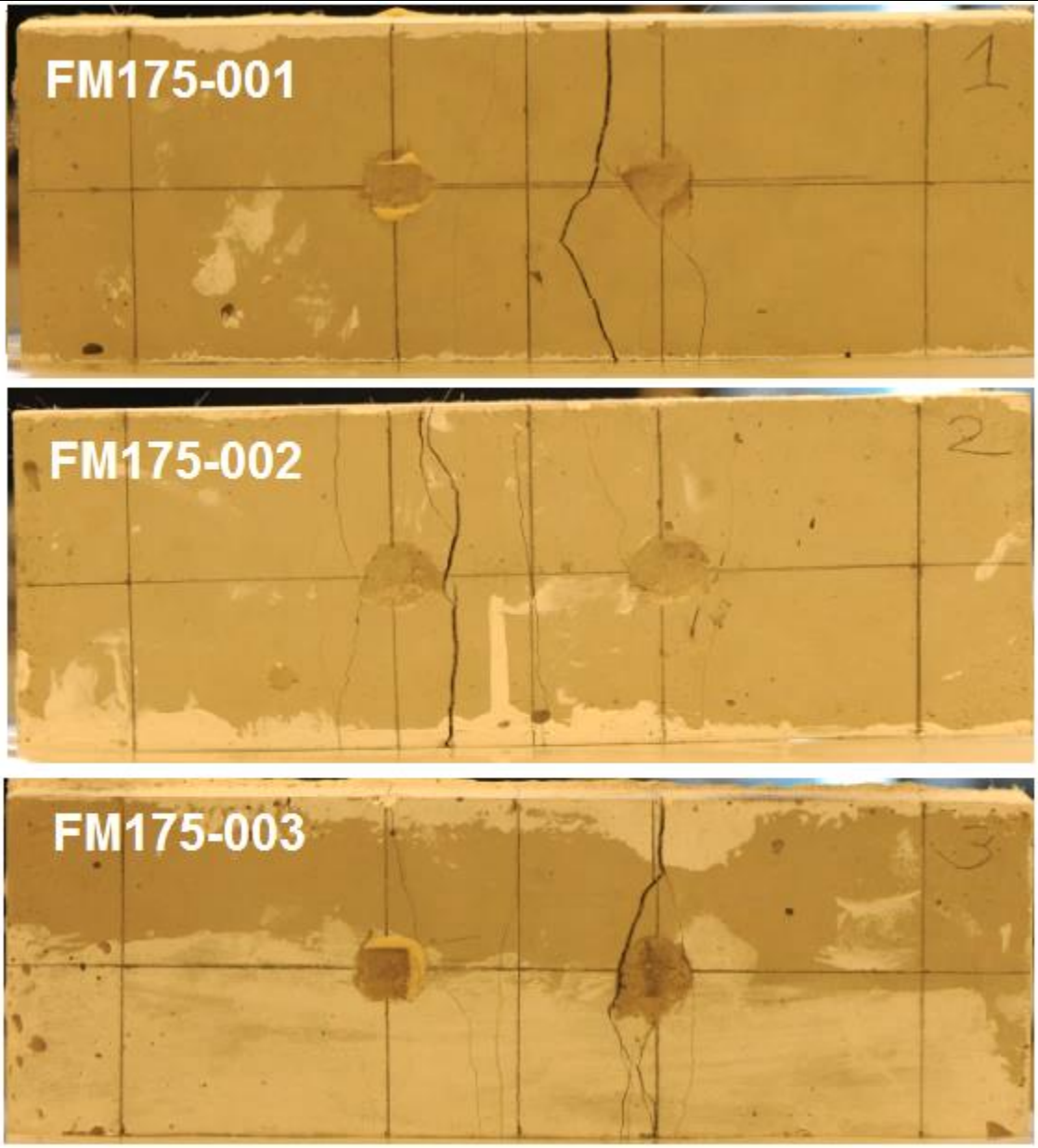

App. E - Figure 1 Crack Pattern of FM175 specimens.

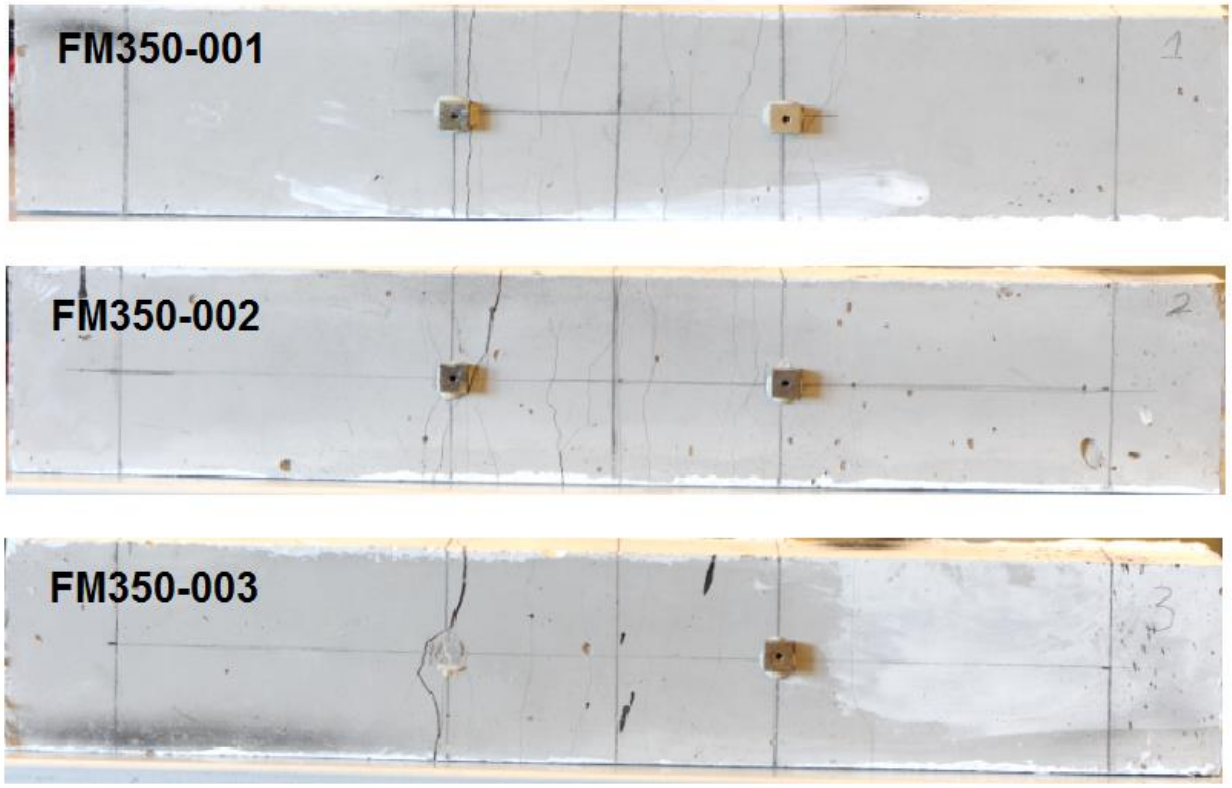

App. E - Figure 2 Crack Pattern of FM350 specimens.